DUDLEY KNOX LIBRARY
NAVAL POSTGRADUATE SCHOOL
MONTEREY CALIFORNIA 93943-5002

STUDY OF RESIDUAL STRESSES AND MICROCRACKS IN HIGH STRENGTH STEEL WELDMENTS

An Investigation of Microcrack Formation and Stressed Growth
Using Laser Microscopy

by

STEPHEN EDWARD IWANOWICZ

B.S. Chemical Engineering, 1983
University of Massachusetts, Amherst Massachusetts

B.S. Biochemistry, 1980
University of Massachusetts, Amherst Massachusetts

Submitted to the Department of OCEAN ENGINEERING in Partial Fulfillment of the Requrements for the Degrees of

NAVAL ENGINEER
and
MASTER OF SCIENCE IN MECHANICAL ENGINEERING
at the
MASSACHUSETTS INSTITUTE OF TECHNOLOGY
JUNE, 1992

© Stephen Edward Iwanowicz,1992

Thesis
T96
a1

DUDLEY KNOX LIBRARY
NAVAL POSTGRADUATE SCHOOL
MONTEREY, CALIFORNIA 93943-5002

STUDY OF RESIDUAL STRESSES AND MICROCRACKS IN HIGH STRENGTH STEEL WELDMENTS

An Investigation of Microcrack Formation and Stressed Growth
Using Laser Microscopy

by

STEPHEN EDWARD IWANOWICZ

Submitted to the Department of Ocean Engineering on 15 May 1992 in partial fulfillment of the requirement for the degree of Naval Engineer and Master of Science in Mechanical Engineering.

ABSTRACT

The confocal scanning laser microscope (CSLM) allows viewing welds with a resolution to 0.25 microns. The image processor of the CSLM provides effectively infinite depth of field by superposing the in-focus parts of images. Slopes of more than 30 degrees do degrade the image, however.

4-point bend tests of bead-on-plate welds on 11 mm thick mild steel, HY-100, HSLA-100, and HY-130 were performed to strains of 0 to 0.02 parallel to the weld bead. A longitudinal, single-pass weld bead of E7014 was manually applied to one specimen of each material with shielded metal arc welding.

Displacement-load and moment-curvature results were as expected.

Images from gold-shadowed replicas studied using the CSLM were recorded both on video tape and photographically. Initial microcracks 1 - 200 microns long were observed in the weld metal. No microcracks were observed in the HAZ of any material. Slag and oxide layers sometimes interfered with observing the weld metal and adjacent baseplate. Under monotonic loading, cracks widened with little growth and Widmanstatten structures appeared unchanged. Crack-like features, 1.5 microns long were present on the weld and on the HAZ. These features are probably oxide cracks and did not appear to grow when stressed.

A literature search gave important references regarding mechanisms for residual stress and microcrack formation, microcrack growth, and methods for their reduction.

Thesis Supervisor: Koichi Masubuchi, PhD,
Title: Kawasaki Professor of Engineering

Acknowledgements

I would like to give my heartfelt thanks to Professor Koichi Masubuchi for his support and guidance. The excitement he found in new ideas and innovations was contagious.

I wish to extend my sincere thanks to Professor Frank McClintock for offering his valuable insight and advice garnered by years of experience. His unbridled enthusiasm and his ability to approach technical subjects with a burning desire to understand them through a thorough and meticulous application of the scientific method was inspirational. I also thank him for showing me that learning doesn't stop with formal education.

I owe a great deal of gratitude to the United States Navy for their support. Without them, none of this would have been possible.

Partial support by the Office of Naval Research, Ref N00014-86-J-1218 for thesis advising is gratefully acknowledged.

Thanks also go to Xiaodong Wang for assistance in performing my experiments.

My deepest appreciation goes to my family. For my wife Lynne who was always there for me, showing love and strength and a lot of understanding and patience over these past three long years. For my little girls, Jennifer and Michelle, who continually amaze and delight me. Thank you for making us a family and making our lives bountiful and complete. To my Dad who taught me the meaning of craftsmanship and from whom I inherited an intense desire to find out how things tick. I wish you could have been here to see this. And to my Mom, who always knew how important family and education were. I wouldn't be here today if it were not for you.

Finally, I thank God for giving me the strength through faith to persevere through the difficult and trying times.

Table of Contents

Study of Residual Stresses and Microcracks in High Strength Steel Weldments

An Investigation of Microcrack Formation and Stressed Growth Using Laser Microscopy

TITLE PAGE 1
ABSTRACT 2
ACKNOWLEDGEMENTS 3
TABLE OF CONTENTS 4
LIST OF TABLES 7
LIST OF FIGURES 8
SYMBOLS AND DEFINITIONS 11

CHAPTER 1
1.0 Introduction 14
1.1 History of Welding 14
1.2 Modern Uses of Welding 15
1.3 Problems in Welded Structures 16

CHAPTER 2
2.0 Theory and Background 18
2.1 Overview 18
2.2 Non-Destructive Testing and the Laser Microscope 19
2.3 Anatomy of a Weld 24
2.4 Stress, Strain, and Related Topics 26
2.4.1 Stress and the Continuum 26
2.4.2 Strain 28
2.4.3 Ut Tensio Sic Vis 30
2.4.4 Stress-Strain Curves 31
2.5 Residual Stresses 33
2.6 Prediction of Residual Stresses 45
2.7 Measurement of Residual Stresses 48
2.8 Cracking in Weldments 50
2.8.1 Residual Stresses and Cracking of Weldments 50
2.8.2 Hot Cracking 50
2.8.3 Cold Cracking 70
2.9 Crack Propagation Under Static Loading 81
2.9.1 Elastic Deformation and Yielding 81
2.9.2 Fracture Mechanics and Crack Propagation 81

2.9.3 Stress Fields and Microcracks 82
2.9.4 Cracking Modes 82
2.9.5 Stress Intensity Factor 84

CHAPTER 3
3.0 Experimental 90
3.1 Overview 90
3.2 Materials 91
3.2.1 Mild Steel 91
3.2.2 Q&T Steels 92
3.2.3 HSLA Steels 93
3.2.4 Origin 95
3.2.5 Specimen Design 95
3.2.6 Specimen Fabrication and Welding 98
3.3 Equipment 99
3.4 Experimental Procedure 101

CHAPTER 4
4.0 Results and Discussion 104
4.1 Initial Conditions 104
4.2 Displacement-Load Curves 105
4.2.1 Mild Steel 106
4.2.2 HY-100 107
4.2.3 HSLA-100 and HY-100 108
4.3 Moment-Curvature Diagrams 109
4.4 Replicas and Laser Microscopy 114
4.4.1 General Baseplate Appearance 116
4.4.2 Mild Steel 116
4.4.3 HY-100 118
4.4.4 HSLA-100 123
4.4.5 HY-130 124
4.5 Discussion of Technique 130

CHAPTER 5
5.0 Conclusions 134

CHAPTER 6
6.0 Future Work 137

TABLES 139

FIGURES 151

REFERENCES 221

APPENDICES

A. Non-Destructive Testing Techniques, An Overview 227
B. The Confocal He-Ne Laser Microscope 237
C. Replication Technique 249
D. Literature Review 251
E. Experimental Results 283
F. Video Tape Map 289

List of Tables

No.	Title	Page
1	Crack Characteristics	139
2	Hot Crack Classification	140
3	An Alternative Hot Crack Classification Scheme	141
4	Relative Hot Cracking Potency Factors of Elements in Iron Binary Systems	142
5	Inagaki Limits on Steel Constituents for Hot Cracking	144
6	Material Composition and Properties	145
7	Estimated Specimen Yield Loads	147
8	Specimen Distortion from Welding	148
9	Specimen Characteristics	149
10	Summary of Displacement-Load Curves	150

List of Figures

No.	Title	Page
1	Thermal Cycle of a Weld	151
2	Anatomy of a Weld	152
3	State of Stress	153
4	Stress-Strain Curve	154
5	Arc Efficiency Values for Various Welding Processes and Materials	155
6	Temperature and Residual Stress Variation Along a Weld	156
7	Residual Stresses in a Butt Weld	157
8	Major Tensile Stresses and Distortions in a Butt Weld	158
9	Major Tensile Stresses and Distortions in a T Joint	159
10	Discretized Model Illustrating Residual Stresses	160
11	Temperature Variation of Yield Strength	161
12	Charpy V-Notch Specimen Orientation in Plate	162
13	Grinding Induced Residual Stresses	163
14	Effect of Tension on Residual Stresses	164
15	Fe-C Phase Diagram	165
16	Quasi-Equilibrium Solidifying Weld Pool	166
17	Fillet Weld Cross Section	167
18	The Effects of Constitutional Features on Cracking Susceptibility in Binary Systems	168
19	Liquid Phase Distributions	169
20	Cracking Modes	170
21	Surface Crack in Plate	171
22	4-Point Bend Test to Determine K_{Ic}	172
23	4-Point Bend Test Apparatus Setup	173
24	4-Point Bend Test Specimen	174
25	Bead-on-Plate Specimen	175
26	Initial Distortion from Welding with E7014	176

List of Figures

No.	Title	Page
27	Mild Steel Displacement-Load Curve	177
28	HY-100 Displacement-Load Curve	178
29	HSLA-100 Displacement-Load Curve	179
30	HY-130 Displacement-Load Curve	180
31	Combined Displacement-Load Curve	181
32	Similar Triangles	182
33	First Approximation of Curvature	183
34	Mild Steel Moment-Curvature Diagram	184
35	HY-100 Moment-Curvature Diagram	185
36	HSLA-100 Moment-Curvature Diagram	186
37	HY-130 Moment-Curvature Diagram	187
38	Combined Moment-Curvature Diagram	188
39	HY-130 Baseplate, No Load, 40x Objective Lens	189
40	Mild Steel, 40x Objective Lens	190
41	Mild Steel, 14 kN Load, 40x Objective Lens	191
42	Mild Steel, 14 kN Load, 100x Objective Lens	192
43	HY-100, No Load, 40x Objective Lens	193
44	HY-100, No Load, 40x Objective Lens	194
45	HY-100, 20 kN Load, 40x Objective Lens	195
46	HY-100, 20 kN Load, 40x Objective Lens	196
47	HY-100, 33 kN Load, 40x Objective Lens	197
48	HY-100, 33 kN Load, 40x Objective Lens	198
49	HY-100 Weld Metal, No Load, 40x Objective Lens	199
50	HY-100 Weld Metal, 33 kN Load, 40x Objective Lens	200
51	HSLA-100, No Load, 40x Objective Lens	201
52	HSLA-100, 30 kN Load, 40x Objective Lens	202
53	HSLA-100 Weld Metal, 30 kN Load, 40x Objective Lens	203

List of Figures

No.	Title	Page
54	HY-130, No Load, 40x Objective Lens	204
55	HY-130, No Load, 40x Objective Lens	205
56	HY-130, No Load, 40x Objective Lens	206
57	HY-130, 5 kN Load, 40x Objective Lens	207
58	HY-130, 5 kN Load, 40x Objective Lens	208
59	HY-130, 5 kN Load, 40x Objective Lens	209
60	HY-130, 40 kN Load, 40x Objective Lens	210
61	HY-130, 40 kN Load, 40x Objective Lens	211
62	HY-130, 50 kN Load, 40x Objective Lens	212
63	HY-130, 50 kN Load, 40x Objective Lens	213
64	HY-130, 50 kN Load, 40x Objective Lens	214
65	HY-130 Weld Metal, No Load, 40x Objective Lens	215
66	HY-130 Weld Metal, 5 kN Load, 40x Objective Lens	216
67	HY-130 Weld Metal, 40 kN Load	217
68	HY-130 Weld Metal, 40 kN Load	218
69	HY-130 Weld Metal, 40 kN Load, 100x Objective Lens	219
70	HY-130 Weld Metal, 50 kN Load	220

Symbols and Definitions

Symbol	Definition	Units
α	Linear Coefficient of Thermal Expansion	
γ	Gamma Function	none
γ_{SFE}	Surface Free Energy	
δ_{ij}	Dirak Delta	none
ε_{ij}	Strain	none
ε_{ij}^{e}	Elastic Strain Tensor	none
ε_{ij}^{p}	Plastic Strain Tensor	none
κ	Coefficient for HAZ Hot Cracking	
λ	Lamé Constant	
μ	Lamé Constant	
ν	Poisson Ratio	none
ρ	Density	kg m^{-3}
σ_{ij}	Stress	N m^{-2}
A	Area	m^2
b_i	Body Forces	N kg^{-1} m^3
CE	Carbon Equivalent	percent
C_l	Composition of Liquid Equilibrium	percent
C_o	Initial Alloy Composition	percent
C_s	Interface Composition When f_s is Solid	percent
d	Grain Diameter	mm
E	Young's Modulus	N m^{-2}
E_T	Young's Modulus, a Function of Temperature	N m^{-2}
F	Force	N
F(x,y)	Airy's Stress Function	none
f_s	Weight Fraction of Solid	none
h	Arc Intensity	joules $inch^{-1}$

Symbols and Definitions

Symbol	Definition	Units
H	Electrical Energy	cal sec^{-1}
I	Current	amperes
k	Equilibrium Partition Ratio	none
l	Length	m
l_0	Initial Length	m
M	Moment	N m
n_j	Normal Vector	none
P	Load or Force	N
Q	Effective Thermal Power	joules sec^{-1}
S_{HC}	Sensitivity to Hot Cracking	none
T	Temperature	°C or °K
T_0	Initial Temperature	°C or °K
T_{BS}	Bulk Solidus Temperature	°C or °K
T_m	Melting Temperature	°C or °K
t_p	Plate Thickness	m or inches
u_i	Displacement	m
v	Welding Travel Speed	m sec^{-1}
V	Volume	m^3
V	Voltage	volts

(this page intentionally left blank)

CHAPTER 1

Introduction

1.1 History of Welding

Welding is defined as the joining of similar materials through fusion. For metals, the welding process forms a localized coalescence of materials produced by heating the metals to the welding temperature. Welding may occur with or without use of either a filler material or the application of pressure. Welding may also be accomplished by the application of pressure alone. It is distinguished from brazing and soldering where an intermediate metal of a lower melting point than the base metal is used to bond two materials. The method of brazing uses filler metals having a liquidus above 450°C; soldering uses filler metals melting below this temperature. (Connor, 1987) The origin of welding has been lost in the mists of time, but archaeologists can trace welding techniques to prehistoric times. A modern day example of an ancient welding technique is the fusing of layers of steel in the forging of samurai swords.

To make welding a productive technique for joining significantly large pieces of metal, a large supply of heat must be available. Prior to the development of electrical energy

in the late 19th century, sufficient heat could only be supplied through combustion techniques such as oxy-acetylene. Between 1880 and 1900, the electrically derived welding processes of carbon arc welding, arc welding, and electrical resistance welding were developed. For the most part, most significant metal structures continued to be riveted together prior to World War II.

Metal-arc welding was first used for ship construction during World War I, though its use was principally limited to repairs. The use of welding increased with development of the requisite technology and the first all-welded ocean going ship was constructed in 1921. Inert-gas arc welding and submerged arc welding were developed during this era. With the advent of World War II, a large emphasis was placed on the use of welding in the shipbuilding industry because of the need to produce thousands of warships and merchant vessels in a timely fashion.

1.2 Modern Uses of Welding

Welding has continued to evolve over the years, borne by the need for higher quality, economical welds and new material development. Old welding techniques were refined as technology developed. There are many instances where a new welding process was developed in response to a new technology being discovered; laser, electron beam, and ultrasonic welding processes are examples.

1.3 Problems in Welded Structures

Problems in welded structures can be traced to two general but closely related areas: design of the welded structure, and the welding process used on the structure. During World War II, welding technology advanced so rapidly, naval engineers were unable to keep up with design innovations to design welded joints properly. Further, metallurgists were equally challenged to address the problem of cleavage fracture which led to shortened service lives and failures of welded structures. This is a problem that persists to this day.

Since World War II, there have been a great many advances in welding science and technology. At present, an emphasis has been placed on using high strength steels in shipbuilding applications, and particularly in naval ship construction. These materials have an advantage of a high strength to weight ratio which permits a subsequent reduction in overall structural weight. Such a reduction in the displacement of a hullform directly translates into smaller propulsion plant components and, ultimately, a smaller ship overall. In this way, significant savings in fuel and equipment costs will be realized over the service life of the ship. However, exotic and high technology materials usually are more expensive than conventional steels and more difficult to join. Because of this, the costs associated with fabrication, and particularly the costs associated with welding, can be quite high. Most submarines in the U.S.Navy are constructed from HY-80, a quench-and-tempered steel with a yield strength of 80 ksi that has been in use since the late 1950's.

USS SEAWOLF, SSN 21, the newest submarine in production, costing over $2 billion, is being made of HY-100. Although extensively studied and tested prior to being certified for submarine construction, and with elaborate procedures specified for welding (NAVSEA, 1990), the use of HY-100 has been fraught with problems. A significant portion of the SSN 21 pressure hull had to be scrapped because of cracks that were found throughout the welded areas. The problem was so widespread that there was no possibility of performing a cost effective repair. Not only was this a tremendous waste of material, but it resulted in a significant setback in schedule, as well as a very large increase in cost. The exact cause of the cracking has not been released to the public as of this writing.

It is therefore important to understand the basis of the cracking phenomena in high strength steel weldments in order to reduce or eliminate their occurrence. Inherent within such an undertaking is the need to detect or identify cracks within a weldment. This study focusses on microcrack formation in some materials either common to the shipbuilding industry or with potential applications. In addition, a new, non-destructive testing technique for visualizing weldment surfaces will be explored: the confocal scanning laser microscope.

Chapter 2

Background and Theory

2.1 Overview

While many diverse alloys may be welded, the body of this study centers its discussion on the welding techniques and alloys used in naval shipbuilding. A complete treatise on the subject is well beyond the scope of this study. Here, submerged arc and gas metal arc (GMA) welding of mild steel, HY-100, HY-130, and HSLA-100 are addressed, along with the feasibility of the application of a new NDT technology, the confocal laser microscope, to welding.

In welding, the heat source, usually an electric arc, supplies a great deal of concentrated heat to the weldment, melting the material and forming a weld. This heat produces complex thermal cycles which in turn cause (a) changes in the microstructure of the heat affected zone, (b) transient thermal stress and metal movement, (c) residual stresses and distortions in the weldment, and (d) ultimately, largely define the useful life of structures. The thermal cycle of a weld is shown in Figure 1. (Masubuchi, 1980)

The basic knowledge of material behavior and weld construction will be discussed as a necessary basis for understanding residual stresses. Further, cracking mechanisms unique

to the welding environment will be introduced along with their relationship to residual stresses and the solidification process. It is necessary to have a firm grasp of these concepts when observations of a weld surface are made with the laser microscope.

The following discussion on material behavior and welding is largely based on the publications of Brick, Clark and Varney, Courtney, Masubuchi, and Popov. More current information is used to augment the framework established by these researchers. This information was obtained in a literature review that was conducted to determine the current thoughts and areas of interest in the particular areas. Portions of the literature review were made possible through the efforts and cooperation of Stephanie Douglas. The review of recent publications in these specific areas should not be viewed as comprehensive, but a significant number of papers were reviewed. (Brick, 1977) (Clark, 1962) (Courtney, 1990) (Masubuchi, 1980) (Popov, 1968) (Douglas, 1992)

2.2 Non-Destructive Testing and the Laser Microscope

An underlying yet major objective of this investigation was to explore the feasibility of applying a new technology to welding practices used in shipbuilding. Specifically, the possible application of the confocal scanning laser microscope (CSLM), as a new non-destructive technique for an in situ inspection to reliably predict the service life of ferrous welds. In practice, there are several non-destructive techniques that are well established

in industry for inspection of ferrous based weldments. These include magnetic particle testing (MT), dye penetrant testing (PT), ultrasound testing (UT), and visual testing (VT). All of these inspection methods are used after the weld has been completed.

Each of these techniques has inherent limitations which is why more than one technique may be used in the inspection of a particular weld. The applicability and limitations for these techniques are discussed in Appendix A.

Note that controlling weld quality is not limited to feedback from post welding inspections. In-process feedback systems have been in development for some time. Recently, a great deal of effort has been directed towards development of robotics with automated, intelligent, in-process weld inspection technology. These systems, which employ techniques such as laser visualization and sophisticated image processing, permit real-time feed back capabilities to control welding parameters. (Agapakis, 1987) (Agapakis, 1990)

Since aspects of visual inspection may be enhanced through magnification with good resolution, an enhanced version of VT can be achieved through the use of the He-Ne CSLM. The confocal imaging system uses the coherent light of a scanning laser and conventional light microscope optics, combining them with a beam splitter and photodetector array. This permits rapid identification of specific areas of a large image that are in focus. As the microscope is swept through the range of focus positions

necessary to visualize all levels of a surface, an image processor collects sequential in-focus areas. A full picture is constructed in much the same way as a jigsaw puzzle picture: each individual piece is an in-focus image assembled to form a large image from which meaningful information may be extracted. Thus, high magnification of rough surfaces is possible with maximum resolution of 0.25 μm. Additional details regarding the specifications, optical theory, and operation of the laser microscope appear in Appendix B.

Currently commercially available, the confocal scanning laser microscope provides a great deal of real-time high resolution visualization of surfaces at high magnification. For inspection of weld surfaces and adjacent areas of baseplate, effective display magnifications of 1200x and 2400x have been found to be the most useful.

In its current configuration, the CSLM has the following advantages and limitations:

Surfaces may be examined in situ, or through the use of plastic replicas. Making a replica is analogous to obtaining a plaster cast of footprints. A cellulose acetate sheet softened with an acetone solution is used instead of plaster of Paris. Resolution has been observed to be good to 0.1 μm. These castings may be taken for study elsewhere by optical of electron microscope. The replication technique is discussed in Appendix C. (Ladd, 1992)

Only surfaces are visualized. The surfaces must be clean and dry, although a wet objective lens can be used.

The surfaces must present a sufficient amount of reflectivity for the laser light. Most metals provide adequate amounts of reflectivity. Problems arise when metal samples are very highly textured, as in a fractured surface, or in instances where the plane of the surface is tilted far from the perpendicular to the impinging laser light, as in the case of the surface of a weld bead. Many of these problems can be solved using the instrument's capabilities as long as they are not too severe.

Resolution limit: 0.25 μm with Nikon Optiphot 100x 0.95NA objective lens.

Magnification limit: 6000x when using the 12 inch B&W monitor and a 100x objective lens. Note the 1.5 mm pixel size on the 12 inch diagonal screen limits the displayed resolution.

A permanent record is possible through the use of photographs of the display screen, video tape, or printouts using an optional printer.

The machine consists of four cabinets which permits a level of portability. In all, the system takes up the space of a desk top. Thus, the device may be transported to the job site. While the equipment is transportable, in its current configuration,

it is not designed for the rigors of an industrial environment. Further, since the device is intended for laboratory use, the laser microscope is not easily used on welds in situ, however, this problem can be surmounted through the use of replicas. Solving these problems through equipment design and refinement will not entail a great technical challenge.

The equipment is expensive. A basic black and white system costs in excess of $250,000 (1992 dollars), a significant capital investment.

Use of the CSLM, like many of the other NDT techniques, focusses on detection of features that are at the surface of a material. Because it has a distinctive array of features and advantages, this new inspection technology fills a unique niche and serves to complement the existing NDT techniques that are in wide use.

Because this is a newly developed technology, little has been written addressing its application to welding. Some researchers are utilizing a scanning laser acoustic microscope, SLAM, to characterize the microstructure of advanced materials. (Kessler, et al, 1985) The SLAM is capable of providing surface visualization similar to the CSLM, but it also has the capability to use ultrasonic energy to interrogate the internal microstructure of optically opaque materials. Ultrasonic frequencies on the order of 500 Khz are used. A focussed laser beam combined with an optical system act as a small point-to-point ultrasonic detector. Coupled with rapid real time imaging (30 images per second), the ultrasonic capability makes it possible to achieve high resolution images on

the order of 1 μm. The SLAM technique can detect internal structures including porosity, lack of bonding, cracks, and voids. It can also detect changes in the elasticity of the material. When deep penetration inspection of a material is required, low frequency acoustic energy is used. The major disadvantages of the system are that it requires an immersion fluid for ultrasonic coupling and that significant flaws found near the surface can hide problems that lie at deeper depths. This limits its potential for large industrial applications.

2.3 Anatomy of a Weld

A cross section of a weld is shown in Figure 2. The welded area is composed of the fusion zone, the zone of partial melting, the heat affected zone, and the base metal. While these regions are macroscopically distinct in appearance and properties, on the microscopic scale their boundaries are not. The system is a continuum and one zone fades or blends into another in small transition regions.

The fusion zone, FZ, often called the weld, is composed of a localized coalescence of metals produced by heating the materials to the welding temperature. The materials in this area come from: (a) the base metal, (b) the filler metal (if any is used), (c) fluxing materials (if any are used), and (d) elements of the welding environment including shielding gases and contaminants.

A zone of partial melting, PMZ, exists in the base metal immediately outside the fusion zone. In this region, the peak temperatures during welding fall between the solidus and liquidus temperatures. This region, which is often considered part of the heat affected zone, is a very thin layer of material.

The heat affected zone, HAZ, is that portion of the base metal that has not been melted, but whose mechanical properties or microstructure have been altered by the heat of welding. The size or thickness of the heat affected zone can vary considerably, depending on the materials involved and the welding process used. For example, in a gas-metal arc (GMA) weld of a HY-130 butt joint in 300 mm plate, the HAZ is approximately 3 mm thick and the PMZ is about 0.3 mm thick.

The region outside of the heat affected zone is undisturbed base material. Areas close to the heat affected zone undergo a thermal cycle through the welding process, but it is inadequate to cause any changes in the material.

2.4 Stress, Strain, and Related Topics

2.4.1 Stress and the Continuum

The simplest case to introduce stress is an axially loaded bar of constant cross sectional area, in tension. Under the action of the applied static force, F, internal forces are established within the material of the bar. Taking a cross section, A, of the rod perpendicular to its axis, the normal stress is:

$$\sigma = \frac{F}{A} \qquad (1)$$

The molecular nature of matter is long established, but in investigating material behavior, unless attention is being focussed on the atomic scale, or dislocation or grain size, it is often convenient to consider matter as a continuum. One must take care in using the continuum concept at the microscopic level. Depending on the application, the assumptions of uniform matter distribution become invalid at the scale of grains or on the scale of dislocation spacings. In these instances, matter can be assumed to be continuously distributed throughout its volume. This continuum concept permits the addressing field quantities such as stress, strain, and displacement as piecewise continuous mathematical functions.

For an arbitrary point, P, in a continuum, Cauchy's stress principle associates a surface traction or stress vector, T_i with each normal vector, n_j, which defines the orientation of an infinitesimal surface element containing P.

$$T_i = \sigma_{ij}\, n_j \tag{2}$$

In any coordinate system where the axes are mutually orthogonal, the condition of stress at any point within a body can be represented as a matrix. This second-rank tensor[1] is commonly referred to as a stress tensor. For the cartesian coordinate system:

$$\sigma_{ij} = \begin{vmatrix} \sigma_{11} & \sigma_{12} & \sigma_{13} \\ \sigma_{21} & \sigma_{22} & \sigma_{23} \\ \sigma_{31} & \sigma_{32} & \sigma_{33} \end{vmatrix} \tag{3}$$

The stress tensor can be thought of as a set of three stress vectors, or surface tractions acting on mutually orthogonal surfaces at a point; its elements are scalar quantities and are force intensities. Figure 3. The terms on the diagonal, σ_{11}, σ_{22}, and σ_{33}, define the states of normal stress; the off-diagonal terms define the shear stresses. The characteristic of symmetry of the stress tensor, where

[1]A second-rank tensor requires two indices to identify its components. A vector is a first-rank tensor, and a scalar is a zero-rank tensor. (Popov)

$$\sigma_{ij} = \sigma_{ji} \tag{4}$$

follows directly from the equilibrium requirements for a volume element. This implies that there are six independent quantities in the stress tensor. (Popov, 1968)

2.4.2 Strain

Materials deform under applied loads; strain is the magnitude of that deformation and, in the elastic regime, it is mathematically related to stress. In plasticity, the effects of strain histories preclude such relationships. For the bar under uniaxial load, above, if the initial length is l_o and the final length is l, then the elongation per unit length of bar is the linear strain:

$$\epsilon = \int_{l_o}^{l} \frac{1}{l_o}\, dl = \frac{l \quad l_o}{l_o} \tag{5}$$

For the displacement vector, u_i, the linear strain is

$$\epsilon_{ij} = \frac{1}{2}\,(u_{i,j} + u_{j,i}) \tag{6}$$

In most engineering applications, elastic strain is on the order of 0.1 to 1.0 percent.

It is important to note that since ε_{ij} is a function of displacement, u_i, strains cannot be independent of one another and a relationship must exist between them. (Popov, 1986) (Shames, 1975) This condition of compatibility is

$$\epsilon_{ij,kl} + \epsilon_{kl,ij} - \epsilon_{ij,ki} - \epsilon_{ki,lj} = 0 \tag{7}$$

and ensures the displacements are single valued.

A strain tensor may be constructed that is similar to the stress tensor and having the same property of symmetry and the same number of independent quantities:

$$\epsilon_{ij} = \begin{vmatrix} \epsilon_{11} & \epsilon_{12} & \epsilon_{13} \\ \epsilon_{21} & \epsilon_{22} & \epsilon_{23} \\ \epsilon_{31} & \epsilon_{32} & \epsilon_{33} \end{vmatrix} \tag{8}$$

2.4.3 Ut Tensio sic Vis

"The force varies as the stretch" is the linear relationship of stresses and strains first postulated by Robert Hooke in 1676. (Popov, 1968) In developing the mathematical relationships describing this behavior, the constitutive equations, the principle of superposition is used. The principle of superposition follows from the elasticity, equilibrium, and strain displacement relationships for small magnitudes of strain. For isotropic materials in elastic behavior, alternate complementary form of Hooke's Law are commonly expressed as:

$$\sigma_{ij} = \lambda \epsilon_{kk} \delta_{ij} + 2\mu \epsilon_{ij}$$
$$\epsilon_{ij} = \frac{1}{E}[(1+\nu)\sigma_{ij} \quad \nu \sigma_{kk} \delta_{ij} \tag{9}$$

where the Lamé constants, λ and μ, are functions of Young's Modulus, E, and the Poisson Ratio, ν.

$$\lambda = \frac{E\nu}{(1+\nu)\ (1-2\nu)}$$
$$\mu = \frac{E}{2(1+\nu)} \tag{10}$$

For most steels, E has values between 29 and 30 Mpsi; the Poisson ratio takes values from 0.25 to 0.35 for most engineering materials.

2.4.4 Stress-Strain Curves

Many common engineering materials, such as steels, exhibit a stress - strain behavior similar to that shown in Figure 4. (Kutz, 1986)

For small stresses the curve has an initial linear elastic region. Hooke's Law only applies for elastic loading conditions where complete recovery to the undeformed condition, $\varepsilon_{ij} = 0$, results from the removal of all stresses. More specifically, these relationships apply for stresses that lie below the proportional elastic limit (PEL) for the material. The PEL is the stress level where there is a deviation from linearity; so the PEL is the maximum stress that can be applied to a material without deviation from the linear proportionality of stress and strain. A related point, and one that is better suited for engineering practices, is the elastic limit (EL). The EL is often indistinguishable from the PEL and is the stress beyond which plastic deformation is present when applied stresses are removed. (Clark, 1962) (Kutz, 1986)

For applied stresses that exceed the elastic limit, the material enters the regime of plastic behavior. Much more complicated and diverse expressions have been developed to model

the stress - strain (σ - ε) behavior within the plastic regime. These models are based largely on empirical data obtained for material specimens isothermally tested under pure, uniaxial tension. It is sometimes customary to present the data as a nominal stress (force per undeformed, original area) versus engineering strain.

$$\sigma = \frac{F}{A_{undeformed}} \tag{11}$$

$$\epsilon = \frac{l - l_o}{l_o} \tag{12}$$

The shape of the σ - ε curves is a function of temperature, strain rate, the material, and other factors. The curves are obtained by loading a standard specimen statically in a tensile testing machine. The load is applied slowly enough to ensure that all parts of the specimen are in equilibrium at any time. There are two common methods for obtaining the information: controlling load rate and controlling extension rate. σ - ε curves are usually obtained by controlling the load rate, $\sigma_{11,t}$. ASTM Standard E8 requires the loading rate not to exceed 100 ksi/min. Alternatively, the strain rate may be determined by maintaining a constant strain rate, $\varepsilon_{11,t}$. Typically, $\varepsilon_{11,t}$=0.05 min^{-1} is used. (Kutz, 1986) For materials like mild steel that do not exhibit a rate dependence, the stress-strain behavior is similar to that shown in Figure 4. (Popov, 1986)

True stress can be used to construct a "true stress - strain curve," however, it is somewhat more difficult to do experimentally since true stress is

$$\sigma = \frac{F}{A_{instantaneous}} \tag{13}$$

Thus, the cross sectional area must be monitored as stress varies. For tests conducted at slow strain rates, this is not particularly difficult in regions where necking occurs since direct measurements of the necking area may be obtained using micrometers or calipers. Optical methods are also used.

2.5 Residual Stresses

Residual stresses are defined as those present in a material that is free of external forces or thermal gradients. Residual stress fields can usually be placed into one of two broad categories: macroscopic and microscopic residual stresses. (McClintock & Argon, 1966)

Macroscopic residual stresses are considered to be long range, extending over macroscopic dimensions of a material. This class of residual stress is most often considered when studying weldments. Microscopic residual stresses are of short range and are usually confined to parts of a material where a homogenous continuum view of

strain is no longer possible. These stress fields become important when considering solidification phenomena, crack formation, and grain boundary effects, discussed below.

From the principle of virtual work, for any arbitrary control volume:

$$\int_V (\sigma_{ij,j} + \rho b_i)\, dV = 0 \tag{14}$$

which is not restricted to elastic energy. Since the control volume is arbitrary the integrand must also vanish and the equation reduces to:

$$\sigma_{ij,j} + \rho b_i = 0 \tag{15}$$

This equilibrium equation must hold true throughout the weldment. Since body forces are often negligible compared to the magnitude of internal stresses, the equation may be further simplified.

Since residual stresses are not a result of external forces, they cannot produce a resultant force or a resultant moment. (Connor, 1987)(Masubuchi, 1980) Thus on any plane section:

$$\int \sigma dA = 0 \tag{16}$$

and about any point:

$$\int dM = 0 \tag{17}$$

The terminology used to refer to residual stresses is not standardized. The technical terms commonly used to describe residual stresses include: "internal stresses," "initial stresses," "inherent stresses," "reaction stresses," and "locked-in stresses." They all mean the same thing.

The scale over which residual stresses act varies from the atomic to the macroscopic. This study is concerned principally with macroscopic residual stresses.

In welded structures, large residual stresses develop as a result of the welding process itself. The welding process involves a complex series of metallurgical and chemical changes that occur over a wide range of temperatures in a relatively short period of time.

In a progressive welding process, a heat source moves along a weld joint, usually in a steady, continuous manner. For electrical welding methods, the electrical power available for welding, H, in Watts is given by

$$H = VI \tag{18}$$

While exothermic chemical reactions and phase transitions of metals also supply some energy to the welding process, these sources are negligible compared to the electrical power supplied from the arc.

The intensity of the welding arc, h, in joules/inch, is expressed as

$$h = \frac{VI}{v} \tag{19}$$

where v is the travel speed of the welding arc in inches/sec.

Not all of this energy is used in making the weld. Like any heat flow problem where high thermal gradients are established, heat is lost from the system through the well known mechanisms of conduction, convection, and radiation.

Heat is conducted to the workpiece and to the electrode. The majority of the heat in the welding process goes into melting the electrode and the base metal. Heat is also lost to the surrounding environment through radiation: energy is radiated from the electrode, arc plasma, base metal, and weld pool. Because not all of the available energy goes into the process of making the weld, an arc efficiency, η_a, can be addressed. The thermal equivalent of the electrical power, H, in joules/sec, is thereby

$$H = 0.24\ VI \tag{20}$$

and the net heat or effective thermal power of the welding arc, Q, is

$$Q = H\eta_a = 0.24VI\eta_a \tag{21}$$

This net heat, or effective thermal power of the welding arc varies greatly depending on the particular welding process being considered and on the materials being used. As seen in Figure 5, η_a can vary from 21% for an alternating current tungsten inert gas, AC TIG, process on tin to 99% for an AC submerged arc method on mild steel.

For any location along the joint, the weld metal and adjacent base material are heated past their liquidus temperatures and a large temperature gradient is established with the rest of the structure. Figure 6. The pool of molten metal is usually very highly agitated and

vigorous flow patterns develop which acts to mix the molten metal. In electrical welding processes, the vigorous mixing action comes as a result of electrical eddy currents and forces from plasma action. Convection plays an important role in defining heat transfer and the position of isotherms within the melt. It also largely determines the shape of the weld pool and associated solidification phenomenon. (Oreper, et al, 1983) This mixing action also facilitates chemical reactions with the fluxing materials and with the surrounding atmosphere. As the heat source passes a location, the weld pool begins to cool at that spot and contract. At the stage where the weld pool begins to solidify, it also begins to exert stresses on the surrounding heat affected zone and on the already solidified weld metal on the upstream side[2]. Initially, the newly solidified weld metal is near its melting point, relatively weak, and cannot exert much stress. Upon further cooling to ambient temperatures, the weld metal can exert stresses that attain the yield strength of the baseplate in some cases.

The pattern of residual stresses that develop in a welded joint is greatly influenced by the geometry of the joint, the number of weld passes, the type of welding process, interpass temperatures, the materials used, and other factors. For example, in butt joints, the portions of the joint that are already solidified are stressed in tension in a direction parallel to the weld axis. These tensile stresses are balanced by a compressive stress field in the base material. (Figure 7) Tensile stresses often develop transverse to the weld axis because of restraints in joint movement that originate from previous passes, or from other

[2]Relative to the moving heat source, any weld joint location that has already experienced the heat source is considered "upstream;" any location yet to experience the heat source is considered "downstream."

mechanical restraints. (Figure 8) In fillet welds, tensile stresses will develop parallel to the weld axis as well as across the face of the weld. (Figure 9)

Connor classifies residual stresses according to the mechanisms that produce them: namely, structural mismatching and the uneven distribution of non-elastic strains, including plastic and thermal strains. (Connor, 1987) The residual stresses in a weldment that has been cooled to ambient conditions can be seen as a combination of the two.

A discretized model illustrating the introduction and magnitude of residual stresses arising from structural mismatch has been discussed by Masubuchi. The model is shown in Figure 10. Three identical carbon steel bars are connected together at their ends. Initially, the system is at ambient conditions throughout and there are no initial stresses present. The central bar is subjected to a thermal cycle where it is heated to 1100 °F (593 °C), then cooled to ambient temperatures. The two side bars remain at ambient conditions for all time, t, and the system is maintained at equilibrium at any instant. From geometry, the stresses in the side bars, $\sigma_{11\,s}$, must be opposite in sign and half of the magnitude of the stresses in the middle bar, $\sigma_{11\,m}$. Since consideration is given only to axial stresses, the indicial notation can be omitted, hence

$$\sigma_s = -\frac{1}{2}\sigma_m \tag{22}$$

As the temperature is increased from T_0 to T, the bars respond elastically with a temperature dependant Young's Modulus, E_T, and linear coefficient of thermal expansion, α:

$$\frac{\sigma_m}{E_T} + \alpha(T - T_0) + \frac{\sigma_s}{E} = 0 \qquad (23)$$

or

$$\sigma_m = -\alpha(T - T_0)\,\frac{2E}{1 + \frac{2E}{E_T}} \qquad (24)$$

Figure 11 shows the temperature dependence of yield stress of several materials. Eventually, the temperature, T, rises to the point where the middle bar has achieved its yield strength, σ_y.

In applying this scheme to a weldment, the middle bar is considered to be the fused metal, and the two side bars are considered to be the base material. Geometric considerations imply that this model is particularly applicable to butt welds.

The second class of residual stresses is that which arises from unevenly distributed nonelastic strains. These strain distributions may result from a plastic deformation of a

material, or from the large temperature gradients that are developed in the welding process. The strain tensor, ε_{ij}, may be decomposed into elastic and plastic strain tensors, thus:

$$\epsilon_{ij} = \epsilon^{e}_{ij} + \epsilon^{p}_{ij} \tag{25}$$

As previously discussed, thermal strains are related to the coefficient of linear thermal expansion and the change in temperature:

$$\epsilon^{p} = \alpha(T - T_0) \tag{26}$$

Although this equation has been written in scalar notation, it is understood that in anisotropic materials, the coefficient of thermal expansion may vary along a given direction. Connor states that thermally induced plastic strains have no shear components. (Connor, 1987) This implies they are principal, however, this may be achieved through the proper transfer of coordinate axes. Principal strains are represented as:

$$\epsilon^{p}_{ij} = \begin{vmatrix} \epsilon^{p}_{11} & 0 & 0 \\ 0 & \epsilon^{p}_{22} & 0 \\ 0 & 0 & \epsilon^{p}_{33} \end{vmatrix} \tag{27}$$

Further, these thermally induced elastic and plastic strains together satisfy the constitutive and compatibility equations, discussed above. The equation of compatibility may be rewritten as:

$$\epsilon^{e}_{ij,kl} + \epsilon^{e}_{kl,ij} - \epsilon^{e}_{ij,ki} - \epsilon^{e}_{ki,lj} - R = 0 \qquad (28)$$

Where R is the incompatibility:

$$R = \epsilon^{p}_{ij,kl} + \epsilon^{p}_{kl,ij} - \epsilon^{p}_{ij,ki} - \epsilon^{p}_{ki,lj} \qquad (29)$$

When the incompatibility is not zero, $R \neq 0$, residual stresses will exist. Thus, the incompatibility can be considered the cause of residual stresses. If the elements of plastic strain are single linear functions of position, then R=0 and residual stresses will not occur. (Connor, 1987) (Masubuchi, 1980)

It is not uncommon for the individual components of a weldment to have some inherent stress distribution prior to welding. The initial residual stress patterns of weldment components will influence the development of the final stress pattern distribution after welding. Residual stress patterns in plates can be established through application of many metal forming techniques. This requires inhomogeneous plastic deformation, such as is produced in bending and rolling operations.

A number of these techniques can also change the material properties of plates and introduce "texture", a preferential orientation of grains which results in anisotropic behavior. The act of rolling plate to size changes the grain structure, particularly near the surfaces of the plate. Strains on the order of 1 are required for this to occur. Individual grains become flattened and elongated in the direction that the plate was rolled.

This change in the grain structure also changes the way the plate responds to applied loads, thus the material can be changed from being homogenous and isotropic to displaying a very anisotropic behavior. Thus, the stress distribution can be quite different compared to what would be present in a corresponding homogenous material since the σ-ε behavior has a directional dependence. For these reasons, it is important to know the rolling direction when obtaining specimens for testing. Obtaining specimens for a Charpy V-notch impact test is a good example of where this is important. Figure 12.

Other metal forming operations that also influence residual stress patterns include: some grinding operations, shot blasting, and peening the surface of a metal. Each of these result in a complex stress pattern to be developed where compressive forces are established at the surface. Figure 13. Conversely, high temperature grinding operations can result in tensile residual stresses at surfaces when the metal is cooled to ambient conditions. This condition can result in premature yield when the metal is stressed. Castings often have complicated stress patterns distributed within them due to uneven cooling.

Heat treatment techniques such as quenching can also introduce internal stress distributions in materials. This is particularly important for quench-and-tempered materials such as HY-80/100/130.

Residual stresses in weldments have two serious consequences: first, they may produce distortion and second, they may even result in premature failure of structures through a variety of mechanisms. Microcracks observed on the surfaces of weld beads and in the surrounding baseplate are caused by the residual stresses of welding. It is well established that fatigue fracture of metals originates from minute cracks at their surfaces. (Miller, 1991) This is discussed in greater detail, below.

Masubuchi classifies residual stresses according to the mechanisms that produce them: (a) residual stresses from structural mismatching, and (b) residual stresses produced by uneven distribution of non-elastic strains which include plastic and thermal strains. In order for thermally induced residual strains to exist, it is necessary to have inhomogeneous plastic flow that remains when the material is cooled to ambient conditions and ΔT is returned to zero.

When the weld does not cool uniformly, the resulting non-uniform thermal shrinkage results in the development of stresses throughout the welded region. The weld joint strains elastically in response to these stresses and the forces often become sufficient to warp or distort the weldment. The magnitude of the distortion is largely dependant on the

geometry of the joint, the design of the structure, and the materials used. For example, in butt joints, a longitudinal and transverse shrinkage or contraction is common. Angular rotation of the baseplate about the weld axis may occur when the weld face shrinks faster than the weld root. In addition, a transverse bending in the plate may occur. Figure 8. Transverse and longitudinal shrinkage as well as angular plate rotation can be observed in fillet welds as well. (Figure 9)

2.6 Prediction of Residual Stresses

Residual stresses that occur during the fabrication of welded structures are considered to be in one of two general classes: residual welding stresses that are produced in the welding of unrestrained members, and residual stresses that are caused by external restraint. (Masubuchi, 1980) Restraining the elements of a weldment before and during welding is necessary to reduce the distortion that would normally result from the action of residual stresses. After welding a complete structure, the restraints are often removed and the welds themselves act to restrain the elements.

A typical distribution of both longitudinal and transverse residual stresses in a single-pass weld in a butt joint is shown in Figure 7. The stresses of principal concern are those parallel to the weld axis, σ_{11}, and those perpendicular to it, σ_{22}. The stress distribution is characterized by the maximum stress in the weld region, σ_{max}, and the width of the

tension zone of residual stress, b. In weldments made in low carbon steel, the maximum residual stress, σ_{max}, is usually as high as the yield strength of the weld metal, $\sigma_{y\,(WM)}$. The distribution of residual stress may be approximated by:

$$\sigma_{11} = \sigma_{max} \left\{1 - \left(\frac{x_2}{b}\right)^2\right\} \exp\left\{-\frac{1}{2}\left(\frac{x_2}{b}\right)^2\right\} \qquad (30)$$

Typically, the residual stress field parallel to the weld axis decays essentially to zero over a distance several times the width of the weld metal. A review of residual stress distributions published by Masubuchi and Connor indicate that b is approximately 4 times the weld width. (Masubuchi, 1980) (Connor, 1987)

In plates joined by a butt weld, the stress distribution may be considered to be 2-dimensional when the plate is less than 1 inch thick.[3] Thus,

$$\sigma_{ij,3} \approx 0 \qquad \{t_p : 0 < t_p \leq 1\ inch\} \qquad (31)$$

For plates over 1 inch in thickness, the variations in stress in the x_3 direction, $\sigma_{ij,3}$, become significant. (Masubuchi, 1980) This is also expected whenever the profile of a

[3]Consider the plate to be lying parallel to the x_1-x_2 plane; the x_3 axis then is oriented perpendicular to the plate.

weld varies greatly in the x_3 direction. A bead-on-plate weld may be considered an extreme case of this.

The principle of superposition may be applied when considering additional low stress levels imposed upon the weldment. Such is the case when a weldment is placed in tension, compression, bending, twist, etc. In these cases, as long as the yield strength is not exceeded, the final stress distribution is a linear combination of the residual stresses and the stress field developed from the applied load.

Linear superposition is not valid for large applied loads where the residual stress curve approaches the yield strength of the material. In the case of tensile stresses applied parallel to the weld, the residual stress curve flattens as the applied stresses increase. Figure 14. Eventually, general yielding occurs across the cross section, and the effect of the residual stresses on the stress distribution becomes insignificant.

When the applied stresses are removed, the structure will contain a residual stress distribution that is "less severe" when compared to the original configuration. (Connor, 1987) This means that the residual stress profile will be flatter overall. Figure 14. This will become important when considering the 4-point bend experiment, below.

2.7 Measurement of Residual Stresses

Residual stresses in a body cannot be determined by measuring the stress change that occurs when an external load is applied to a body. As a result, many of the tests used to determine residual stresses are destructive tests, involving cutting or drilling of a specimen and the strain change resulting from removing stress is measured. Volumes have been written on methods and techniques to determine residual stresses in steel. Generally, the methods can be grouped into one of four classes: (Masubuchi, 1980)

Stress-Relaxation Techniques

X-ray Diffraction Techniques

Techniques by Use of Stress Sensitive Properties

Cracking Techniques

Stress relaxation techniques may use electrical or mechanical strain gages, or may employ brittle coatings or etched grids. These methods have been specialized for applications to plates, tubes of cylinders, and for 3-dimensional objects. They usually involve a destructive procedure such as cutting or drilling. These techniques do not lend themselves to microscopic stress field evaluation.

X-ray diffraction using film or a diffractometer is a method that gives stress information on a molecular scale. These procedures are non-destructive, but time consuming and costly. The results are of questionable accuracy.

Techniques based on stress sensitive properties usually consist of ultrasonic or hardness methods. Although non-destructive, these methods have not been adapted for general use in industry; they principally reside in the laboratory.

Cracking techniques have been devised based on hydrogen induced or stress-corrosion cracking. At present, these methods are in their technological infancy and are restricted to the research laboratory. These procedures are useful for when studying residual stresses in complex structural models where a complicated residual stress field exists. These destructive methods only supply qualitative information.

The important point here is that there is no non-destructive method that can divulge the residual stress distribution of a weldment over an area of microscopic size. Thus, the presence of residual stresses in a weldment is largely conjectural and based on a history of destructive tests or on observations of cracks and other stress induced phenomena.

This is where the laser microscope may find true usefulness. The instrument can be used as a device to perform inspections of weldments. Microcracks and other surface features that are indicative of future problems and particular failure modes may be identified. The

weldment service life may be predicted based on studies that determine the conditions necessary to precipitate failure from these surface features.

2.8 Cracking in Weldments

2.8.1 Residual Stresses and Cracking of Weldments

Weldment cracks are caused by localized stresses that exceed the ultimate strength of the metal. Cracks can also initiate from defects in the metal and occur at stresses lower than the ultimate strength. In either case, these cracks usually do not show evidence of deformation. Considering the conditions under which they form, there are two general categories for cracking in weldments: hot cracking and cold cracking. Their characteristics are summarized in Table 1.

2.8.2 Hot Cracking

Hot cracking occurs at elevated temperatures, at or near the bulk solidus temperature, T_{BS}. Examination of the iron-carbon phase diagram shows steels to have a bulk solidus temperature that varies with carbon content. For construction steels, T_{BS} can vary from approximately 1550°C to 1400°C. (Figure 15) A low carbon content is preferred in steels

because steels with high carbon content are susceptible to a variety of cracking phenomena. Many common ASTM and MIL-S steels have a carbon content of approximately 0.2%. This weld metal solidification cracking is prevalent in nickel and aluminum based alloys, and austenitic stainless steels. Its presence in ferritic steels varies widely but can be a serious problem in high strength quenched and tempered steels such as HY-80/100/130. It can also be exacerbated by high heat input welding processes on thick sections that have highly restrained joints. (Dixon, 1981)

In the welding process, these cracks form during or immediately after welding, during the initial stages of cooling. The thermal shrinkage associated with the solidification process is on the order of 2-6% and imposes strains across the liquid films at the dendrite interface, causing them to rupture. These form the nucleation sites for cracking, discussed below. These cracks occur both in the weld metal and in the heat affected zone immediately adjacent to the fusion zone. Hot cracks are intergranular cracks, following grain boundaries. If open to the atmosphere, the crack surfaces generally show a layer of oxidation.

Hot cracking can occur in a number of forms in a weldment. The primary type of hot cracking is weld metal solidification cracking which can occur in the weld or in the heat affected zone.

2.8.2.1 Characterization of Hot Cracks:

Dixon reports a proposed classification scheme for hot cracks. Here, hot cracks are classified by the mechanism of their formation and the location in which they are found. (Dixon, 1981) The gross characteristics of this classification system are shown in Table 2.

Thus, high temperature cracking consists of Type 1, Segregation Cracking, and Type 2, Ductility-Dip Cracking. Each of these mechanistic classes are further subdivided by crack location.

2.8.2.2 Type 1, Segregation Hot Cracks:

Type 1, or segregation hot cracks, are associated with micro-segregation of phases which leads to intergranular films of low melting point, T_m. Segregation and its relationship to the phase diagram are discussed below. Type 1 is further divided into three sub-classes:

Type 1A Segregation Hot Cracks in 1° Weld Metal:

Primary, 1°, weld metal cracking upon solidification occurs when segregation provides a two-dimensional path of low cohesive strength. The strains that

develop from thermal contraction of the solid phases cause cracks to form within this weak region.

Type 1B Liquation Cracking in the HAZ:

Liquation refers to the partial melting of the grain boundaries. Liquation cracks are found in the HAZ where the peak temperature of the thermal cycle remains below the bulk solidus temperature, T_{BS}. The intergranular regions, which typically have a lower T_m than the metal they surround, may be liquified during the thermal cycle. These films may then provide paths for grain boundary separation from the stresses of welding.

Type 1C Liquation Cracking in 2° Weld Metal:

Type 1C hot crack is a liquation crack similar to Type 1B, but found in multipass weld metal. Here, the secondary, 2°, weld metal (a previous pass) undergoes a thermal cycle in a subsequent pass similar to that required for the formation of Type 1B cracks. So this is really a HAZ crack where the base material is a previous weld pass.

2.8.2.3 Type 2, Ductility-Dip Hot Cracks:

A reduction in ductility is observed in some alloys at temperatures immediately below their recrystalization temperatures, therefore, ductility-dip cracks may occur in these alloys. Designated as Type 2 hot cracks, these cracks occur at newly migrated grain boundaries. Unlike Type 1 hot cracks, the Type 2 crack is always devoid of any low T_m films. Type 2 hot cracks typically require higher strain levels for formation than do Type 1 cracks. These cracks have been observed in austenitic steels and nickel based alloys.

The subdivision of Type 2 cracking is similar to that used for Type 1 hot cracks, although it appears in a different order. See Table 2. This inconsistency is a source of confusion. A better classification scheme is proposed in Table 3 where the differences from the Hemsworth plan are underlined in bold.

2.8.2.4 Theory of Hot Cracking in the Weld Metal

Several theories exist to explain the mechanisms of hot cracking. At present, the two most widely accepted explanations have been put forward by Borland and Prokhorov. (Dixon, 1981) These theories share the same basis of crack initiation site formation, but only Prokhorov considers the effect of residual stresses growth rate. A discussion of the common theory is necessary.

2.8.2.4.1 Weld Metal Solidification

During continuous welding processes, a pool of molten metal is formed and moves along the weld line. Characterized as being in a quasi-equilibrium or steady-state condition, a layer of continuously solidifying material follows the molten pool. Figure 16. The dimensions and geometry of the weld pool and solid-liquid interface varies with welding parameters such as heat input, thermal gradients, and materials used. The weld metal may solidify either by cellular or dendritic growth initiated from the fusion boundary.

High temperature gradients, such as those which are produced by Tungsten-Inert Gas (TIG) welding, lead towards a cellular grain growth. For lower temperature gradients, characteristic of processes such as submerged arc welding, dendritic growth is prevalent. However, GMA is used more often in ship construction compared to TIG welding. Thus, this investigation concentrates on GMA processes.

Dendritic growth initiates from the liquid-solid interface of the molten metal pool and the base material. Dendrites which nucleate on this interface always lie along specific crystallographic directions. (Ashby, 1980) As cooling continues, specific dendrite orientations, those that are nearly perpendicular to the advancing solidification front, become dominant as dendrites of other orientations are cut off or blocked. As crystallization continues, solute is rejected at the solid-liquid interface. The preferred

dendrite orientation ultimately results in the characteristic grain pattern of a weld cross section shown in Figure 17. Refer to the Fe-C phase diagram shown in Figure 15. The non-equilibrium lever rule is used to find the composition of a solidified binary alloy at the dendrite-liquid interface.

$$C_s = kC_0(1-f_s)^{k-1} \tag{32}$$

Where C_s is the interface composition when the weight fraction, f_s, is solid; C_0 is the initial alloy composition; C_l is the composition of the liquid in equilibrium with the solid phase.

From the tie line of a phase diagram, the partition ratio, k, for a constituent is the ratio of the solid phase composition to the associated liquid phase composition in the associated adjacent liquid at any specific temperature:

$$k = \frac{C_s}{C_l} \tag{33}$$

2.8.2.4.2 Segregation and Crack Initiation

Different elements in steel have different equilibrium partition ratios. When k takes on values less than 1, C_l will always be greater than C_s and the liquid phase will always have a higher concentration of the particular constituent than the associated solid phase. Thus, metals containing elements such as sulfur which have k<1 will show a capacity to exclude or segregate the constituent into the liquid phase. This results in a liquid phase of progressively higher concentrations of solute surrounding the growing dendrites with a subsequent lowering of the T_m. Although the bulk of the liquid remains ahead of the solidification front, dendrite interlocking occurs and pockets of liquid become isolated from the solidification front, forming localized films of low T_m. Eventually, the entire weld is solidified but it is far from being homogenous: concentration gradients of solutes vary considerably through the weld. These principles imply that the solutes which have values of k<1 will be in a higher concentration in those areas that were solidified last. (Masubuchi, 1980) Since the physical properties of a material vary with changes in its makeup, the response of various portions of the weld to applied stresses is expected to vary greatly.

Coincident with dendrite growth is the thermal generation of stresses across the region behind the solidification front. These forces may cause interdendritic cracks, providing initiation sites for the growth of solidification cracks, but most of these areas will be

"healed" by the flow of metal from adjacent pockets. (Dixon, 1981) When this repair mechanism is no longer possible, permanent cracks are formed.

2.8.2.5 Hot Cracking Mechanisms

2.8.2.5.1 Shrinkage-Brittleness Theory

A semi-rigid network of dendrites is constructed from the dendrites that grow towards each other and interlock. Contraction strains develop until a critical rupture strain is met and fissures are generated. The "healing" process repairs these initial cracks as long as liquid flow is possible between the liquid pockets. Cracking occurs as the weld transits through a "brittle temperature range", BTR, which covers the temperatures from when the primary dendrites first interlock to just below the solidus. Once the local temperature drops below the solidus, the strains in the metal are more uniform. The metal can then absorb thermal strains without cracking. The tendency of a material to exhibit these cracks is believed to be related to the extent of the BTR, where the larger the BTR, the more susceptible the material is to hot cracking. (Dixon, 1981)

2.8.2.5.2 Strain Theory

Pellini, et al propose that cracks cannot occur during the "mushy" stage of solidification since shrinkage strains are uniformly distributed. Cracking is caused by the presence of [low T_m] liquid films between solidification grains.

2.8.2.5.3 Borland Generalized Theory

The theory developed by Borland is based on the Shrinkage-Brittleness and Strain theories and is discussed by Masubuchi and Dixon. (Masubuchi, 1980) (Dixon, 1981) The solidification process is considered to comprise four stages:

1. Primary Dendrite Formation
2. Dendrite Interlocking
3. Grain Boundary Development
4. Completion of Solidification

Figure 18 illustrates the relationship between the Fe-C phase diagram, the solidification process, and susceptibility of a material to undergo hot cracking.

Primary Dendrite Formation

The solid phases are dispersed in the liquid with both phases capable of relative movement.

Dendrite Interlocking

Dendrites have grown to sufficient size so as to contact and interlock. Thus, both liquid and solid phases are continuous, but only the liquid is capable of relative movement and so can move with relative ease between the dendrites.

Grain Boundary Development

Materials become susceptible to hot cracking once they have entered this stage of solidification. Crystal growth continues and the ability of the liquid phase to flow becomes restricted. "Healing" of the dendrite fissures can occur in so long as liquid can flow to the trouble spot.

The continually developing shrinkage strains can be accommodated provided they do not exceed a critical value. Strains beyond the critical value produce permanent

crack initiation sites and perhaps permanent cracks. Borland refers to the temperature range over which this stage occurs as the critical solidification range, CSR. As the size of the CSR increases, the material is more susceptible to formation of hot cracks.

Towards the end of this phase, the solid crystals are in an advanced stage of development. Because of extensive solid bridging between the interlocked dendrites, the liquid phase is no longer free to move about and no relative movement of the two phases can occur. The liquid phase is effectively relegated to discrete pockets.

Completion of Solidification

The remaining liquid has solidified.

While the presence of a wide freezing range is necessary for hot cracking to occur, the liquid phase must also be distributed in a form which allows high shrinkage stresses to build up between the grains. This condition is satisfied when the liquid phase is distributed over nearly all grain surfaces. If the liquid were confined at the triple points

of the grain boundaries, large areas of grain surfaces would closely join and be able to withstand large strains without forming cracks except at the triple points.

Quantitatively, Borland suggests that the distribution of the liquid phase during solidification is governed by the ratio of the liquid-solid interfacial energy, γ_{LS}, and the grain boundary energy, γ_{SS}, which approximately sets the wetting angle, θ:

$$\tau = \frac{\gamma_{LS}}{\gamma_{SS}} = \frac{1}{2\cos(\frac{\theta}{2})} \ldots \quad (34)$$

θ, the wetting angle, is also referred to as the dihedral, or contact angle.

Low values of τ, on the order of 0.50, are bad since almost all surfaces are covered with liquid phase; conversely, high values of τ, on the order of 0.58, are good since the liquid phase is restricted to localized regions of grain triple points. (Figure 19)

2.8.2.5.4 Prokhorov's Theory of Hot Cracking

The previously discussed theories have introduced the concept of a critical level of internally generated thermal stresses and strains, and temperature bands, combined with the morphology and mechanisms of the solidifying weld metal. However, they have not

addressed the rate of strain development or the effect that strain rate has on crack initiation.

Prokhorov describes the weld metal crack susceptibility as being related to the temperature and the strain rate within the solidifying metal. The brittle temperature range, BTR, delineates the band of temperatures over which cracking will occur. The lower end of the BTR is the temperature just below the solidus where the strength of the grain boundaries is sufficient to resist the thermally induced shear (versus normal) stresses. The upper limit is the temperature at which the liquid phase is prevented from circulating around the grains.

Within the BTR, the liquid-solid metal is ductile and can absorb limited strain. Most of the strain is accommodated by the localized shearing of ductile intergranular phases. Too large a strain rate produces higher stresses and ruptures in the grain boundary films, creating cracks.

2.8.2.5.5 Theory of Hot Cracking in the Heat Affected Zone

During welding, the heat affected zone experiences temperatures between the solidus and liquidus temperatures and partial melting of the grain boundaries occurs. Tensile stresses resulting from cooling contractions produce strain concentrations in the grain boundaries

which may develop into cracks. These cracks are usually small and are termed "microcracks."

Masubuchi and Martin proposed a quantification of the critical stress for forming an intergranular microcrack in the HAZ. (Masubuchi, 1980) Here, grains are assumed to be surrounded by soft materials that have a low critical shear stress. This facilitates deformation by permitting sliding along the grain boundaries when a low level of stress is applied.

Previous researchers had suggested that wedge-shaped microcracks form as a result of the intersection of two slip planes. Based on these earlier studies of creep fracture, Masubuchi and Martin proposed the critical stress for formation of an intergranular crack in the HAZ is:

$$\sigma_{cr} = \kappa \sqrt{\frac{\gamma_{SFE}\, E}{d}} \qquad (35)$$

where κ is a coefficient; γ_{SFE} is the surface free energy of the grain boundary material. E is the Young's Modulus of the grains, and d is the grain diameter. γ_{SFE} is reduced when liquification occurs, resulting in a lower threshold for the critical stress. σ_{cr}. Note that this equation is only applicable in the elastic regime.

2.8.2.6 Weld Metal Constituents and Hot Cracking

The composition of the weld metal and the base metal play an important role in determining the susceptibility of a particular weldment to hot cracking. It has been known for some time that hot cracks are much less prevalent in mild steel weldments than in structures made of high strength material such as HY-80, HY-100, or HY-130. Usually, hot cracking can be minimized or eliminated by suitably adjusting the composition of the weld metal or base metal using the tenets of Borland's generalized theory of super-solidus cracking. Detrimental films would be avoided and the CSR would be reduced in scope. This is fine in principle, but impractical in application, since many of the materials that are deemed harmful from a pure Borland theory view are necessary for the metallurgy to produce a steel with the desired characteristics of strength, etc. The relative hot cracking potency of elements in iron-binary systems are listed in Table 4.

The individual elements that effect hot cracking include carbon, sulphur, phosphorous, manganese, oxygen, silicon, aluminum, niobium, cerium, copper titanium, and boron. In ferritic welds, carbon, sulphur, phosphorous, niobium, copper, boron, and nickel are considered crack promoters. Manganese, oxygen, cerium, and chromium are regarded as crack inhibitors. There is disagreement in the literature regarding the effects that silicon, aluminum, and titanium have towards hot cracking susceptibility.

The following discussion of selected elements is derived from studies performed by Dixon and by Masubuchi:

Aluminum:

Aluminum is used as a deoxidizer. In small amounts, it will reduce one of the beneficial effects oxygen provides of inhibiting hot crack formation. In larger concentrations, aluminum combines with sulfur, forming (Al,Fe)S, and reduces susceptibility to cracking.

Dixon reported that aluminum concentrations of 0.005% or higher produce Type II sulfide films in steel castings. Some investigators report these films at aluminum concentrations as low as 0.002%. When the aluminum content approaches 0.01%, Type III particles begin to appear. (Dixon, 1981)

Carbon:

Essential for the formation of high strength steels, carbon is universally considered a cracking promoter.

Phosphorus:

Considered an impurity, phosphorus reduces notch toughness and promotes solidification cracking. The importance to increasing crack susceptibility is under debate, although cooling rate may play an important role in conjunction with the material. A Fe - Fe_3P eutectic exists with a melting point of 1050 °C which probably increases crack susceptibility. (Dixon, 1991)

Manganese:

Most authors consider manganese to be a crack inhibitor due to its interaction with sulfur. It has been reported that a magnesium-to-sulfur concentration ratio of up to 50 substantially reduces hot cracking.

A quantitative measure of hot cracking sensitivity of a low-alloy high strength steel has been proposed by Inagaki:

$$S_{HC} = \frac{C\left[S - P + \frac{Si}{25} + \frac{Ni}{100}\right]}{3Mn - Cr + Mo + V} \times 10^3 \qquad (36)$$

where concentrations are in percent. When S_{HC} <4, the material is considered to have a good resistance to hot cracking.

To prevent hot cracking in steel weldments, Inagaki proposes the constituent parameters detailed in Table 5.

2.8.2.7 Welding Parameters and Hot Cracking

The welding parameters pertinent to ship construction that effect sensitivity to hot cracking include: weld surface profile, dendrite growth pattern, travel speed, arc oscillation, heat input, flux, plate strength and thickness, preheat, and joint preparation. Any welding parameters that raise the level of strain across the solidification front will increase the sensitivity towards hot cracking. These parameters are generally related to the geometry of the joint and include: concave surface profiles, high weld depth/width ratios, increased plate thickness, unsatisfactory joint preparation, and localized preheat treatments tend to promote cracking. Cracking may be reduced by controlling the solidification structure. This can be accomplished by using shallow joint profiles, arc oscillation or pulsation, and multipass welding.

2.8.2.8 Reduction of Residual Stresses and Reheat Cracking

Residual stresses in weldments can be a real problem since they cause initiation of phenomena such as hot and cold cracking. There are techniques that have been devised to reduce the residual stresses in weldments which include: material selection, joint design and preparation, control of welding parameters, and post welding heat treatment.

McPherson describes the process of reheat cracking which is a special form of hot cracking that occurs when a weldment undergoes stress-relief heat treatment. Steels containing vanadium appear to be particularly susceptible to this phenomenon. Here, cracking occurs under the action of residual stresses in the HAZ over a range of temperatures as the assembly is cooling to ambient temperatures. For low alloy steels, reheating must exceed 1100°C, then reheat cracking occurs between 550°C and 650°C.

Originally, reheat cracking was thought to be caused by alloy carbides being taken into solution during austenization in the weld HAZ. Carbides, such as V_4C_3 and Mo_2C, precipitate out to strengthen the grains by restraining dislocation movement. This ultimately leads to the constraint of deformation in the grain boundaries until the local stress exceeds the available grain boundary ductility.

Presently, other factors are now considered to be involved in the process. It is suggested that trace concentrations of Al, Cu, B, P, S, As, Sb, and Sn may reduce the ductility of grain boundaries. Towards this end, steels doped with Al and Cu showed some evidence

of embrittlement and steels doped with B to levels as low as 3 ppm in the presence of Al showed evidence of severe embrittlement. The other impurities showed no apparent effect. Other factors which may influence reheat cracking are welding procedures and joint geometry which determine the residual stress level and distribution. (McPherson, 1978)

This phenomenon emphasizes the need to control welding parameters to reduce residual stresses. Removing these stresses may lead to serious flaws in the weldment. In many cases, performing stress relieving operations may not be possible. This is particularly true in the materials which have been strengthened through heat treatment. The quenched-and-tempered steels considered in this study, HY-80/100/130, fall into this category. The specifications written for these materials specifically prohibits such post welding heat treatments. (NAVSEA 1990)

2.8.3 Cold Cracking

Cold cracking is commonly referred to as hydrogen cracking, hydrogen induced cracking, hydrogen assisted cracking and delayed or hydrogen delayed cracking. These names reflect the importance of the presence of hydrogen in crack susceptibility of high strength steels. Cold cracks form at temperatures below 204°C and are usually transgranular, appearing in the FZ and in the HAZ. Generally, the susceptibility of the HAZ to cold

cracking increases with the base metal yield strength. Formation of cold cracks is generally associated with the formation of martensite in the weldment and is dependant on martensitic structure, the amount of diffusible hydrogen present in the FZ and HAZ, and on the magnitude of residual stresses present. (Masubuchi, 1980) (Kasatkin, 1985)

There are two general classes of cold cracks that are distinguished by the length of time they take to form. These are short time cold cracks and delayed cold cracks. (Masubuchi, 1980)

Short Time Cold Cracks

Short time cracks initiate as the weld cools down to ambient temperatures.

Delayed Cold Cracks

Delayed cracks initiate after some time at ambient conditions. The time period between initial cooling to ambient conditions and the onset of cracking can be from days to months in length. This is the basis for the portion of MIL-STD-1688A(SH) which specifies that HY-80 and HY-100 welds be subjected to MT testing for 7 days from the time the welding and postheat period is completed and the weldment has attained ambient temperatures. (NAVSEA, 1990)

2.8.3.1 Carbon Equivalent and Cold Cracking

The elements that are in the base metal play a large role in defining the susceptibility of a steel to cold cracking. The concept of Carbon Equivalent, CE, is a parameter that is widely used both as an approximate register of the ability to harden a steel and as a method to predict cold cracking tendencies. CE is based on the effect carbon has to increase susceptibility to cold cracking through martensite formation and subsequent effects from atomic hydrogen. The effect a specific component has is empirically derived from experiments and a mathematical expression for CE can be constructed to predict cold cracking susceptibility. There are a number of formulas used to quantify CE based on the chemical composition of the steel.

For low alloy steels, the American Welding Society defines carbon equivalent as:

$$CE_{AWS} = C + \frac{Mn}{6} + \frac{Ni}{20} + \frac{Cr}{10} + \frac{Cu}{40} - \frac{Mo}{50} - \frac{V}{10} \qquad (37)$$

Using this formula, for CE values that exceed 40, the steel will show a tendency to form underbead cold cracks. (Phillips 1960, Masubuchi 1980)

The International Institute of Welding defines CE to be:

$$CE_{IIW} = C + \frac{Mn}{6} + \frac{Cr + Mo + V}{5} + \frac{Ni + Cu}{15} \qquad (38)$$

The Japanese Society of Steel Construction uses:

$$CE_{JSSC} = C + \frac{Si}{30} + \frac{Mn + Cu + Cr}{20} + \frac{Ni}{60} + \frac{Mo}{15} + \frac{V}{10} + 5B \qquad (39)$$

which is valid in the range of 0.07% to 0.22% actual carbon content of the steel. (Davidson, et al, 1989)

It is interesting to note the conflicts between these expressions. For some components, such as molybdenum and vanadium, not only do their effects vary in magnitude, but also in sign, indicating detrimental effects for positive values and beneficial effects for negative values. Thus, one must take care to know the specific applications for which the expressions were intended. The CE formula for conventional C/Mn pipe steels (not shown) will not properly predict cold cracking susceptibilities for newer microalloy steels.

2.8.3.2 Thermal Cycles and Phase Transformations

The thermal cycle experienced by the metal in the FZ and in the HAZ determines the final microstructure upon cooling. The ferrite of the melt transforms to austentite then back to ferrite upon cooling. In quenched-and-tempered steels, a similar transformation occurs in the HAZ where martensite is transformed to austenite and back. During these phase transformations, impurities present in the alloy tend to diffuse toward the austenitic grain boundaries. It is the presence of the grain boundaries in the temporary austenite phase that promote intergranular fracture. (McMahon, 1981)

The cooling rate has a significant effect on the grain size of the martensitic microstructure within the HAZ. Very rapid cooling rates produce a fine grained microstructure which is found to be less susceptible to cracking. A controlled cooling rate after the martensitic transformation temperature with an isothermal holding cycle and the application of preheat also reduce the susceptibility cracking. (Kasatkin, et al, 1985)

2.8.3.3 Hydrogen Effects

Molecular hydrogen is the major culprit behind cold cracking and principally originates from water and hydrocarbon contamination of the weld materials. The high temperature

plasma of the welding arc dissociates water into hydrogen and oxygen.[4] Thus, the presence of water in the welding atmosphere, welding rod, flux, and on the weld metal becomes an important consideration towards the reduction of cold cracks. Hydrogen is a normal component in the atmosphere and shielding gasses are used to flush it away from the weld site.

For materials that show a sensitivity to hydrogen cracking, elaborate measures are taken to reduce hydrogen sources. Refer to the HY-80/100 MIL-SPEC as an example. (NAVSEA 1990) Diffusible hydrogen levels can be controlled by managing welding parameters such as the time and temperature conditions of cooling, the size of the weld, and the initial hydrogen concentration in the arc atmosphere. The primary source of hydrogen found in welds is from the moisture contained in the welding electrode. Hydrogen levels on the order of 9-10 ppm is sufficient to cause cracking in HY-80. (Nippes, 1988) This level decreases with increasing yield strength. Weld preheat, postheat, and high interpass temperatures increase the amount of hydrogen that diffuses from the weld and decrease the susceptibility to cracking. (Wong, 1988)

[4]Scavengers such as Al are used to eliminate oxygen from the melt pool. Oxygen can also effect the cracking resistance of high strength steel. The cracking susceptibility and intergranular fracture increases with an increase in oxygen content. Matsuda found that intergranular fracture surfaces including oxygen have many microvoids and microcones. Inclusions near the prior austenite grain boundary cause microvoids and microcones on the intergranular fracture surface. Oxygen concentrations in the range of 15-210 ppm are sufficient to cause cracking in HY-130 weldments. (Matsuda, 1985)

Hydrogen may be internal or external to the weldment. External hydrogen at elevated partial pressures can initiate cracks st the surface of the metal. Internal hydrogen can collect in heavily dislocated slip bands that form from impurity segregation and serve to initiate subsurface cracks. (McMahon, 1981) When subsurface initiation does occur, there is evidence that it occurs at locations of maximum triaxial stress. Whether originating internally or externally, hydrogen travels to areas of maximum triaxial stress by normal lattice diffusion or dislocation transport. Once hydrogen is available at these sites, cracks can be initiated and may grow through intergranular cracking, interphase cracking, by acceleration of microvoid coalescence at carbide particles, or by transgranular cleavage. The "trapping" strength of hydrogen can effect the cracking rate in different microstructures. Hydrogen can be trapped in defects in steel that include dislocations, impurity atoms, inclusion particles, interfaces between the matrix and carbide particles, internal cracks and voids, and grain boundaries. (Thompson, 1981)

The amount of diffusible hydrogen can be controlled by factors such as the time and temperature conditions of cooling, the size of the weld, and the initial hydrogen concentration in the arc atmosphere. The primary source of hydrogen found in welds is from the moisture contained in the welding electrode. Hydrogen levels on the order of 9-10 ppm are sufficient to cause cracking in HY-80. (Nippes, 1988) This level decreases with increasing yield strength. Weld preheat, postheat, and high interpass temperatures increase the amount of hydrogen that diffuses from the weld and thereby decreases the susceptibility to cracking. (Wong, 1988)

Oxygen can also affect the cracking resistance of high strength steel. The cracking susceptibility and intergranular fracture increases with an increase in oxygen content. (Matsuda, 1985) Matsuda discovered that intergranular fracture surfaces including oxygen have many microvoids and microcones. Inclusions near the prior austenite grain boundary cause microvoids and microcones on the intergranular fracture surface. Oxygen concentrations in the range of 15-210 ppm are sufficient to cause cracking in HY-130 weldments.

The thermal stresses induced during welding are attributed to the restraint of free thermal expansion and contraction by the surrounding structural elements in a welded structure. In the HAZ of butt welds, the transverse residual stresses induced by external restraint govern the formation of cold cracks in this region. In longer welds on thick plate, the stresses and strains produced by internal restraint are triaxial and are due to inhomogeneous heating and cooling. (Thompson, 1981) If these residual stresses exceed a critical level, cold cracking can occur. This level is known as the critical stress. The presence of hydrogen in the lattice structure weakens its cohesive strength and will lower the critical stress required to initiate cracking. Residual stresses can be reduced by the use of preheat, interpass temperatures and post weld heat treatment. (Brednev, 1990) (Kasatkin, 1985) In thick sections where multipass welds are used, the majority of the weld will be tempered by the heat of subsequent welding passes. (Brooks, 1979)

Residual stresses at temperature are necessary to activate the process of intergranular slip, which is a necessary condition for microcracking. The likelihood of slip occurring along grain boundaries is governed by the possibility of activation of intergranular deformation, the grain size, and the grain structure. (Kasatkin, 1985) Inclusions and impurities around grain boundaries play an important role in the initiation of sub-microcracks during intergranular slip. The active process of growth of these sub-microcracks is caused by trapped vacancies initiated during rapid cooling, plastic deformation, and martensitic transformation. (Kasatkin, 1985)

Plastic deformation also occurs during the welding thermal cycle and can affect the susceptibility to cracking. Plastic deformation develops least when welds are cooled rapidly after welding and where conditions provide higher cooling rates from the martensitic transformation temperature. As the cooling rate is reduced, plastic deformation develops while cracks are forming. High rate of movement during the initial period after welding, the degree of preheat, and distribution of diffusible hydrogen, have a substantial effect on the deformation process and breakdown of the metal. (Kasatkin, 1985) During martensite transformation, the rate of plastic deformation in the HAZ is governed by the total density of mobile dislocations formed during the high temperature deformation of austenite as well as during the formation of martensite. Previous high temperature deformation along grain boundaries and the unstable structure intensify intergranular slip as the tensile stresses increase, at temperatures below 200°C. (Kasatkin, 1985)

The stress levels along with the hydrogen content affect the location and extent of cracking in a weldment. Cracks are shown to initiate and propagate in the HAZ, along the fusion line, when stress levels are low (near the critical stress level) and the hydrogen content is low. When the hydrogen content is high with low stress levels and the hydrogen content is low with high stress levels, cracks tend to initiate in the HAZ and propagate into the weld metal. The cracks initiate and propagate into the weld metal with high hydrogen content and high stress levels. The high hydrogen content is approximately three times higher than the low hydrogen content levels. (Kasugi, 1983) In the HY steels, HAZ cracking usually occurs perpendicular to the stress direction and is located underbead and removed from the toe on either side of the weld. Despite the orientation of inclusions parallel to the primary stress directions, these inclusions sometimes act as crack initiators.

The chemical composition of the metal greatly affects its resistance to cracking. Alloying elements which contribute to the hardness of a material are important in determining the susceptibility to cracking. These elements include carbon, manganese, nickel, chromium, copper, molybdenum, and vanadium. Carbon content is the most significant element in increasing hardness. The carbon equivalent relates the proportion of all of these elements to crack susceptibility. Hardness increases with increasing carbon equivalent. A hardened microstructure is more susceptible to cracking.

There are other measures used to assess crack susceptibility or resistance in a weld. The maximum critical stress is a commonly used parameter to evaluate cold cracking resistance. This stress is defined as the maximum stress at which the specimens do not fail within 24 hours. This parameter is influenced by specimen size, composition, and thermal cycle of welding. As specimen width increases, the critical stress decreases. The reduction in critical stress is influenced by the increasing degree of strain localization and formation and growth of a plane stress state with increasing width. The critical stress increases with the reduction in the mean cooling rate in the HAZ metal. This is due to the self-tempering of the resulting martensite, reduction of local microstresses and more efficient hydrogen removal from the HAZ. (Sterenbogen, 1987) This critical stress is often related to K_{Ic}, the stress intensity factor. Sterenbogen proposed a criterion for cold cracking resistance, particularly for large specimens: the ratio of the maximum critical stress to the yield limit. If this ratio is greater than one, then cracks do not form in the HAZ of the welded joint. Brednev suggests a criterion, A_{2cr}, which characterizes the critical energy capacity of local plastic deformation in delayed fracture of a welded joint, considering both force and deformation. A_{2cr} is defined as the product of the critical stress level and the critical local plastic strain.

2.9 Crack Propagation Under Static Loading

Within the weldment, there are two areas with quite different properties that must be considered. The baseplate and the weld to some extent may be considered ductile. The HAZ often exhibits a brittle characteristic. These two different material responses to applied loads result in different mechanisms of crack propagation. It is initially assumed that some cracks have been initiated through the action of thermal stresses as discussed above.

2.9.1 Elastic Deformation and Yielding

For ductile materials, failure under static loading is considered to initiate by a slow coalescence of voids.

2.9.2 Fracture Mechanics and Crack Propagation

When a material is brittle, fracture proceeds by the high velocity propagation of a crack across the brittle volume under load. Kutz states: Failure is predicted to occur in the multiaxial state of stress when the maximum principal normal stress becomes equal to or exceeds the maximum normal stress st the time of failure in a simple uniaxial stress test using a specimen of the same material.

2.9.3 Stress Fields and Microcracks

Globally, a condition of stress is estimated as a simple average measure of force per unit area. This assumes a homogenous, isotropic medium which is often a good approximation, based on the scale of observation. However, in a material where discontinuities are distributed within its volume, the stress field will have large variations on a macroscopic level. Discontinuities such as microcracks will have large stress concentrations at their tips. The stress field considered may be due to a residual stress field, an applied load, or to a superposition of the two.

A microcrack may be modeled as an ellipse which in the limit becomes a sharp crack. An ellipse in cartesian coordinates is described as:

$$\left(\frac{x_1}{a}\right)^2 + \left(\frac{x_2}{b}\right)^2 = 1 \qquad (40)$$

where the length of the major axis, 2a, is parallel to the x_1 axis.

2.9.4 Cracking Modes

The growth of cracks is categorized in terms of the orientation of the crack to an applied stress, and the type of applied stress. Refer to Figure 20.

Mode I Cracks:

Mode I cracks are cracks which have a stress field perpendicular to their major axis, and as such are also termed "opening mode" cracks. Here, the displacement is perpendicular to the plane of the crack.

Mode II Cracks:

Mode II or "sliding mode" cracks are characterized by a shear stress acting across the crack plane, parallel to the its long axis. The displacement of the crack surfaces is in the plane of the crack and perpendicular to its leading edge, thereby sliding one surface of the crack along the other.

Mode III Cracks:

Mode III or "tearing mode" cracks is caused by out-of-plane shear stress. Crack surface displacements are in the plane of the crack and parallel to its leading edge.

Although all three modes are present in a typical cracking situation, Mode I cracks are the most important. (Masubuchi, 1980) Further, in the 4-point bend experiment, discussed below, this is the principal crack mode of concern. This is because the laser microscope only sees those cracks open to the surface. In addition, the surfaces that were visualized were subjected to tensile stresses through a pure bending moment.

2.9.5 Stress Intensity Factor

Consider the case where a Mode I crack of length 2c along the x_1 direction is subjected to a uniform stress, σ, in the x_2 direction. For this crack which extends through the thickness of an infinite plate, the stress distribution is approximated as:

$$\sigma_{11} \approx \frac{K}{\sqrt{2\pi r}} \cos\frac{\theta}{2}\left[1 - \sin\frac{\theta}{2}\sin\frac{3\theta}{2}\right] \tag{41}$$

$$\sigma_{22} \approx \frac{K}{\sqrt{2\pi r}} \cos\frac{\theta}{2}\left[1 + \sin\frac{\theta}{2}\sin\frac{3\theta}{2}\right] \tag{42}$$

$$\sigma_{12} = \frac{K}{\sqrt{2\pi r}} \sin\frac{\theta}{2}\cos\frac{\theta}{2}\cos\frac{3\theta}{2} \tag{43}$$

The stress intensity factor, K, can be thought of as a measure of singularity at the crack tip. It is dependent on the crack geometry and on the imposed far field state of stress. K is not a measure of the stress concentration. For this example,

$$K = \sigma\sqrt{\pi c} \tag{44}$$

Note that along the x axis, $\theta=0$, and the stress tensor reduces to

$$\sigma_{\alpha\beta} = \frac{K}{\sqrt{2\pi r}} \begin{vmatrix} 1 & 0 \\ 0 & 1 \end{vmatrix} \tag{45}$$

In reality, specimens are not infinite in lateral dimensions, so a correction factor, α, may be added to equation (44):

$$K = \alpha\,\sigma\sqrt{\pi c} \tag{46}$$

where α is geometry dependant.

According to Griffith, crack growth will occur when the energy released during crack extension, U, is equal to the energy required for incremental crack growth, W. Thus,

$$U = W \tag{47}$$

Further, for an incremental distance of crack growth, da, it follows that:

$$U_a = W_a \tag{48}$$

These quantities denote the energy required for crack growth per unit distance and may be used as a measure of crack growth resistance for a material. When W_a is large, the material is crack resistant (fracture resistant) because it requires a large U_a for fracture. Conversely, when W_a is small, the material has a small fracture resistance. Fracture will occur when the energy released is very much greater than the energy required for growth.

Thus, the Elastic Energy Release Rate, G, is defined as:

$$G \equiv U_a \tag{49}$$

and the Fracture or Crack Resistance, R, is defined as:

$$R \equiv W_a \tag{50}$$

It is important to note that while R is a material property, G is problem dependant (geometry dependant).

From Inglis' solution for an elliptical hole,

$$G = U_{\rho} = \frac{2\pi\sigma^2 c}{E} \tag{51}$$

which indicates that the Elastic Energy Release Rate is proportional to the crack length, c, and to the square of the applied stress state.

From experimental work using a Mode I crack in a plate, there exists some initial crack length for which fracture will occur before general yielding. When this situation exists, the empirical relationship between initial crack length, $2c_0$, and the average fracture stress, σ, os a constant:

$$K = \sigma\sqrt{\pi c} = constant \tag{52}$$

Consequently, fracture occurs when the stress intensity factor, K, reaches a certain value that is material dependant. This Critical Stress Intensity Factor, K_k, is also termed the "fracture toughness" of a material and is a material property.

When the fracture stress approaches 0.8 σ_y, then the results deviate from the K = constant curve and structure is more ductile.

A surface crack in a plate of finite dimensions is much more complicated to model than an infinite plate with a through-crack. Here, a plate of width, W, and crack length, $2c_0$, is subjected to a tensile load, P. See Figure 21. The critical stress intensity factor may be expressed as:

$$K_{I_c} = \sqrt{\frac{6\pi\sigma a_0}{\frac{\sigma}{0.2}\left(\frac{\Phi}{\psi}\right)^2 - 1}} \tag{53}$$

where

$$\Phi = \int_0^{\frac{\pi}{2}} \sqrt{1 - \frac{c_0^2 - a_0^2}{c_0^2}\sin^2 e}\, de \tag{54}$$

$$\psi = \frac{P}{WB} \tag{55}$$

These equations are valid for specimens with width-to-thickness ratio, W/B > 6; initial crack depth, $a_0 < B/2$; and initial crack length, $c_0 < W/6$.

For a 4-point bend test, a notch bend specimen of width, W, and thickness, B, is subjected to a load P as shown in Figure 22. Here, the crack lies on the edge of the plate and runs the full thickness. The critical stress intensity factor may be expressed as:

$$K_{I_c} = \frac{\left(\frac{P}{B}\right)^2 \frac{L^2}{W^3}\left[34.7\frac{a}{W} - 55.2\left(\frac{a}{W}\right)^2 + 196\left(\frac{a}{W}\right)^3\right]}{1 - \nu^2} \qquad (56)$$

This equation is valid for specimens with a width to thickness ratio, $2 < W/B < 8$. Note the specific dimensional relationships of the load points in the 4-point bend test apparatus.

CHAPTER 3

Experimental

3.1 Overview

There are two main points to this investigation:

1. One point is the application of new technology, the confocal He-Ne laser microscope, to welding. The He-Ne confocal laser microscope was used extensively to visualize the surface of weld specimens. Additionally, other potentially beneficial applications of this NDT tool towards welding are explored.

2. Microcracks in high strength steel weldments were investigated. The He-Ne laser microscope was used to study the occurrence and growth of microcracks in weldments under static bending loads. This area constitutes a complement to two concurrent Master's theses performed at MIT:

An investigation of fatigue crack growth was performed by John Cushing at MIT. Fatigue crack initiation and growth in steel weldments were studied. The specimens Cushing used were mild steel with a weld bead

from an E70 electrode that was applied using GMA welding. (Cushing, 1992)

A study into the mechanisms of weld associated microcrack formation in various materials was accomplished by Stephanie Douglas. There, the laser microscope was used in inspection and visualization of several materials using a number of welding techniques. (Douglas, 1992)

3.2 Materials

Four baseplate materials were selected for their current and potential future uses in the shipbuilding industry: mild steel, HY-100, HY-130, and HSLA-100.

3.2.1 Mild Steel

"Mild steel" is a generic label for carbon steels with carbon content less than 0.3 percent. The mild steel used in this study is a relatively weak steel where yield strength, σ_y, is on the order of 30 kpsi. These metals typically have good weldability and good fracture toughness, principally resulting from a low carbon content. Mild steel is included in this

study as a control because it does not form cracks very easily. It has a low level of susceptibility to hot and cold cracking and is relatively easy to weld.

3.2.2 Q&T Steels

HY-80 was developed in the 1940's and was accepted for use in naval vessels in the late 1950's where it has developed a long and successful history. HY-80 is a shorthand notation for "High Yield: 80 kpsi yield strength". This is an example of a quenched-and-tempered steel. The use of these steels and their weldments in naval vessels is directly related to their extraordinary toughness, high strength, and deformation performance under high rate loading. The toughness and strength achieved in the HY-series steels is obtained with the use of relatively high amounts of alloying elements combined with a quenched-and-tempered (Q&T) heat treatment. The result is a martensitic steel structure. This structure requires the use of stringent welding process controls and specially designed filler materials to retain adequate properties in the as-welded condition. These precautions are needed to assure sound, crack-free welds due to the steel's sensitivity to hydrogen-related cracking. (Montemarano, 1986) (NAVSEA, 1990) (General Dynamics, 1977)

Two quenched-and-tempered, Q&T, steels were selected for study: HY-100 and HY-130. HY-100 has been in use by the United States Navy for many years in new surface ships

construction. It has recently been certified for submarine use and is the material selected for the SSN-21 USS Seawolf submarine pressure hull. The U.S. Navy is exploring the potential applications of HY-130 in naval shipbuilding.

3.2.3 HSLA Steels

HSLA means "High Strength Low Alloy." HSLA steels have potentially the same (or better) strength and toughness properties as HY-steels, but are obtained by a combination of "clean" steel processing, carefully selected, small amounts of microalloying elements, and heat treatments. This results in a steel with a ferritic microstructure that is easier to weld than the HY-steels.

The microalloying of HSLA steels results from small amounts of Al, B, Cb, N, Ti, and V which function in grain refinement and precipitation hardening to increase strength and toughness in a conventional C-Mn structural grade steel. These elements are present in concentrations of less than 0.15 weight percent. Additional increases are achieved with nominal amounts of Co, Cu, Ni, and Mo, the conventional alloying elements, combined with proper heat treatment. The quantity, shape, and size of inclusions are controlled. Microstructure transformation products are refined, and grain size and strengthening precipitates are controlled during rolling operations. The resultant low-carbon steels are

extremely weldable without the use of many of the stringent process controls required for the HY-steels. (Montemarano, 1986)

The key advantage of the HSLA steels over the HY-steels is their inherent weldability and attendant lack of preheat requirement as part of the welding process. Cost savings of $0.40 to $0.90 per pound of welded ship structures are estimated when comparing HSLA-80 to HY-80. (Montemarano, 1986)

At present, the U.S.Navy is supporting a HSLA research and development and certification program to evaluate potential uses in naval ships. For this study, HSLA-100 was selected as a material to compare to HY-100.

The elemental composition and properties of the materials used in this study are shown in Table 6. Carbon Equivalent, CE, is calculated using equation (37). Steels with values of CE > 40 show susceptibility to formation of underbead cold cracks. (Masubuchi, 1980) Hot Cracking Sensitivity is calculated using equation (36). Steels with $S_{HC} < 4$ are considered to have good resistance to hot cracking.

3.2.4 Origin

All materials were made available through the efforts of R. A. Bass who used samples of most of them in his MIT Master's thesis which explored an in-process method to reduce residual stresses in HY steels. (Bass, 1989)

3.2.5 Specimen Design

Utilizing beam theory, the dimensions of specimens used in the 4-point bend test were determined from estimating bending forces based on the yield strength of the strongest material to be tested (HY-130), and the capacity of the test machine.

The test fixture used for the 4-point bend test accepts specimens that are at most 6.35 cm (2.5 in) wide. In order to ensure the maximum residual stresses from welding and to minimize anticlastic curvature in the deformed state, the maximum width was adopted for the specimens. The baseplate for all of the metals was 1.27 cm (0.5 in) thick. Since the width-to-thickness ratio, W/t_p, is equal to 5.0, plate and shell theory is not really appropriate and beam theory was used for the design. Thus, the elastic stress in a beam is given by the well-known elastic flexure formula[1] which describes the axial stress

[1]Here, a right-hand cartesian coordinate system is used where the beam axis is parallel to the x_1 axis, the width of the beam is in the x_3 direction, and the displacement occurs in the x_2 direction.

distribution, σ_{11}, as a function of distance from the neutral axis, x_2. (Popov, 1968)(Shames, 1975)

$$\sigma_{11} = -\frac{Mx_2}{I} \tag{57}$$

M is the bending moment. For a symmetric bending experiment where l is the distance between the widely spaced support points, l_0 is the distance between the narrow support points, and P is the load:

$$M = \frac{l-l_0}{2}\,\frac{P}{2} = \frac{l-l_0}{4}P \tag{58}$$

In this case, the load experienced by all support points is P/2. Figure 23.

I is the moment of inertia of the cross sectional area about the centroidal axis when x_2 is measured from that axis. For a rectangular cross section of width, w, and thickness, t_p:

$$I = \int_A x_2^2 dA = \frac{wt_p^3}{12} \tag{59}$$

Combining these equations, the stress at the outermost surface of the beam specimen for any load, P, is

$$\sigma_{11} = \frac{P(l - l_0)}{t_p^2 w} \tag{60}$$

provided the stress does not exceed the yield strength of the material. This equation may be rearranged to determine the load required to achieve yield in a beam specimen:

$$P_{Yield} = \frac{t_p^2 w}{l - l_0} \sigma_y \tag{61}$$

The final specimen dimensions were calculated using characteristics of the strongest material, the testing device dimensions, and the capacity of the testing machine. HY-130 material characteristics were used to give the limiting case. The spacing of the load points for the 4-point bend test were 11.00 cm (4.331 in) and 25.00 cm (9.843 in) which were at the maximum limits of the testing apparatus. Since the plate was initially 1.27 cm (0.5 in) thick, the 10 klb maximum load of the testing machine was not a limiting factor. The finished specimen dimensions were 40.64 cm (16.00 in) long, 6.35 cm (2.50 in) wide, and 1.242 cm (0.489 in) thick. See Figure 24. The estimated forces required to attain yield for the four materials are shown in Table 7.

3.2.6 Specimen Fabrication and Welding

The material samples were prepared from mild steel, HY-100, HSLA-100, and HY-130 plate stock that was roughly 1.27 cm (0.5 in) thick. The steel plates were supplied with the direction of rolling clearly marked. This allowed the specimens to be laid out such that their major axes were parallel to the plate rolling direction. Specimens were flame cut at least 1.27 cm (0.5 in) oversized based on a 0.3 cm (0.125 in) slag and heat affected zone. Since flame cutting introduced metallurgical changes and residual stresses at the edges, it was necessary to trim this material from the specimen borders. Blanchard grinding was used to remove the affected material. The specimens were machined in a group which ensured they were all the same size.

The large surfaces of the plates were lightly Blanchard ground to remove mill scale and surface roughness on both sides. All specimens were surfaced in a group to ensure all samples had the same thickness. The specimens acquired a 16 machine finish. The smooth surfaces were needed to maximize the ability to observe surface features that might otherwise be obscured or undetectable on a rolled mill surface.

The final specimen dimensions were: 1.24 cm (0.489 in) thick, 6.4 cm (2.5 in) wide, and 40.6 cm (16.0 in) long. A length of 18 inches would have been preferred. This is based on studies performed by DeGarmo, but such a length was incompatible with the testing

apparatus.[2] (DeGarmo, 1946) Further, larger samples are impractical because of size and weight limitations of the laser microscope's specimen platform. Unnecessarily large samples would also waste limited resources.

Shielded arc welding was used to deposit weld beads on the plates. Weld beads were laid down the center of the plates along the long axis. Four specimens were prepared in this way, one from each of the materials being investigated (mild steel, HY-130, HY-100, and HSLA-100). Because cracks were desired in the specimens, no special preheating, postheating, or hydrogen shielding precautions were taken. E7014 weld rod was used to weld downhand at ambient conditions to produce beads that were 0.64 cm (0.25 in) wide and 0.25 cm (0.10 in) tall, on average.

Eight specimens were prepared. Their characteristics are summarized in Table 9.

3.3 Equipment

A Helium-Neon confocal scanning laser microscope, model 1LM11, developed by Lasertec Corporation of Japan, was used extensively throughout this investigation. Details of the theory and operation of the microscope appear in Chapter 3 and Appendix B.

---

[2]DeGarmo investigated residual stress distributions and their relation to test specimen length. 18 inches is the shortest length required in order to achieve the maximum longitudinal and transverse residual stresses for a nominal welding condition.

The 4-point test was performed on an Instron 8501 test machine. The arrangement of the test apparatus is shown in Figure 23. The assembly consists of two sets of rollers. All four rollers are 2.54 cm (1 in) in diameter and 7.3 cm (2 7/8 in) long and were spaced as shown in Figure 23. The upper set, designated as B1 and B2, are held in a massive, rigid jig that prevents significant movement relative to each other. In this way, they are moved as a rigid pair, allowing for some minimal amount of jig flexure. Two special B rollers, each with a clearance groove to accommodate the weld bead, were manufactured from drill rod. The lower set of rollers, designated A1 and A2, are similarly joined. The two sets of rollers can only move along the z-axis.

A load cell integral to the test machine senses loads which are then digitally displayed on a control panel. The rollers are positioned using hydraulics and can be controlled manually or by computer. During testing, the A rollers are moved and the B rollers are held in place. The z-axis position of the A rollers is also digitally displayed on the control panel.

The materials used to obtain replicas of the plate specimens were obtained from Ladd Research Industries, Inc., P.O. Box 1005, Burlington, VT 05402. Detailed steps used to obtain replicas and treat them for visualization beneath the laser microscope appear in Appendix C.

3.4 Experimental Procedure

Each specimen was tested using the following procedure:

1. Prior to applying any load to the specimen, the surface was cleansed and a replica was obtained to record the zero-load condition. An area surrounding the longitudinal center of the plate was used for the replicas. For the samples that were welded, this area included the weld bead and a portion of the baseplate immediately adjacent to the weld. (Figure 25) The same region was used for all subsequent replicas in order to study development of cracks in the baseplate and in the weld at different load levels. The center of the plate was used because it would be subjected to a symmetrical, if not uniform, bending moment.

2. With the two A and B roller sets widely spaced, the specimen was laid upon A1 and A2.

3. The A rollers and specimen were hydraulically raised under manual control until the upper set of rollers, B1 and B2, just make contact with the specimen. In order to ensure that the specimen is not prematurely loaded, the load cell output is monitored during this step.

4. Hydraulic pressure was manually increased in successive steps and the specimens were deformed through the applied bending moment. Therefore, the displacement of the rollers was the independent variable, and the load resulting from the bending resistance of the specimen was the dependant variable. The bending resistance was translated into force sensed by the load cell and was digitally displayed along with the position of the rollers. For each successive increase in roller displacement, both the roller position and the corresponding load level were manually recorded.

5. Manual control was maintained throughout the experiment because of the need to stop regularly and obtain a replica at different load levels. The motion of the rollers could have been computer controlled, but it was impractical to develop the program to do so. Further, manual control offered greater flexibility in performing the experiment and permitted parameters such as load step increments to be adjusted in real time.

Roller displacement was adjusted to achieve specific load level targets of 10, 20, 30, 40, and 50 kN. When these loads were achieved, the experiment was stopped and a replica was obtained in most cases. A replica was also obtained when the data indicated the specimen was yielding.

6. The specimens were loaded into the plastic regime where a final replica was taken at maximum load. The load was then fully released and the specimen was removed from the testing machine.

7. The replicas were shadowed with gold and observations were made using the laser microscope. See Appendices B and C.

CHAPTER 4

Results and Discussion

4.1 Initial Conditions

Prior to welding, all specimens were machined flat. The welding process introduced residual stresses into the specimens and caused them to distort. Since the weld bead was laid down the centerline of the long axis, distortion was bilaterally symmetrical and the specimens longitudinally curled slightly towards the surface that contained the weld bead. The magnitude of displacement from the planar condition was measured at the center of each specimen using a steel rule. The results of these measurements are shown in Table 8 and in Figure 26. Radius of curvature varies from 740 cm for mild steel to 2024 cm for HY-130. The radii of curvature are calculated from the geometric relationship for a section of a circle: (Beyer, 1980)

$$c = \sqrt{4h\ (2R - h)} \tag{62}$$

Where c is the chord length, h is the shortest distance from the center of the chord to the edge of the circle, and R is the radius of the circle. This expression is easily rearranged to solve for the radius.

$$R = \frac{c^2}{8h} + \frac{h}{2} \tag{63}$$

Yield strength error bars in Figure 26 represent the difference between nominal and measured strength, based on HY-130. HY-130 was determined to have an actual yield strength of 139 kpsi. The displacement error of ±0.01 inch (0.025 cm) is based on the graduations of the metal scale. Figure 26 shows this data to appear linear.

4.2 Load-Displacement Curves

The recorded data appear in tabular form in Appendix E, and graphically in Figures 27 through 31. All eight specimens were tested. Only HY-130 withstood loads in excess of 35 kN. Mild steel never supported loads in excess of 16 kN.

Load level was plotted against displacement in Figures 27 through 31 and are analogous to stress-strain curves. In all cases, the specimens initially exhibited a linear behavior indicative of elastic response. Deviation from linearity indicates yielding had occurred. Since stress could only be calculated for elastic behavior, converting the load information into corresponding tensile stresses using equation (60) would result in a large error. Once

the yield strength is attained at the outer fibers of the specimen, average surface tensile stress is maintained at that level as the load increases, except for strain hardening.

It is important to consider residual stresses at this juncture. The residual stress distribution parallel to the weld axis can be approximated by equation (30). As tensile stress is increased, the stress distribution shifts as shown in Figure 14, indicating the weld bead is the first region that yields. Furthermore, any cracks present in the surface of the weld, and particularly those which are subjected to Mode I geometries, would attain yield at their tips at average surface tensile stress levels below the yield strength. Such cracks would both widen and lengthen.

4.2.1 Mild Steel

Figure 27 shows the behavior of mild steel. The behavior of both the weld bead-on-plate (MS-W) specimen and the plain plate (MS-P) specimen are shown. The linear portion of the curve has a slope of 66 kN/cm. The maximum load sustained for the MS-W specimen is 15.6 kN; the MS-P specimen could only sustain 14.2 kN. This difference of 1.4 kN is due to the presence of the weld bead.

The weld bead is composed of a mixture of the E7014 welding rod and the mild steel baseplate. The welding rod metal has a rated yield strength of 70 kpsi, and the mild steel

has a 30 kpsi yield strength. (Table 6) This situation where the filler metal has a greater yield strength than the baseplate is termed "overmatching." (Connor, 1987) The metallurgy and physical characteristics of the fused metal are not known, but because the mild steel does not attain its strength through any heat treatments, it is expected that the weld metal has a yield strength somewhere between 30 and 70 kpsi. The MS-W curve is also shifted upwards from the increase in moment of inertia from the increased cross sectional area due to the weld bead.

Deviation from linear response occurs about 8.5 and 9.7 kN, indicating yield at the outer surface occurs within this load range. This is consistent with the predicted values of P_{yield} shown in Table 7. The significant results of the displacement-load curves are summarized in Table 10.

4.2.2 HY-100

The displacement-load response for HY-100 is plotted as Figure 28. The load response of both the welded (HY-100-W) and the plain plate (HY-100-P) specimens are shown. The specimens exhibit behavior similar to that seen in mild steel: there is an initial linear portion of elastic response followed by yield and a corresponding deviation from linearity. Both the welded and the plain plate specimens lie on nearly the same curve. The slope of the elastic response region is calculated to be 65 kN/cm which differs from the mild

steel response by 1.5%. Furthermore, the displacement-load responses of all of the welded specimens are identical within their respective elastic regimes. (Figure 31) This is consistent with the materials having the same Young's modulus. (Table 6) This is the "undermatched" condition where the weld bead has a lower yield strength than the baseplate. Relative to the mild steel case, the HY-100 weld appears to have a significantly smaller effect on the strength of the welded specimen when comparing to the plain plate specimen.

Figure 28 shows an initial deviation from linearity in the 23 to 26 kN load range. This is consistent with the yield strength of HY-100 which is about 3 times greater than mild steel. Recall that mild steel indicated first yield about 8.5 kN, and 3 times that value is 25.5 kN.

4.2.3 HSLA-100 and HY-130

None of the remaining materials showed a significant difference in bending resistance between the welded specimens and the corresponding plain plate specimen. Admittedly, of the plain plate specimens, only the HY-130 specimen (HY-130-P) was taken sufficiently well into the plastic regime to be able to make valid comparisons to the welded specimen (HY-130-W).

As indicated earlier, in all of these cases, the yield strength of the baseplate is larger than that of the filler metal. This is the "undermatched" condition. (Masubuchi, 1980) Little can be surmised about the yield strength of the weld metal without direct testing. This is because HY and HSLA steels attain their high strength through heat treatment. Most of this effect is lost when the metal is melted. Quenching the weld would serve to restore some of the lost strength, however, brittle structures would form in the metal structure. Undoubtedly, the yield strength of the fused metal is less than that of the baseplate. Further, the HAZ which had undergone a high thermal cycle probably is weaker and infused with brittle zones because no precautions were made to control hydrogen. The HY steels are particularly susceptible to this.

It is interesting to note that HY-100, which is known to have a yield strength of 139 kpsi, shows a significantly larger resistance to bending compared to HSLA-100. (Figure 31) This indicates that the actual yield strength of HSLA-100 is close to its advertized value of 100 kpsi.

4.3 Moment-Curvature Diagrams

A first order approximation of the bending moment-curvature relationship was constructed using the following method: (Refer to Figures 32 and 33)

In order to construct the moment curvature diagrams, four important simplifying assumptions were made regarding the 4-point bend test:

1. The portion of the specimen between the A rollers forms a segment of a right circular cylinder. This assumption really comes from simple beam theory. With a uniform, constant bending moment, the curvature will be constant except for minor variations due to cross sectional variation from the weld profile.

2. The regions of a specimen that lie between the A and B rollers remain planar throughout the experiment.

3. The planar regions are tangent to the circular region at their line of contact.

4. The lines of contact between the A rollers and the specimen remain at a constant distance from each other through the entire range of deformation. In addition, x-axis spacing between the A roller lines of contact and the B roller lines of contact remain constant through the experiment.

Some more complex methods in dealing with this deformation problem are addressed in Chapter 6.

These four assumptions result in the construction of two similar right triangles. sharing a common line which is tangent to a circle. One of the triangles has a corner coincident with the center of the circle. (Figure 32) From simple geometry, a relationship was developed to calculate the radius of curvature from the z-axis displacement data:

$$R = \frac{l_0}{2} \frac{1}{\sin\left(\arctan\left(\frac{\beta}{\alpha}\right)\right)} \tag{64}$$

where

$$\alpha = \frac{l - l_0}{2} \tag{65}$$

and β is the z-axis displacement measured from initial roller contact with the specimen (step 3 of the experimental procedure).

The bending moment is calculated using equation (58). Strain can then be calculated using:

$$\epsilon = \frac{t_p}{2}\frac{1}{R} \qquad (66)$$

It is known that the radius of curvature for an unloaded specimen is infinite. In the ideal case, the specimen is initially planar. This is a good approximation for the plain plate specimens which were machined flat. The welded specimens have some initial curvature, but the radii are large, varying from 7.40 m for mild steel to 20.24 m for HY-130. (Table 8) When the roller displacement is infinite, the radius of curvature would be equal to $l_o/2$. Equation (62) meets these requirements.

This is a first order approximation. Other assumptions could have been made to produce results of comparable accuracy with greater mathematical difficulty. For example, the shape of the specimen between the rollers could have been assumed to be parabolic instead of circular. Furthermore, friction, roller contact deformation, initial curvature, plate thickness, and other effects are not considered in the calculations.

The moment-curvature behavior of the eight specimens are plotted as Figures 34 through 38.

Examination of Figure 38 shows that the initial curvature present in each specimen corresponds to low levels of bending moment. Mild steel has the largest residual moment

at 125 Nm. The higher strength materials have considerably smaller values. No corrections are made for the initial curvatures in evaluating the data.

While it appears that equations (58), (62), and (63) are dependant only on the geometry and load, it is the material characteristics of the metal used that defines the load response to an applied displacement. In the elastic regime, the relationships are simply the slopes calculated in Table 10. The validity of the assumptions may be tested by comparing the calculated results to theory. From beam theory, the moment-curvature relationship is:

$$R = \frac{EI}{M} \tag{67}$$

Thus R varies as the inverse of M. For all of specimens examined, the Young's modulus is constant. Certainly, for all the plain plate specimens, the moment of inertia, I, is identical. The cross section of the weld bead varies slightly along the length of the welds. Based on bead height measurements, the variation in weld cross section was calculated to be less than 10%. However, the difference in the moment of inertia between a specimen with a weld compared to a plain plate specimen was calculated to be 7.6%. For a first order approximation of moment-curvature behavior, the moment of inertia for all specimens is taken to be the same.

Figure 38 shows the moment-curvature behavior for all of the welded specimens. The 1/M relationship of equation (67) is seen to be present in all specimens. The response to the applied bending moment deviates from theory when yielding begins. As expected, the mild steel shows the deviation from the 1/M functionality at the lowest level of bending moment, followed by HSLA-100, HY-100 and HY-130. This is simply a reflection of the linear conversion of the load-displacement data discussed above.

4.4 Replicas and Laser Microscopy

Replicas were taken of the specimens at various load levels following the procedure outlined in Appendix C. The replicas were subsequently shadowed with gold and studied using the confocal scanning laser microscope. 20x, 40x, and 100x objective lenses were used. Most of the imaging was performed using the 40x objective lens. This lens was obtained specifically for the purpose of inspecting areas adjacent to welds because it has a 10 mm stand-off distance. Normal lenses have a standoff distance of approximately 1 mm. This prevents visualization of the HAZ and adjacent weld because weld bead physically interferes with the lens body. Similar problems arise in studying the highly convoluted replicas obtained from the same area of the weldment.

A video tape was made of several replicas for record purposes. The position of the video tape counter and data relating to the sample were manually recorded to correlate the video images with specific samples. The video tape map is included as Appendix F.

After the replicas were studied under the laser microscope, the video was played back and black-and-white images were obtained from the video monitor. The photographs were taken using 35mm Kodak Tmax 100 film in a tripod-mounted Canon A-1 camera. A Tamron 80-210mm focal length lens was used at 135mm / f8 to reduce pincushion distortion of the images. To minimize vibration effects, the shutter was tripped using a cable release. The length of exposure was regulated by the camera circuitry. Photographic processing was preformed by a commercial vendor.

The photographs showing significant features are included as Figures 39 through 70. In several instances, composite photographs were constructed. Compared to single images using a lower power objective lens, composite pictures have the advantage of being able to examine large areas at higher resolution.

The correlation between images of replicas using the laser microscope, replica images using SEM, and the original specimen were recently verified at MIT. (Cushing, 1992) A specific experiment to establish this verification was deemed superfluous and was not performed. However, in practice, areas of some specimens were directly studied using

the laser microscope, based on replica information. In all cases, the resolution of the replica appeared to exceed the resolution of the video monitor.

4.4.1 General Baseplate Appearance

Figure 39 shows HY-130 baseplate in an unstressed condition, using the 40x objective lens. The image shows an area 120 μm long by 87.5 μm wide. The surface is covered with a series of criss-crossing, fairly uniform marks from the Blanchard grinding process. No cracks are seen. This photograph is shown as a typical example of the Blanchard ground surfaces of all the specimens. The scratches were quite shallow and exceeded the capabilities of the laser microscope to have their depths determined.

4.4.2 Mild Steel

Figures 40a and 40b show the same area of mild steel baseplate at two load levels. The direction of tensile loading through application of a bending moment is indicated. Prior to loading, no cracks were visible in this area. The small granular bumps are artifacts of the gold shadowing process. Note that they are not reproduced from one replica to the next.

Figure 40a shows the surface while the plain plate specimen experienced a load of 10 kN. Figure 27 indicates the specimen is in yield. Note the cracks forming along the edges of the Blanchard grinding mark. The orientation of the cracks to the direction of principal stress may indicate that the crack is forming through a combination of Mode I and Mode II cracking. Altematively, the fracture could be following a grain boundary, however, this is unlikely for the crack that follows the edge of the grinding mark.

Figure 40b shows this area of plating in full plastic yield at a sustained load of 14 kN. The cracks that were small in Figure 40a have grown substantially and interconnected. Some cracks branched to form legs that are transverse to the applied load. The black area of the photograph that indicates the location of the crack is misleading. In a replica, a crack manifests itself as a long peak instead of a crevasse. It has been observed that the impinging light of the laser microscope illuminates the specimen at a slight angle. This causes shadows to be cast by objects that have a sufficiently large slope and are oriented in any direction but that which is parallel to the incoming light. This anomaly is seen in several other photomicrographs included here. For this reason, the width of the crack is not easily discerned and results can be misleading. Therefore, the thick, black areas of Figure 40b may overestimate the true width of the crack.

Notice that there is a feature of the surface in Figure 40a that appears thread-like. In figure 40b, this feature forms the path of a large crack. This may be coincidence, or the thread-like feature may be a very thin microcrack.

Figure 41 shows a portion of the mild steel plain plate specimen at a sustained load of 14 kN, observed with the 40x objective lens. This composite photograph shows a cracking pattern that is, on the average, about 70° to the scratch pattern left by Blanchard grinding and 30° to the axis of applied stress. Both transgranular and intragranular cracking appear to be present. Note the granular artifacts are present.

Figure 42 shows the tip of a major crack in Figure 41. This image was obtained using the 100x objective lens. The true edges of the major crack are more easily discerned.

It is important to note that no material examined in this study exhibited baseplate cracking other than mild steel. The cracking that was observed in HY-100, HSLA-100, and HY-130 was always associated with either the weld or the HAZ.

4.4.3 HY-100

Figure 43 shows HY-100 at a zero stress state. No load is applied. The top 75% of this composite photomicrograph contains weld metal and the direction of the weld axis is indicated. The bottom 25% shows the adjacent baseplate, the beginning of the HAZ. This strip of photographs is continued onto Figure 44 to illustrate the variation in the features of the baseplate as distance from the weld increases.

There are four things commonly observed in these weldments:

1. baseplate surface
2. weld metal surface
3. oxide layers
4. slag

Most, if not all, of these items will appear in the welded specimens. Often, it is not easy to discern between some of them.

The baseplate surface has been described in Figure 39. The features vary with the preparation of the surface. Grinding, peening, cutting, etc, all have distinctive patterns and different surface features can be observed.

The weld metal surface has a highly irregular appearance. Widmanstätten structures are commonly observed in all welded specimens. A good example of this structure is seen in Figure 65. A pattern that appears to be a crack is visible in the extreme upper right hand corner of Figure 43. This feature is also visible in Figures 45 and 47 where it appears at the top of the photo, but closer to the middle. This crack-like feature appears to lengthen and branch as the load is increased. (Figures 47 and 47) While it appears to be a crack in the weld metal, this feature may also be an artifact from grain formation,

or a crack in an oxide layer lying atop the weld. Other similar features can be seen between the three photomicrographs.

The large black region that bisects the lower quarter of the photograph at an angle is not a crack. It is a region where the replica surface is at a large angle to the incident light. The result is that the light does not reflect back into the objective lens and so no features are discerned.

The baseplate immediately adjacent to the weld appears at the bottom of Figure 43. It appears rougher and has a granular appearance compared to Figure 39, the undisturbed baseplate. Many of the marks from Blanchard grinding have become distorted.

Locally, the weld-baseplate interface is not perpendicular to the long axis of the weld and appears angled. Short, irregular features, 13.8 μm long and 0.8 μm wide on average are scattered through this area. These appear to be microcracks, but they do not appear to grow under increased load. Figures 45, 46, 47, and 48 show the same weld and baseplate areas as in Figures 43 and 44. The differences are the load levels sustained at the time the respective replicas were taken.

Figure 44 shows baseplate from 87 μm to 375 μm from the weld. One image was inadvertently omitted when photographing the video tape. The rough appearance of the baseplate immediately adjacent to the weld gradually approaches the appearance of

undisturbed baseplate. (Figure 39) The surface appears to have a lumpy character in the areas between the Blanchard grinding marks. These first appear approximately 60 μm from the weld. Initially, the features are irregular in shape, roughly 2.5 μm in diameter, with a long axis perpendicular to the weld axis. By 100 μm from the weld, they become more circular in appearance. They eventually fade from the plate at a distance of 0.25 cm from the edge of the weld. In light of this, these features appear to be indicative of the HAZ.

Figures 45 and 46 show the same region as Figures 43 and 44, but here, the static load has been increased to 20 kN. For HY-100, this is within the elastic regime. (Figure 28) There are indications that the crack-like features in the weld metal region of Figure 43 have grown somewhat. This is not definitive and may be due to differences in the replicas themselves.

The small crack-like features of the HAZ do not appear to have changed. However, it appears that there is less resolution of the HAZ area in Figure 45 when compared to Figure 43.

Regions of Figure 46 show greater contrast than the corresponding areas of Figure 44. For this reason, there are some surface features that appear to be microcracks but are probably not. These features are about 16 μm long and 0.3 μm wide, irregularly shaped, and situated in random orientations.

Figures 47 and 48 show the HY-100 specimen at 33 kN load, corresponding to a strain of 0.009. (Equation (66)) The figures indicate this is well within the region of plastic deformation, so the entire weld and outer surface of the baseplate are in yield. Surprisingly, there is little change between the surface features observed for the 20 kN and the 33 kN load replicas.

Figure 49 shows a well developed crack in the weld metal of HY-100. This replica was obtained for the unloaded condition, so this is a crack that formed from the welding process. The axis of the weld is indicated. This crack was found approximately in the center of the weld and is perpendicular to its long axis. This indicates the longitudinal residual stresses depicted in Figure 7b had a major influence on its formation and growth. It is located at the crest of a small ridge in the weld. The end of the crack that appears in the lower right hand corner of the photograph is formed in an odd shaped crook, perhaps following a grain boundary. The opposite end of the seems to be branched into several arms. The crack is 169 μm overall. Stretched out, it would measure over 200 μm. The crack measures 3.1 μm wide.

Figure 50 shows this same crack under a 33 kN specimen load. The direction of the applied tensile stress is parallel to the longitudinal axis of the weld. The weld itself is oriented nearly perpendicular to the applied stress, implying that Mode I crack growth is expected. (Figure 20) The 33 kN load places the outer surfaces in plastic strain. (Figure 28)

Several significant changes have occurred from the unloaded condition of Figure 49. The crack has clearly grown wider and has been distorted, especially in the sections near the top of the photograph. The width has doubled in some locations, but the pattern of growth is not uniform. Although more detail can be seen in the upper portions of Figure 50 (compared to Figure 49), the crack does not appear to have increased in length significantly. This could be due in part to the orientation of the ends of the crack to the direction of the applied stress. The upper end of the crack is nearly parallel to the applied stress, so Mode II cracking would be geometrically preferred provided there were a sufficient variation in the local stress field. The lower end of the crack forms a crook, turning back on itself. No meaningful conclusions can be drawn in this case. The crack should have lengthened, but it did not.

4.4.4 HSLA-100

Figures 51 and 52 show HSLA-100 loaded at 0 kN and at 30 kN, respectively. The photomicrographs were obtained from the same general region of two separate replicas. In both cases, the images encompass a portion of the weld bead and adjacent baseplate.

The HSLA-100 weld and baseplate was very similar in appearance to the mild steel weldment. The weld appeared to have normal Widmanstätten structures, and no cracks

were observed. The baseplate appeared to have the granular appearance that faded with distance from the weld, again, becoming an indicator of the extent of the HAZ. This feature, which is readily detected visually on the video monitor, has not reproduced as well in the photographs.

Figure 53 contains the image of HSLA weld at a specimen load of 30 kN. A pattern of features was observed on the crest in the composite photomicrograph. A line of small ridges has formed in a pattern following the crest. Many appear circular in shape, the center neatly level with the surrounding material. The diameter varies from 6 μm to 10 μm. In the replica, the outlines are slightly raised ridges (corresponding to depressions in the original specimen) approximately 1.2 μm wide. These may be anomalies of an oxide layer, or they may indicate deformation about grain boundaries. No information was found regarding the grain size or shape within the weld with which to correlate the observations.

4.4.5 HY-130

Figures 54, 55, and 56 constitute a composite photograph of the weld and HAZ of HY-130 in the unstressed condition.

In Figure 54, the weld metal takes up the upper eighth of the photograph. There are two other small indications that may be cracks in an oxide layer. There appear to be two

cracks in Figure 54, both in the HAZ. The first is about in the center of the photograph. shaped like the letter "U." Both tips of this crack appear to be branched. The second crack appears on the right edge of the photo, nearly 2/3 of the way down. The first indication of a crack appears nearly 70 μm away from the weld There, it appears to follow a scratch from Blanchard grinding. 120 μm away from the weld, it abruptly changes into a jagged path, appearing to be intragranular cracking. It runs off the side of the composite photograph so its ultimate fate is unknown.

The bumpy, granular appearance of the baseplate in the HAZ begins about 85 μm from the weld. Initially, the bumps are small, about 1.5 μm in diameter on average. The phenomenon becomes pronounced at an approximate distance of 200 μm from the weld. Here, the bumps are fairly uniform in shape and average 2.5 μm in diameter. They can be seen to fade with distance from the weld. (Figures 55 and 56)

Figures 57, 58, and 59 comprise a strip of photomicrographs of HY-130 at a specimen load of 5 kN. The area the photographs are obtained from is not the same as the previous set of figures, but they are adjacent to them. Because no precautions to limit hydrogen cracking had been taken, it was expected that the phenomenon would be very pronounced in this specimen. From hydrogen embrittlement, the cracks were expected to become evident at relatively low levels of stress. Small increments of stress were used in obtaining replicas of this specimen.

Figure 57 shows the weld and HAZ baseplate. The crack-like structure near the top of the photograph is probably either cracks in a brittle oxide layer, or possibly a grain boundary. The baseplate adjacent to the weld appears very rough and may be covered with an oxide film. The round, smooth patches of the photograph are bubbles of the replica itself. These are areas where air was inadvertently trapped during the replication process. Note the texture of the surface: it is quite rough close to the weld and gradually smooths as distance is increased. No cracks or related phenomena are observed. The horizontal gash at the top of Figure 59 is the result of mechanically removing slag from the weld.

Figures 60 and 61 are a composite photomicrograph of the weld and adjacent baseplate of HY-130 loaded to 40 kN.

The weld metal in Figure 60 takes up the upper half of the photograph. The crack-like features observed in the weld metal may be oxide cracks, or artifacts from solidification. These structures have been observed in the weld metal at all levels of applied load. The crenelated surface of the baseplate adjacent to the weld is most likely an oxide layer. The small crack-like features distributed over these surfaces presumably are not indicative of a problem with the baseplate.

Figure 61 shows the condition of the baseplate from 118 μm to 152 μm from the weld. The bubbly surface that takes up much of the left side of the photograph is probably a

slag deposit. The right side is relatively clean baseplate. At the top, center of Figure 61, a microcrack may have formed. It is unclear what the series of small, lateral, crack-like features is in the upper part of this photograph. They do not appear to be full cracks.

Figures 62, 63, and 64 form a composite photomicrograph of HY-130 loaded to 50 kN. The features observed in these figures are very similar to those discussed in the previous set of photographs.

The weld area of Figure 61 appears to be covered with a layer of oxide which has cracked from the stress. There are a series of small crack-like structures bordering the edge of one of the oxide areas. These are located near the middle of the photograph. These features may be due to yielding of the material. No cracks appear in the baseplate. The lower right of the photograph appears to be slag.

There appears to be an area of general yielding near the top of Figure 63 from the apparently elongated surface features observed in a section of the photograph. It is doubtful that this really is plastic deformation. In comparing the elongated structures to the surrounding baseplate, strains on the order of 100% would have had to occur. Such a localized patch of plastic deformation is not possible from a continuum mechanics viewpoint. It violates the boundary conditions. Therefore, it is likely that this feature is an anomaly of the replica. This may have formed by prematurely removing the replica from the specimen surface while the solvent was still present to a large degree and the

cellulose acetate was soft and pliable. The surface features appear elongated in the direction of the maximum tensile stress. The lower portion of Figure 63 and the upper portion of Figure 64 are a bad spot in the replica. No information can be found there.

Figure 64 shows the baseplate at greater distances from the weld. As seen in other replicas, the textured surface is abating. No cracks or other serious anomalies are observed.

Figure 65 shows the HY-130 weld metal in the absence of externally applied loads. As discussed earlier, this is a good example of Widmanstätten structures which are formed through the solidification process. It is important to note, however, that Widmanstätten structures do not generally cross one another as some of the features of this specimen do.

Figures 66a and 66b are photomicrographs of HY-130 weld metal taken with the 40x objective lens. Here, the specimen has a 5kN load applied to it.

Note the similarity of the structure in Figure 66a to that of Figure 53. There are sections where there is a raised ridge (corresponding to a depression in the real surface) surrounding a section of weld metal that is close to being at the same level as the surrounding surface. The raised-ridge structure is very similar in both photomicrographs. Although this structure was not observed at the zero load state, the fact that it is present at this low load level indicates that it may be indigenous to the weld metal of HY steels.

The implications of the presence of this structure are unknown. This would be an area for further study.

Figure 66b appears to have some crack-like structures that may be weld cracks or may be oxide cracks.

Figures 67a and 67b show HY-130 weld metal with a 40 kN load applied to the specimen. Figure 67a was taken using the 20x objective lens; Figure 67b is of the same area and was obtained with the 40x objective lens. Figure 67a shows how the Widmanstätten structures tend to congregate into patches. Figure 67b illustrates the increased level of detail at higher magnification.

Figures 68a and 68b are also of HY-130 weld metal at a 40 kN load, corresponding to a strain of 0.010. These are included to illustrate the variation of weld metal surface texture. No indications of yield or failure are noted.

Another odd formation is observed in Figure 69. Here, HY-130 weld metal at a 40 kN load level was observed using the 100x objective lens. This formation appears to be a series of cracks in a fish scale pattern. It may be disrupted oxide, rather than real cracks in the weld metal. This pattern of cracks appears to be quite regular.

Figures 70a and 70b show HY-130 weld metal with a specimen load of 50 kN, corresponding to a strain of 0.017. Like Figures 67a and 67b, the 20x and 40x objective lenses were used. Some small cracks appear to have formed in examining Figure 67b.

4.5 Discussion of Technique

One of the disappointments in performing the observations using the laser microscope was that there was a lack of statistically significant findings. Cracking was not as plentiful as had been initially expected. Because of this, quantitative distributions of microcrack size, location, orientation, and other parameters could not be constructed. In examining the replicas using the laser microscope, it was observed that cracks were much less prevalent in the mild steel weldments than any of the HY steels. There were also less cracks and other problems found in HSLA-100 than in either of the HY steels. Again, a statistically significant sample could not be obtained.

It was hoped that cracks could be traced back to specific features or types of features through the use of replicas at various load levels. This premise hinges on the ability to find a large number of cracks at elevated load levels, and taking enough replicas over the region where the crack exists to be able to trace it back to its origin. An example of this was seen when discussing the "thread-like objects of Figure 40a. Because cracks were not as plentiful as hoped, this was not possible.

Naturally, to do this, one must be able to clearly identify a structure as a crack, and not some other anomaly. Such skills come with experience. In practice, for applications to industry, a significant amount of training is necessary in order to have inspection personnel using the equipment effectively.

Significant problems come from using the replica technique on a weldment or on any other surface that has abrupt changes in slope. The operator must practice his or her replicating technique in order to ensure that the replicas will be accurate and complete. It is a real challenge not to get air bubbles in the region where the weld metal meets the baseplate. The same comments hold true for replicating the top of a weld surface.

A related problem arises when one attempts to examine such a convoluted replica beneath any microscope, laser or otherwise. The problem is that the replica is so highly contoured, regions of it will be at high angles and reflectivity will be poor, and/or distortion will be high. To some degree, this problem can be overcome by tilting the slide-mounted replica underneath the objective lens. Because the field of view is so small, this becomes impractical and hinders microscopic studies tremendously.

The laser microscope has a great deal of potential as an inspection tool. At present, the instrument is intended for use as a laboratory instrument and is not compact nor hardy enough to use in an industrial environment, much less using it shipboard.

The rigors of the industrial environment necessitate the equipment be made stronger and less delicate. The components must be made shock-hardy and condensed into a smaller package or packages. Ideally, the compact, industrial version would consist of one or two components, be light enough to be transported by one person, and be flexible enough for multiple applications.

The industrial environment is dusty and dirty, problems that can be addressed with small filter units and cabinets with tight seams. Shipboard, the temperature and humidity can vary from very dry, freezing conditions to hot, damp conditions, and any combination in between. The equipment at present can sustain temperatures between 5°C and 40°C, and relative humidity of 80% or less. (Appendix B) The range of operating environments must be expanded, particularly for high humidity.

Record keeping is important in any inspection scheme. There are several methods available for making records that will last significant amounts of time.

The video tape is an easy recording medium. When stored under ideal conditions, a good quality video tape will last in excess of 10 years. The problem is that it is difficult to review the information and a map must be established for each tape to identify what each image is. An alternative method would be to create the capability to type in identifying information using a keyboard and the laser microscope itself.

Photographs offer a convenient medium for storing and maintaining records of inspections. They are easily compared and filed. Photographs last on the order of many decades.

Replicas, themselves, can act as the recording medium, storing much more information than photographs or video tape. They are, after all, a faithful reproduction of the actual surface being studied. The longevity of replicas is not known, although it is speculated to be on the order of decades.

CHAPTER 5

Conclusions

The traditional way to apply microscopy to welding is to section a weld, polish and etch it, then study the cross section. The problem with this approach is that it is a destructive test which many times can alter or destroy some of the very features one is examining for. Relatively little attention has been given to applying microscopes in situ for inspections of welds. The confocal scanning He-Ne laser microscope has great potential in this area. Principally through the virtue of its capability to process images and construct extended focus pictures, visualization and measurement of irregular surfaces is easy. Findings may be recorded in a number of different formats for later study or for archival storage.

A great deal of information exists regarding conventional microscopy as applied to metallurgy and welding. The confocal scanning laser microscope is a tool to broaden this body of knowledge with significant potential applications to industry.

The capability of the laser microscope as a tool to study weldment surfaces is demonstrated. Cracks and other surface features as small as 0.25 μm in width can be routinely observed. Composite photomicrographs may be assembled, permitting study and

recording of relatively large areas at high resolution. Through the combination of replication and laser microscope visualization, metallurgical phenomena such as crack initiation and propagation can be followed. The technique of assembling composite photographs allows study of features too large for single-screen viewing.

No definitive features were found to indicate possible trouble-spots within a weldment, but a small number of samples and limited time precluded further study. However, in-situ visualization of welds may result in relatively accurate service life predictions, based on experienced gamered through such experiments as those discussed herein.

The work presented on this thesis represents just a start into applying the laser microscope to the study of high strength steel weldments. While hard, quantitative data was not obtained for relating the growth of microcracks to the embrittled HAZ and welds, a great deal of qualitative information was gathered. Baseplate and weld cracks were observed to form and grow under monotonic loading. The baseplate cracks were observed only in mild steel. Crack-like features were also observed in oxide layers lying atop weld metal. There was surprisingly little evidence of formation of new cracks in the HAZ or in the weld metal under strains that went well into the plastic regime. This was especially surprising for HY-130 which should have had a great deal of hydrogen cracking. Results indicate that HSLA steels do have a significant advantage over HY steels in their resistance to cracking at comparable strength levels. This directly translates into a lower production cost per ton of steel. It is therefore warranted to fully address the potential

uses of HSLA steels as a replacement for the HY steels currently being used in naval shipbuilding.

CHAPTER 6

Future Work

The following topics represents are possible follow-on work to this thesis:

HSLA steels: Investigate the feasibility of replacing HY-steels with HSLA-steels, weighing fabrication methods, shock criterion, cost, and other parameters important to naval shipbuilding.

Microcrack formation and growth: This study can be expanded to include a statistically significant population of specimens and different welding techniques. The investigation can include the effects of undermatching / overmatching and its applicability to high strength steel weldments. In addition, critical crack length effects can be studied.

Investigation of methods to reduce residual stresses in weldments. Different welding techniques and emerging technologies can be investigated. In this way, such new processes as ultrasonic and laser welding can be studied.

Stress corrosion cracking: Through the use of the VCR, timed recordings can be made of crack initiation and propagation of specimens as they are partially immersed in a hydrogen permeating environment.

Stereo visualization: The relatively small size of a replica mounted on a glass slide lends itself to be handled and positioned. A tilting mount can be devised to obtain stereo photomicrographs of different phenomena whose likeness is preserved on a replica. Further, positive casts can be made from the negative replicas and the shape of actual surfaces can then be reproduced and observed.

Table 1

Crack Characteristics

Formation Characteristic	Hot Crack	Cold Crack	
		Short Time	Delayed
Temperature	near bulk solidus temp	< 204 °C	
Time delay	immediate upon weld solidification	during cooling to ambient	days to months
Propagation	intergranular	transgranular	transgranular
Location	weld metal, HAZ	weld metal, HAZ	
Principal Cause	low Tm grain boundaries	hydrogen embrittlement	

Table 2

Hot Crack Classification

	Mechanistic Classification	Location Characteristics
High Temperature Cracking	Type 1 Segregation Cracking	Type 1A Solidification Cracking in 1° Weld Metal
		Type 1B Liquation Cracking in HAZ
		Type 1C Liquation Cracking in 2° Weld Metal (multipass)
	Type 2 Ductility-Dip Cracking	Type 2A Ductility-Dip Cracking in HAZ
		Type 2B Ductility-Dip Cracking in 1° Weld Metal
		Type 2C Ductility-Dip Cracking in 2° Weld Metal (multipass)

Table 3

An Alternative Hot Crack Classification Scheme

	Mechanistic Classification	Location Characteristics
High Temperature Cracking	Type I Segregation Cracking	Type I-A Solidification Cracking in 1° Weld Metal
		Type I-B Liquation Cracking in HAZ
		Type I-C Liquation Cracking in 2° Weld Metal (multipass)
	Type II Ductility-Dip Cracking	Type II-A Ductility-Dip Cracking in 1° Weld Metal
		Type II-B Ductility-Dip Cracking in HAZ
		Type II-C Ductility-Dip Cracking in 2° Weld Metal (multipass)

Table 4

Relative Hot Cracking Potency Factors of Elements in Fe-Binary Systems (Clark, 1962) (Masubuchi, 1980)

Relative Ranking	Element	Weight Percent	Uses or General Effects
Worst	S	925.0	Impurity: causes hot cracking (FeS), reduces ductility, forms laminations, Notes: 1, 2, 4 (MnFeS, ZrS, MnS)
	B	917.0	Increases hardenability (< 0.001% B)
	C	322.0	Reduces notch toughness, Notes: 1, 2
	P	121.1	Impurity: reduces notch toughness, increases brittleness, Notes: 1, 2
	As	40.2	Inhibits graphitization.
	Cb	28.8	
	Mn	26.2	Deoxidizer, better notch toughness, combines with S, Notes: 1, 2, 3, 4
	Sn	16.8	
	Zr	15.2	Notes: 1, 2, 4 (ZrO), 5
	Ti	13.8	Notes: 1, 2, 3, 4 (Ti_xO_y), 5
	Ta	13.0	
	Sb	5.04	
	Cu	3.61	Precipitation hardening, Notes: 1, 2, 6
	Ni	2.93	Notes: 1, 2, 5
	Si	1.75	Deoxidizer, Notes: 1, 2, 4 ($Si0_2$-Mn_xO_y)
	Al	1.52	Deoxidizer (fine grain), Notes: 1, 2, 4 (Al_2O_3, etc), 5
Least	Co	0.3	Increases ability to cut hard, gritty, or scaly materials, reduces hardenability.

Table 4

Relative Hot Cracking Potency Factors of Elements in Fe-Binary Systems
(Clark, 1962) (Masubuchi, 1980)

Relative Ranking	Element	Weight Percent	Uses or General Effects

Notes:

1. Dissolves in ferrite, strengthens.
2. Dissolves in Austenite, increases hardenability.
3. Forms carbide
4. In non-metallic inclusions: deoxidizers and grain growth control.
5. Forms special intermediates (XX_xN_y, $XX_xN_yC_z$), increase hardness.
6. Increases machinability.

Table 5

Inagaki Limits on Steel Constituents for Hot Cracking

Element	Maximum Concentration (%)
C	0.15
Mn	0.80
Ni	1.0
S	0.035
Mn/S	35.0

Table 6

Material Composition and Properties
(data from Bass, 1989)

Element or Property	Mild Steel	HY-100	HY-130	HSLA-100
% Composition				
C	0.21	0.20	0.09	0.04
Cr	0.09 - 1.4	1.5	0.55	0.57
Cu	-	-	0.15	1.58
Mn	1.0	0.1 - 0.4	0.71	0.86
Mo	0.09 - 1.4	0.40	0.40	0.60
Ni	0.09 - 1.4	3.2	4.83	3.55
P	0.05	0.025	0.008	0.004
S	0.05	0.025	0.003	0.002
Si	0.09 - 1.4	0.25	0.28	0.27
Ti	0.09 - 1.4	-	0.005	-
V	0.09 - 1.4	-	0.08	-
Cb	-	-	-	0.032
Al	-	-	-	0.03
CE_{AWS}	38 - 42	52 - 57	47	
S_{HC}	6.7 - 5.0	8.4 - 5.9	1.9	
Material Properties				
Identifier	ABS Class B	USX TAG328	Lukens Steel Tag323	
σ_y (kpsi) Minimum	30	100	130	100
σ_y (kpsi) Actual	-	-	139	-
σ_{ult} (kpsi) Minimum	56	110	142	

Table 6

Material Composition and Properties
(data from Bass, 1989)

Element or Property	Mild Steel	HY-100	HY-130	HSLA-100
E (Mpsi)	29	29	29	29
ρ (lb/in^3)	0.29	0.30	0.30	0.30
Process	as rolled	Q&T	Q&T	

Table 7

Estimated Specimen Yield Loads

Material	P_y
Mild Steel	XXX
HY-100	XXX
HSLA-100	XXX
HY-130	XXX

Table 8
Specimen Distortion from Welding

Material	Yield Strength (kpsi)	Distortion over 40.6 cm (cm)	Radius of Curvature (cm)
Mild Steel	30	0.279	740
HY-100	100	0.152	1358
HSLA-100	100	0.178	1160
HY-130	130	0.102	2024

Table 9

Specimen Characteristics

No.	Material	Length (cm)	Width (cm)	Thickness (cm)	Weld Bead Applied	Plain Plate
1	Mild Steel	40.6	6.4	1.24	X	
2	Mild Steel	40.6	6.4	1.24		X
3	HY-100	40.6	6.4	1.24	X	
4	HY-100	40.6	6.4	1.24		X
5	HSLA-100	40.6	6.4	1.24	X	
6	HSLA-100	40.6	6.4	1.24		X
7	HY-130	40.6	6.4	1.24	X	
8	HY-130	40.6	6.4	1.24		X

Table 10 Summary of Displacement-Load Curves		
Material	First Yield Load (kN)	Slope (kN/cm)
Mild Steel	8.5 - 9.7	66
HY-100	23 - 26	65
HSLA-100	20 - 23	64
HY-130	30 - 35	67

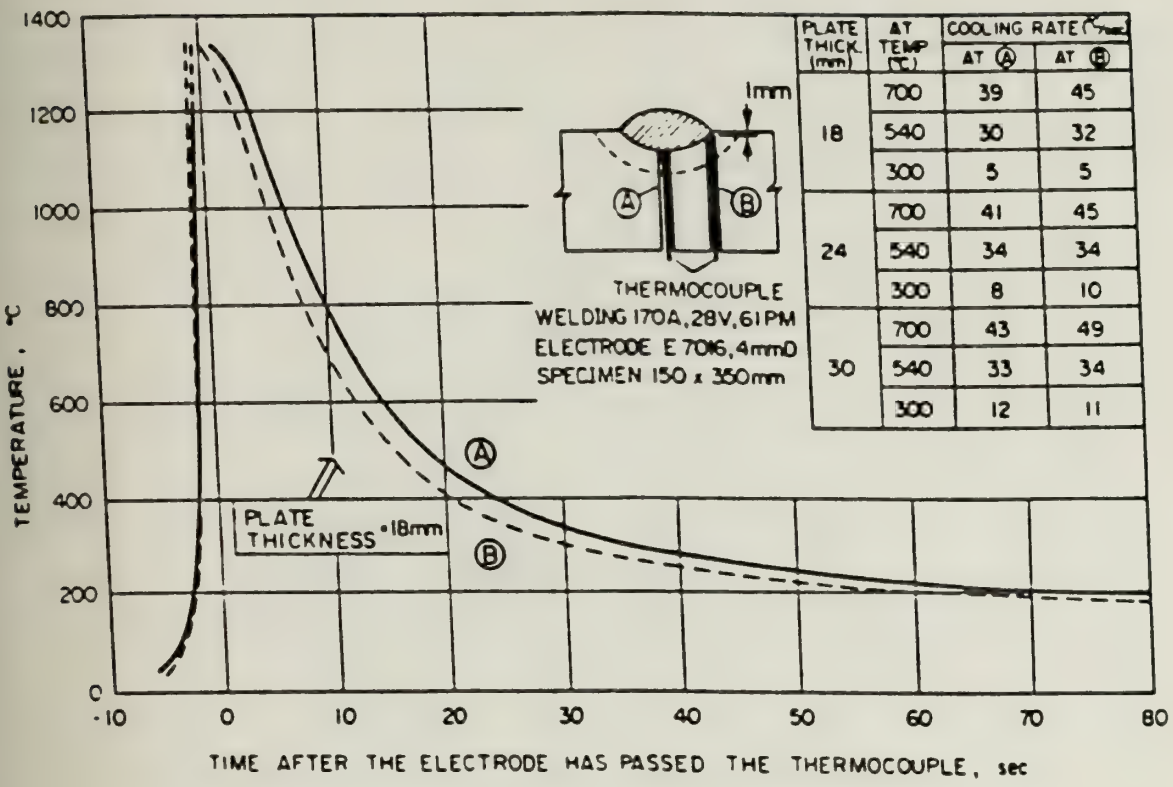

Figure 1: Thermal Cycle of a Weld

Thermal cycles are shown at two locations in the weldment. Position A lies beneath the weld. Position B lies near the surface, adjacent to the weld in the baseplate. In both cases, the high temperature in the HAZ causes metallurgical changes discussed in the text. (Masubuchi, 1980)

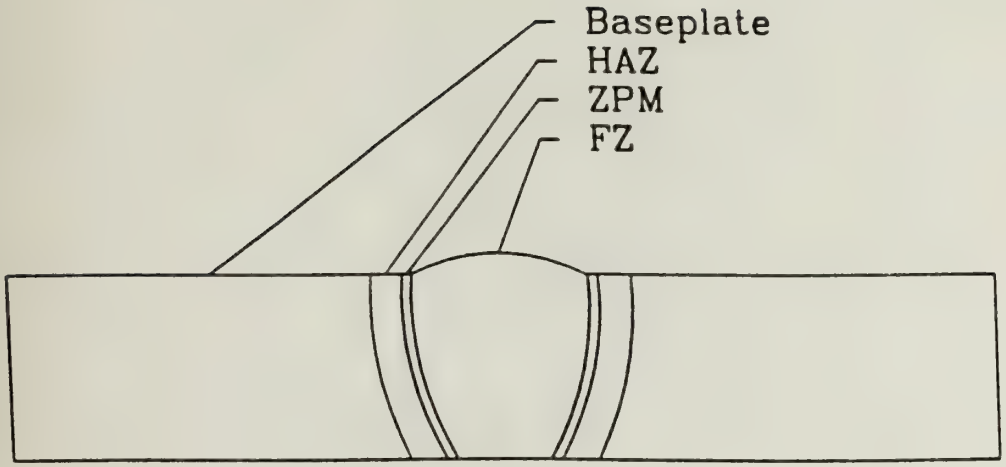

Figure 2: Anatomy of a Weld

The cross section of a butt weld is shown. The Fusion Zone (FZ), Zone of Partial Melting (ZPM), Heat Affected Zone (HAZ), and unaffected baseplate are indicated.

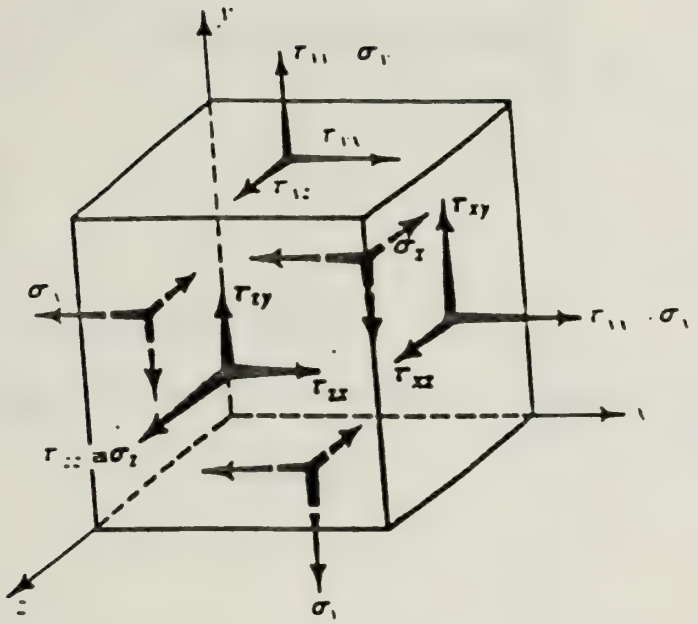

Figure 3: State of Stress

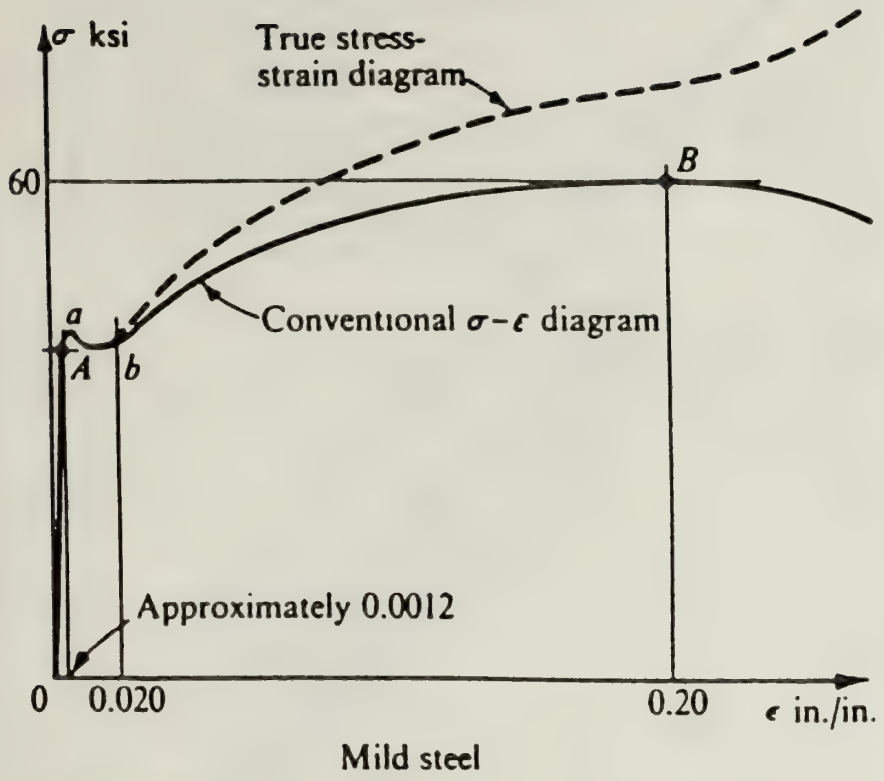

Figure 4: Stress-Strain Curve
A typical stress-strain curve

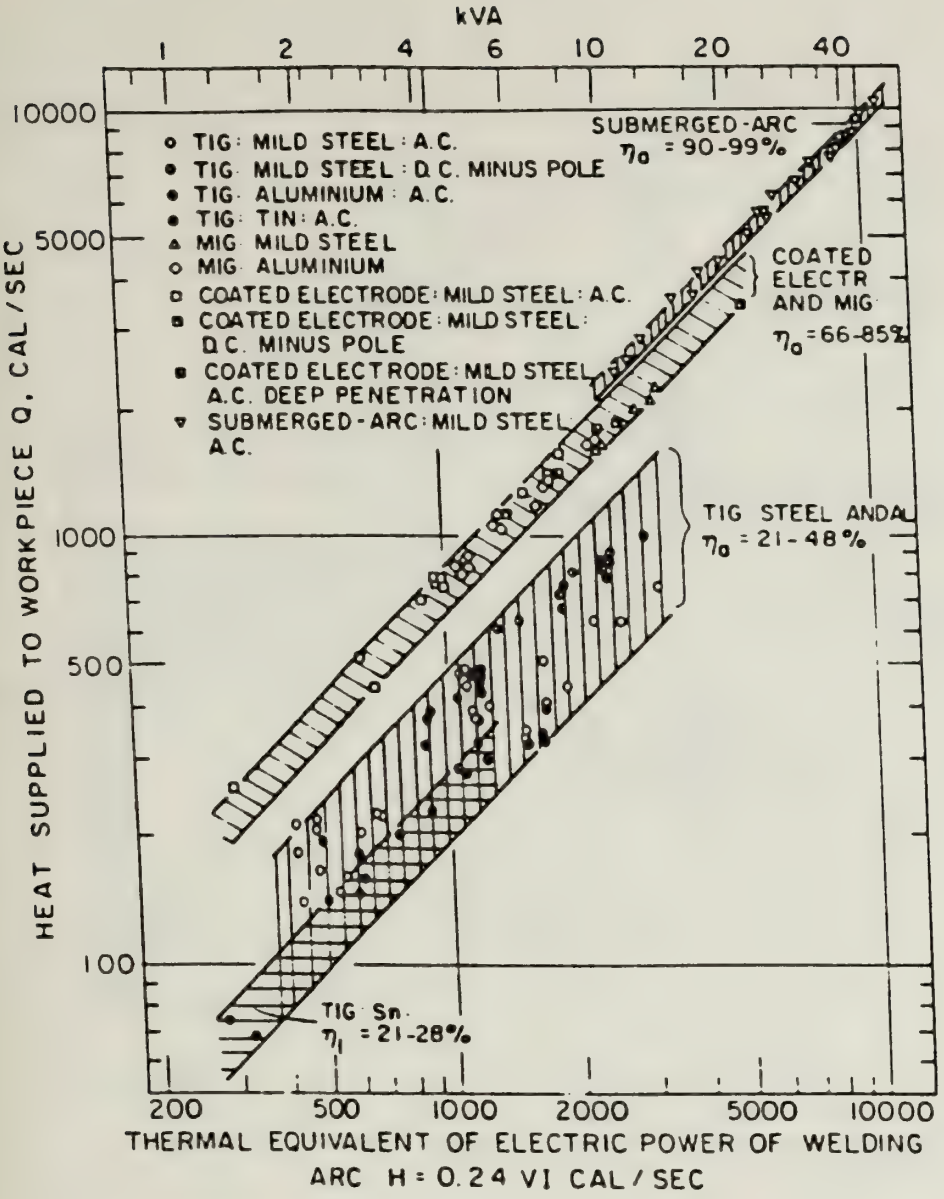

Figure 5: Arc Efficiency Values for Various Welding Processes and Materials (Masubuchi, 1980)

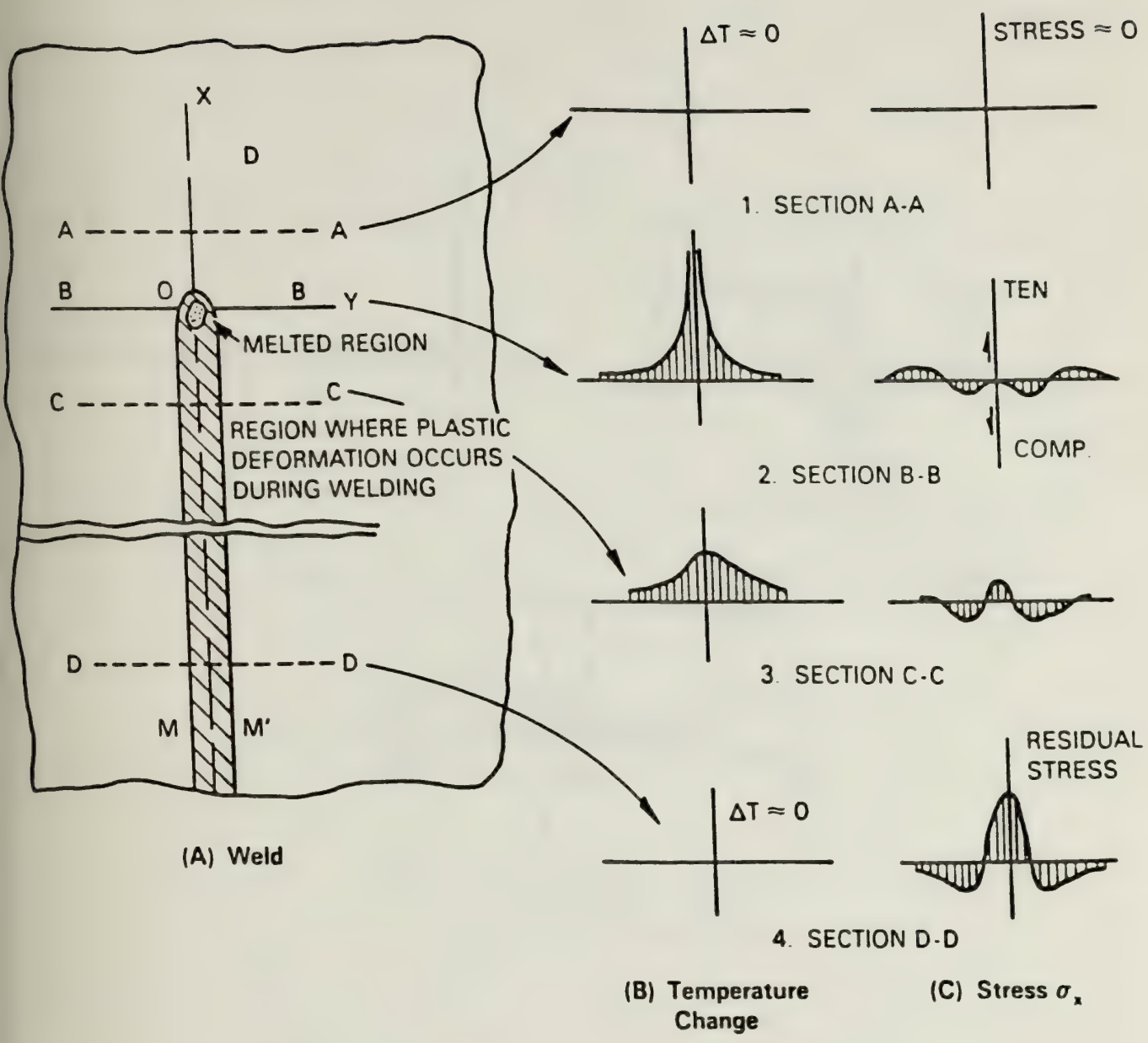

Figure 6: Temperature and Residual Stress Variation Along a Weld
(Masubuchi, 1980)

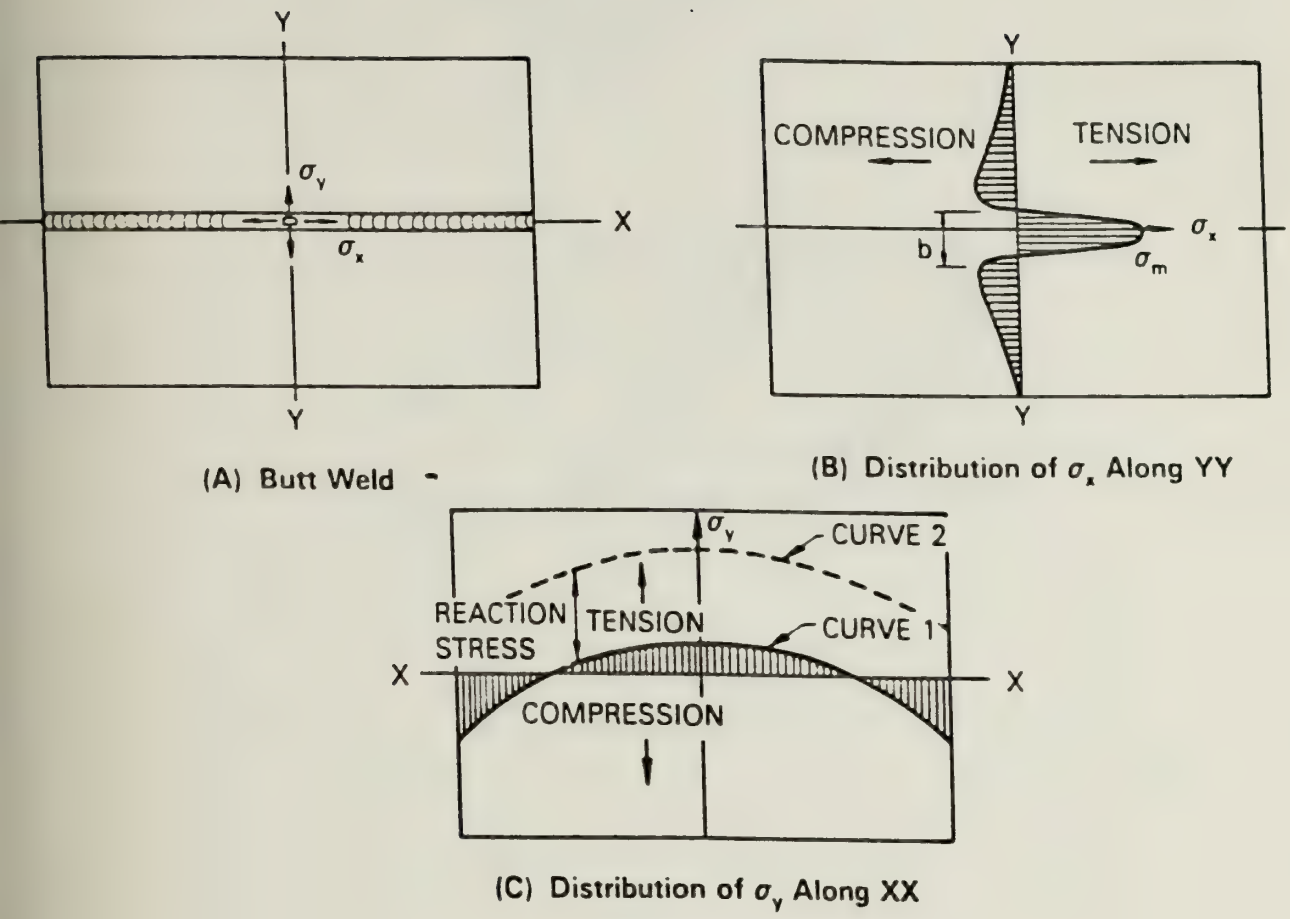

Figure 7: Residual Stresses in a Butt Weld

Longitudinal and transverse residual stress distributions for a bead-on-plate or butt weld are shown. (Masubuchi, 1980)

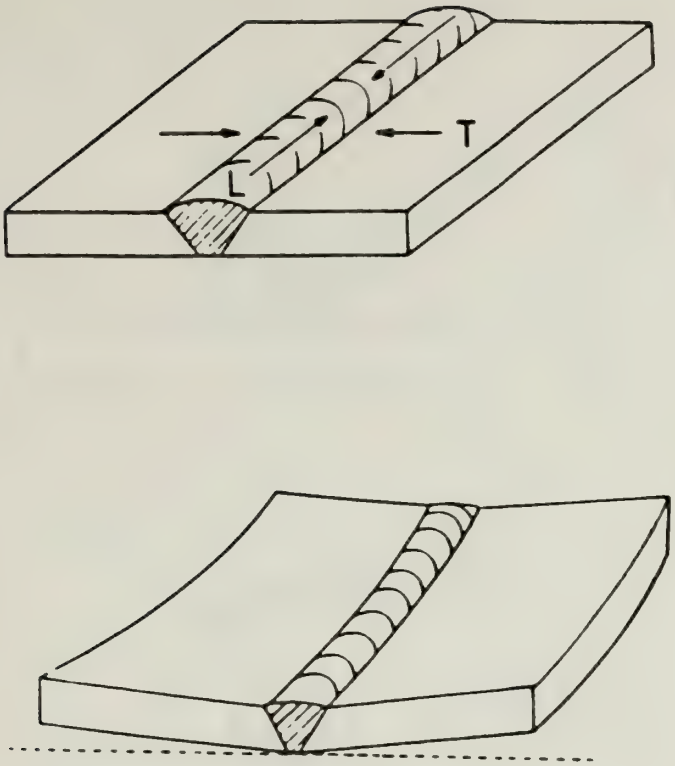

Figure 8: Major Tensile Stresses and Distortions in a Butt Weld
(Connor, 1987)

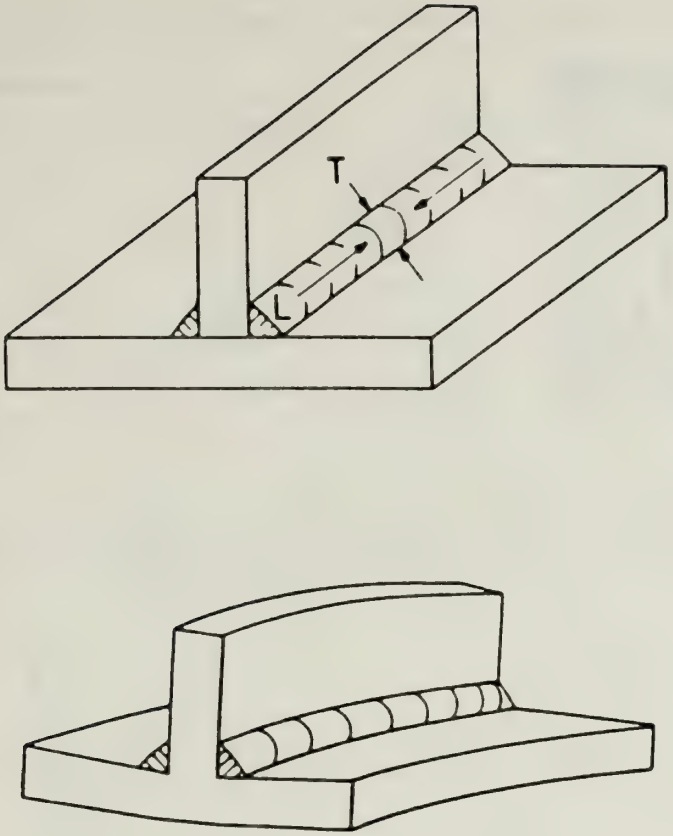

Figure 9: Major Tensile Stresses and Distortions in a T Joint
(Connor, 1987)

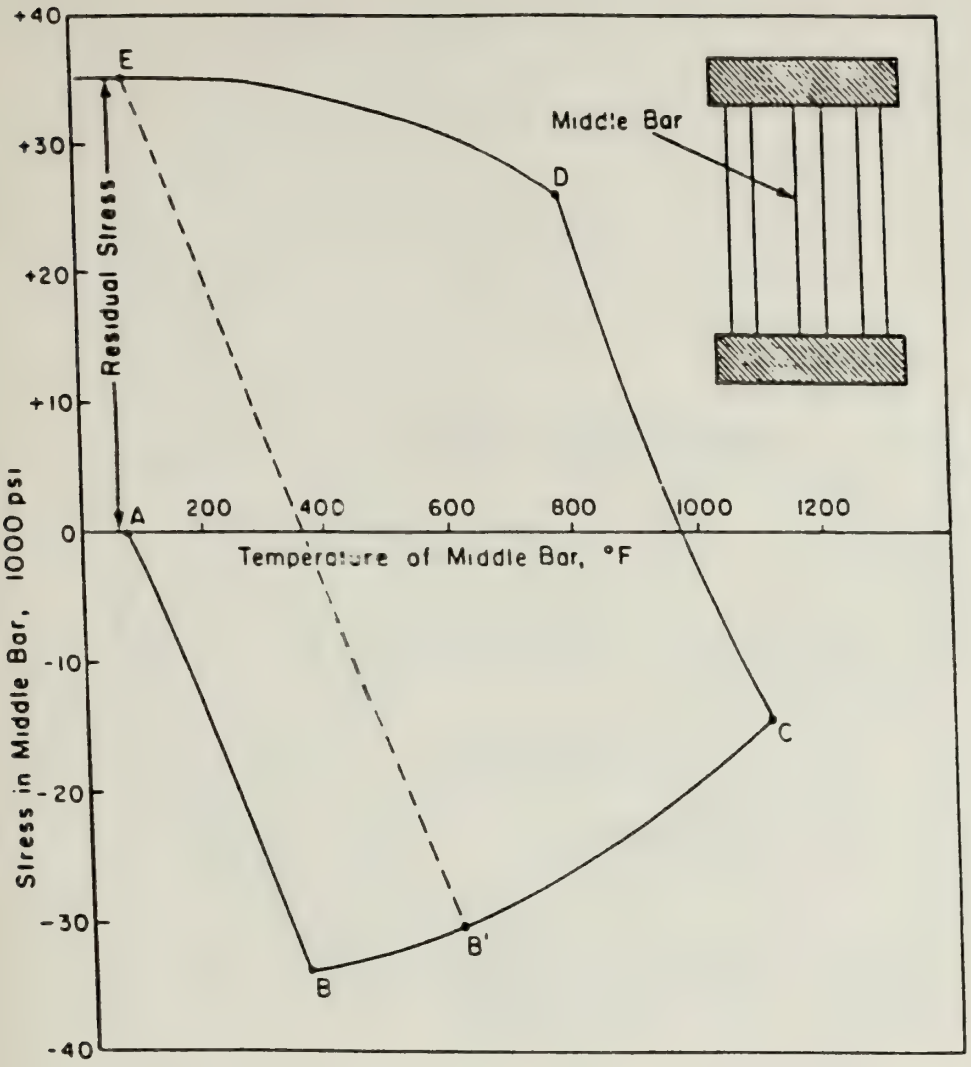

Figure 10: Discretized Model Illustrating Residual Stresses

A	Initial conditions.
A-B	The middle bar is heated. The side bars remain at ambient conditions throughout this procedure.
B	The middle bar reaches its yield strength.
B-C	The middle bar is in yield. The yield strength decreases as the temperature increases. Plastic deformation occurs in this region.
C	Maximum temperature is attained, begin the cooling process.
C-D	Cooling the middle bar, it first relaxes elastically, then passes into tension.
D	Compressive yield strength is reached.
D-E	The middle bar deforms plastically in tension.
E	At ambient conditions, showing the magnitude of the resulting residual stress in the bar.
B'	This is the condition that would have resulted in the same final residual stress state if simply cooled without any plastic deformation in the plastic regime.

(Masubuchi, 1980)

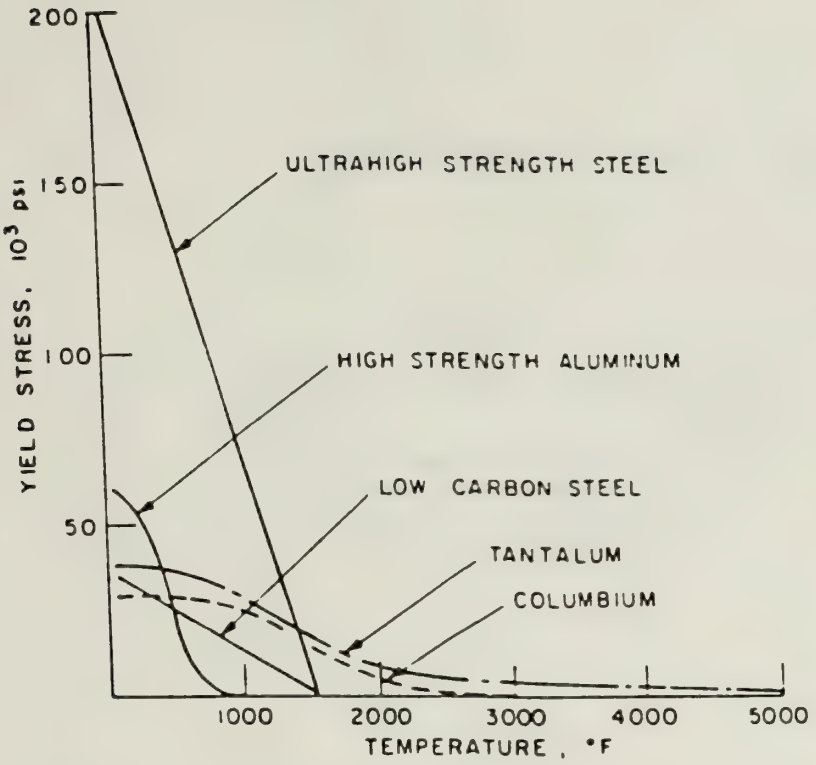

Figure 11: Temperature Variation of Yield Strength
(Masubuchi, 1980)

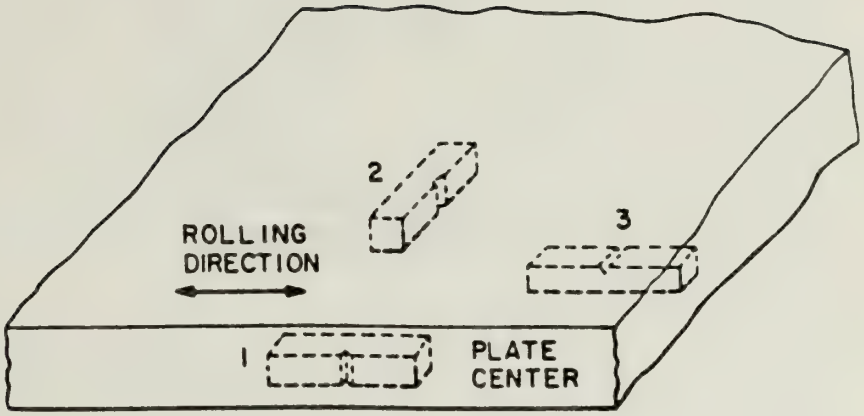

Figure 12: Charpy V-Notch Specimen Orientation in Plate
(Masubuchi, 1980)

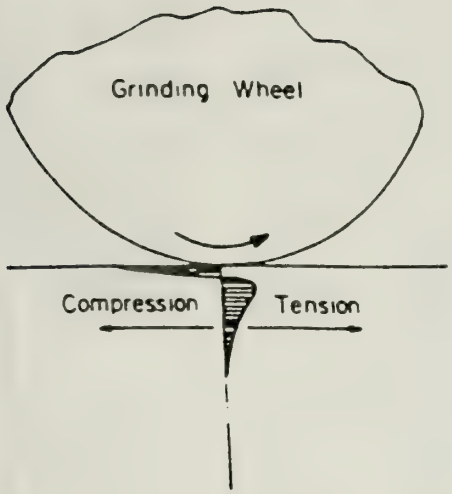

Figure 13: Grinding Induced Residual Stresses
(Masubuchi, 1980)

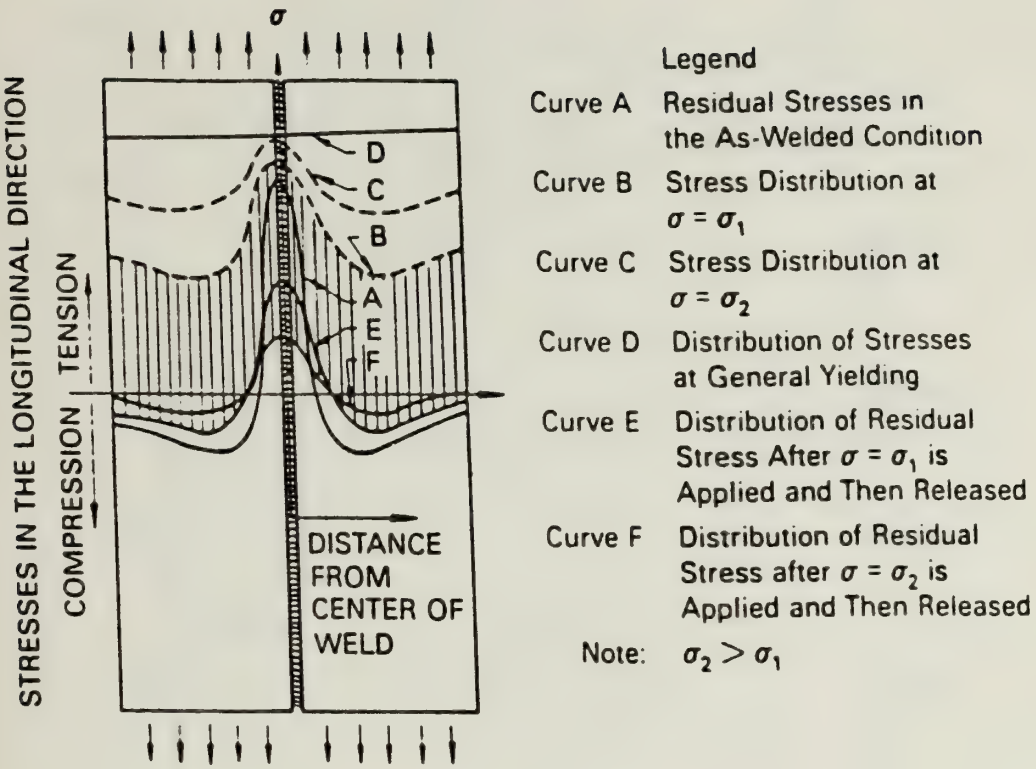
σ
STRESSES IN THE LONGITUDINAL DIRECTION
TENSION
COMPRESSION
D
C
B
A
E
F
DISTANCE FROM CENTER OF WELD
Legend
Curve A Residual Stresses in the As-Welded Condition
Curve B Stress Distribution at σ = σ1
Curve C Stress Distribution at σ = σ2
Curve D Distribution of Stresses at General Yielding
Curve E Distribution of Residual Stress After σ = σ1 is Applied and Then Released
Curve F Distribution of Residual Stress after σ = σ2 is Applied and Then Released
Note: σ2 > σ1

Figure 14: Effect of Tension on Residual Stresses
(Connor, 1987)

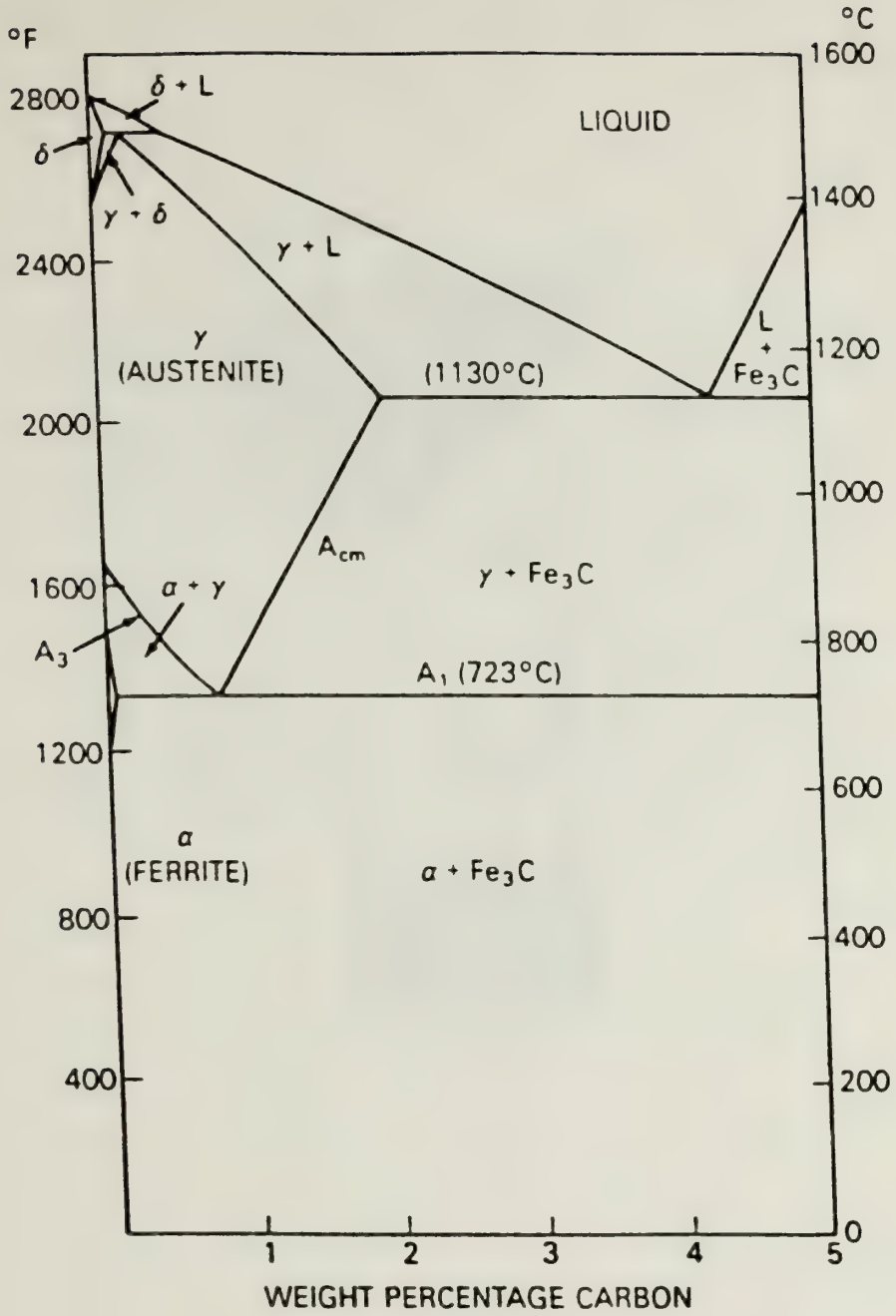

Figure 15: Fe-C Phase Diagram
(Connor, 1987)

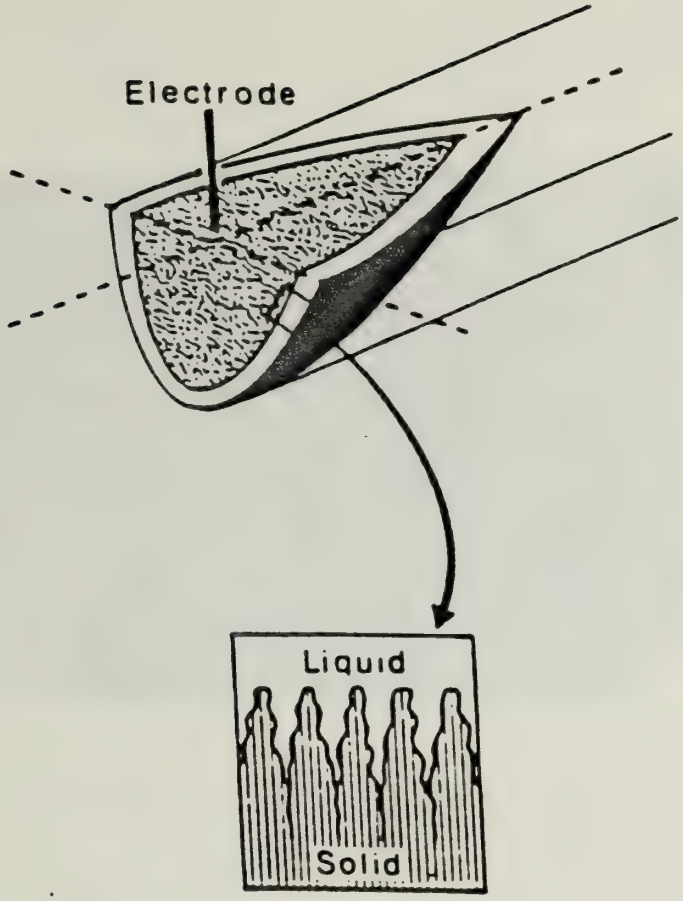

Figure 16: Quasi-Equilibrium Solidifying Weld Pool
(Dixon, 1981)

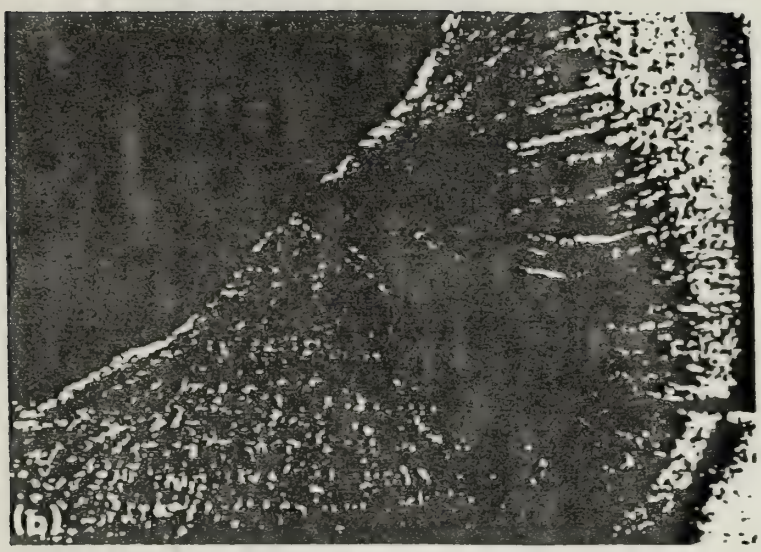

Figure 17: Fillet Weld Cross Section
Note the grain pattern and the crack that has developed due to segregation effects.
(Masubuchi, 1980)

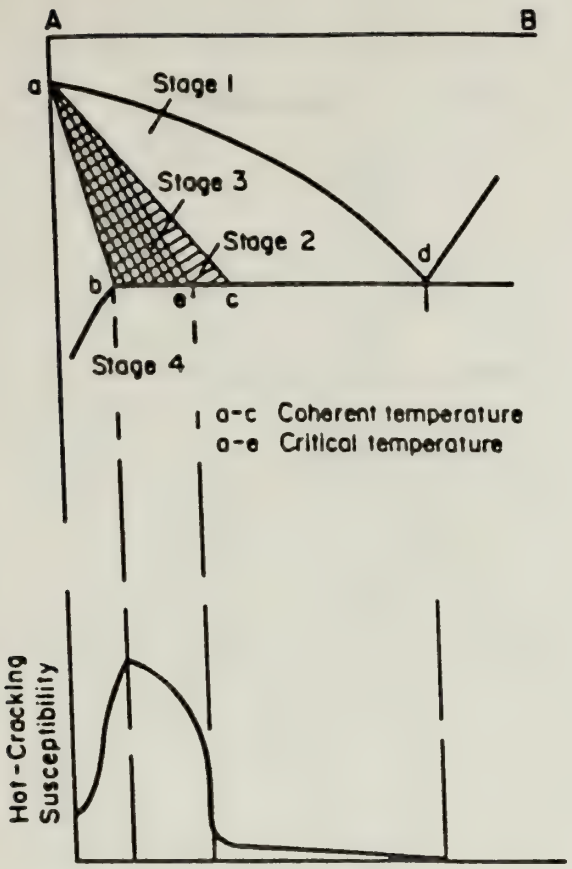

Stage 1 - Dendrites freely dispersed in liquid. No cracking.
Stage 2 - Interlocking of grains. "Liquid healing" possible if cracks form. "Accommodation" not important.
Stage 3 - Critical solidification range. No "healing" of cracks possible if "accommodation" strain exceeded
Stage 4 - Solidification. No cracking.

Figure 18: The Effects of Constitutional Features on Cracking Susceptibility in Binary Systems
(Masubuchi, 1980)

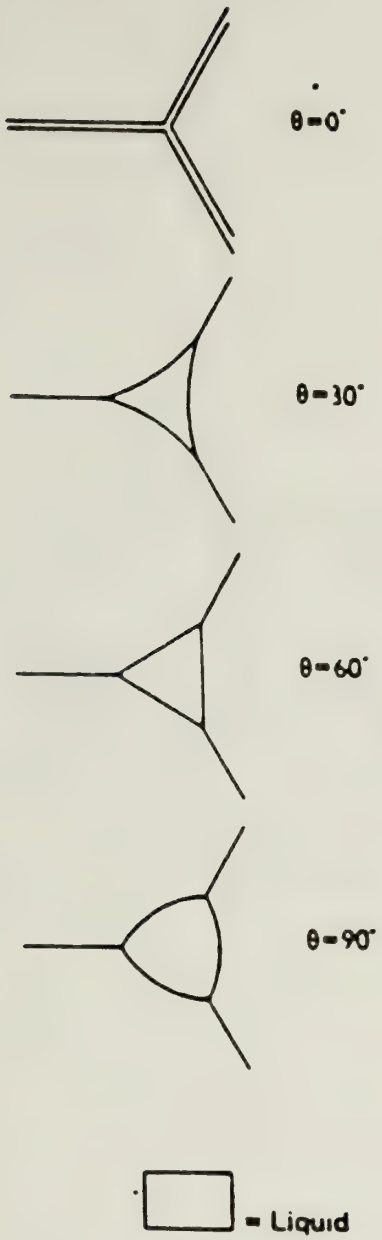

Figure 19: Liquid Phase Distributions
(Dixon, 1981)

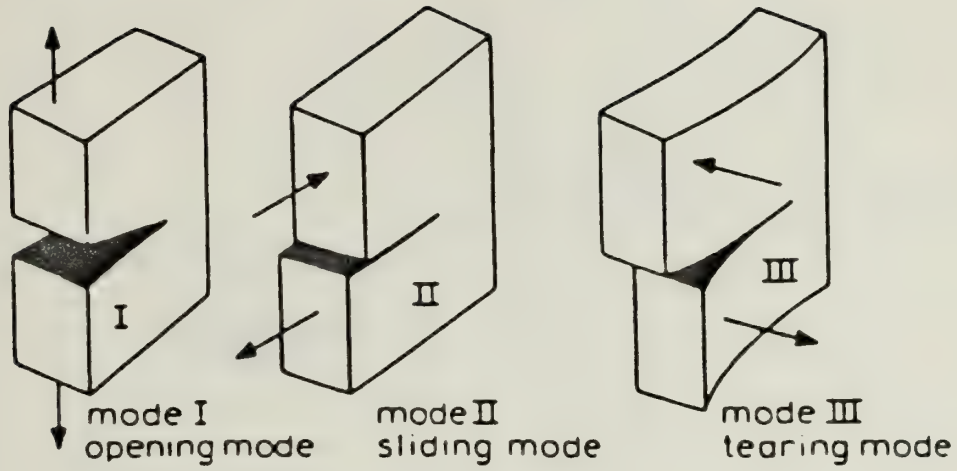

Figure 20: Cracking Modes
(Masubuchi, 1980)

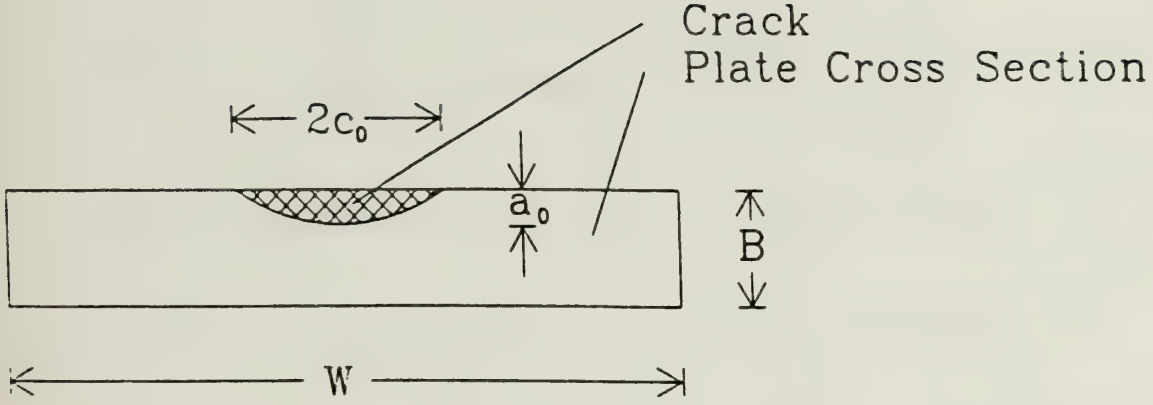

Figure 21: Surface Crack in Plate

The surface crack in a plate is shown in cross section. This has some similarities to the experiment conducted in this study.

(Masubuchi, 1980)

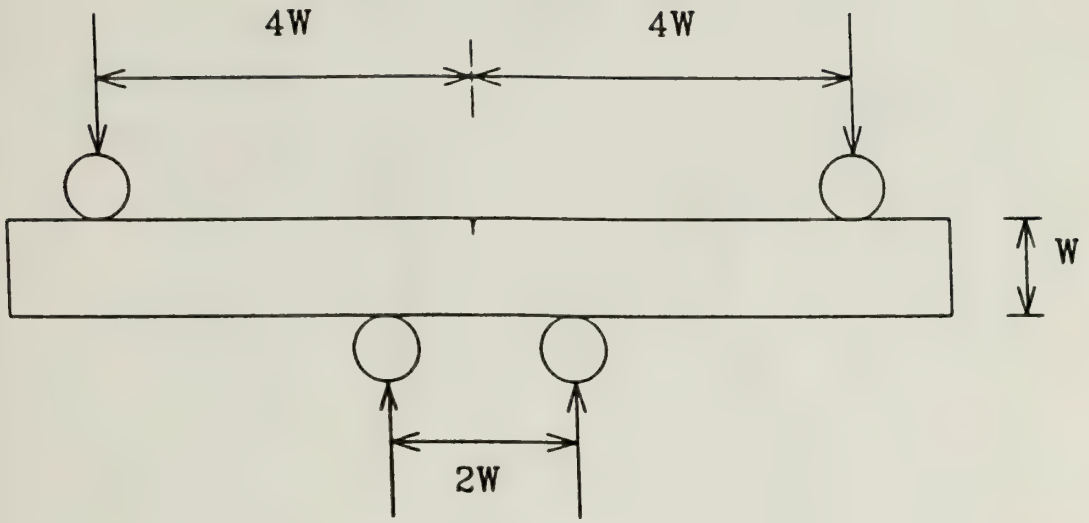

Figure 22: 4-Point Bend Test to Determine K_{Ic}
(Masubuchi, 1980)

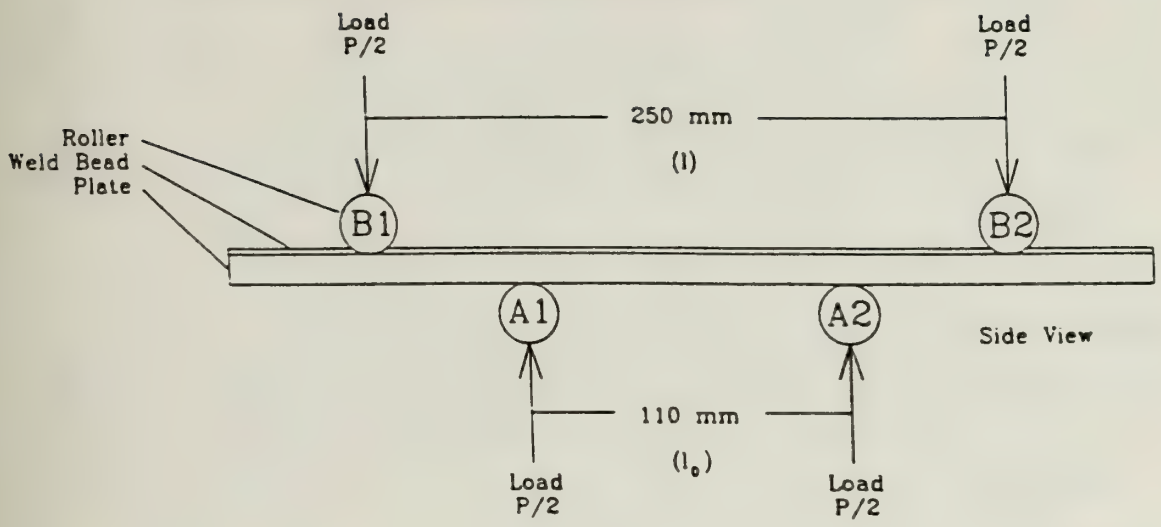

Figure 23: 4-Point Bend Test Apparatus Setup

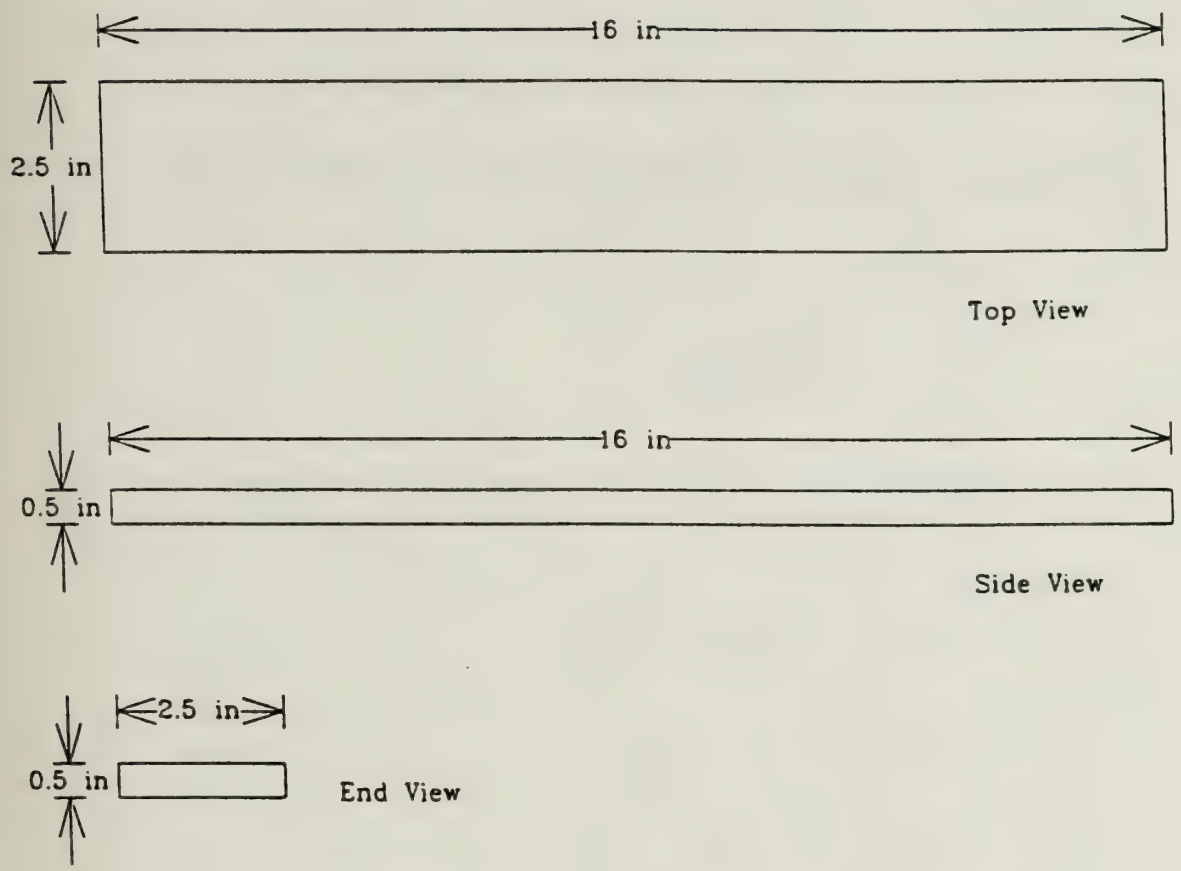

Figure 24: 4-Point Bend Test Specimen

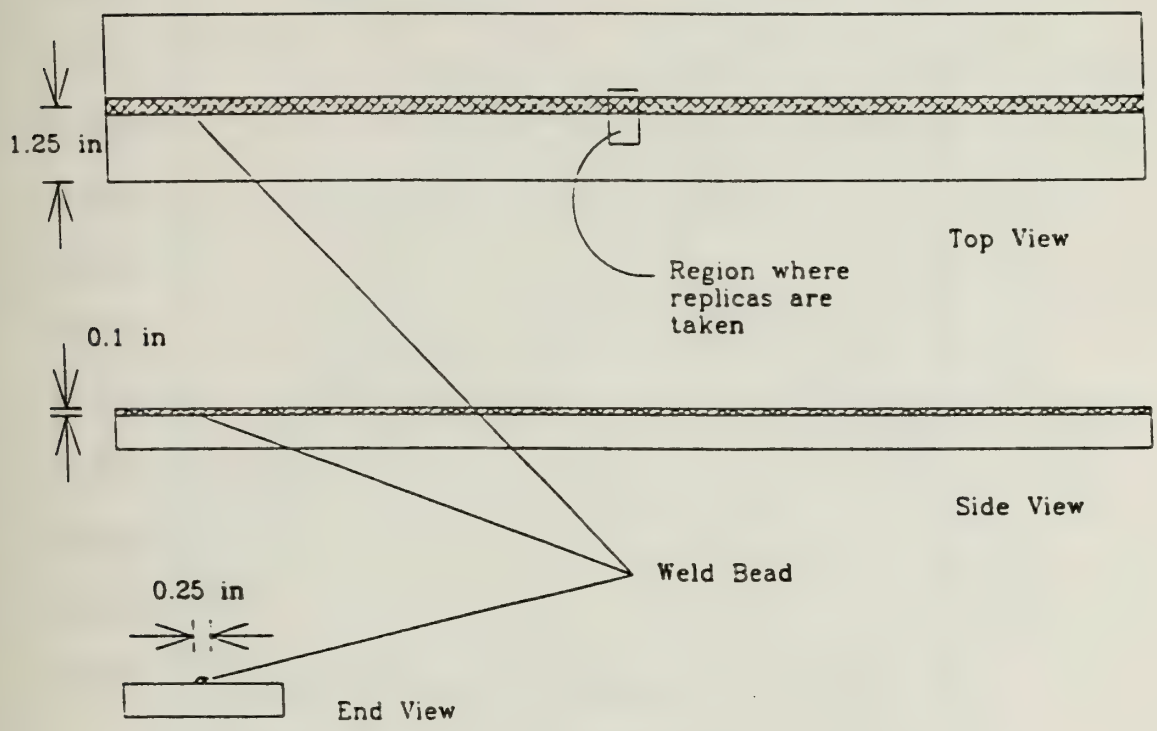

Figure 25: Bead-On-Plate Specimen

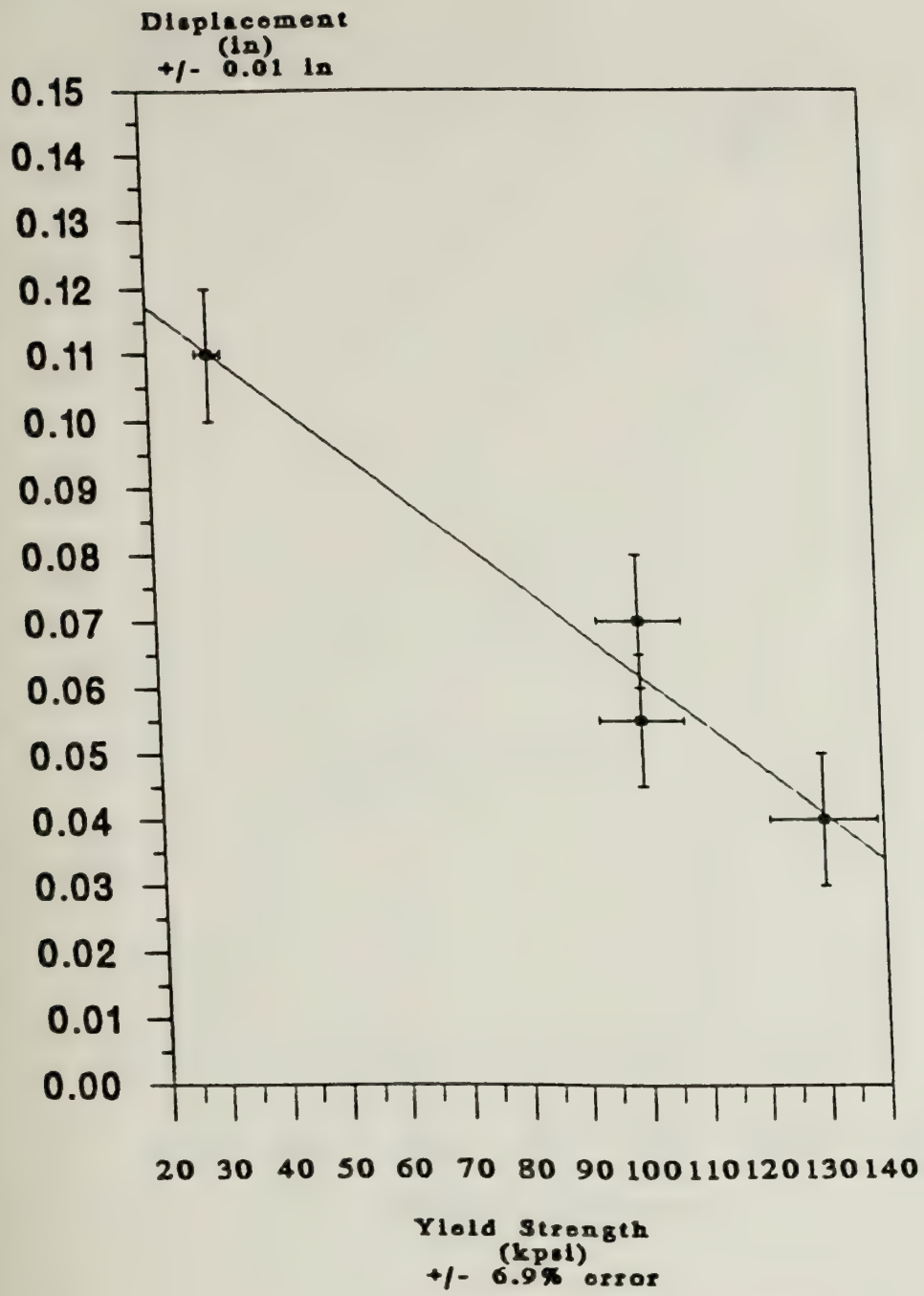

Figure 26: Initial Distortion from Welding with E7014

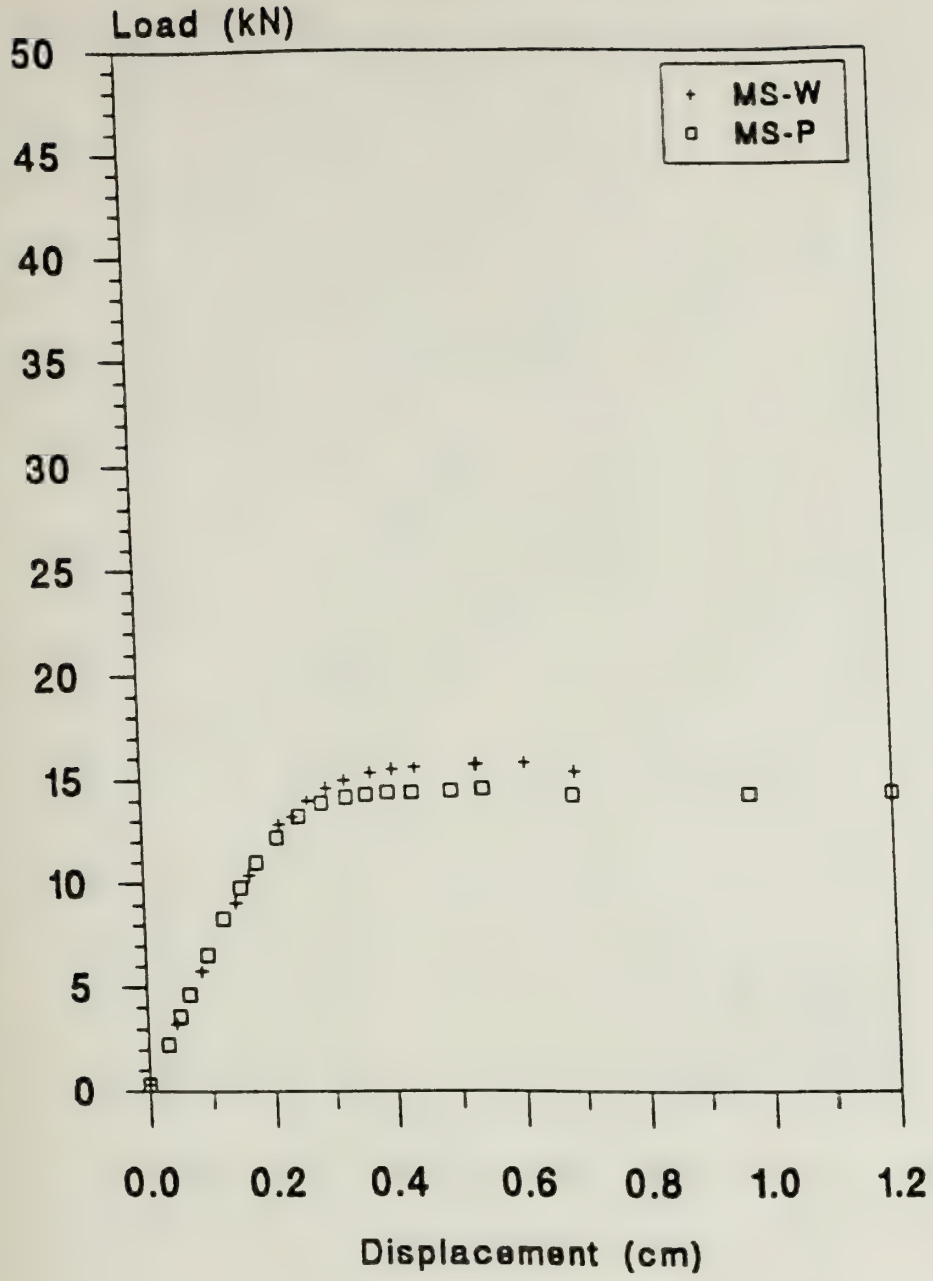

Figure 27: Mild Steel Displacement-Load Curve

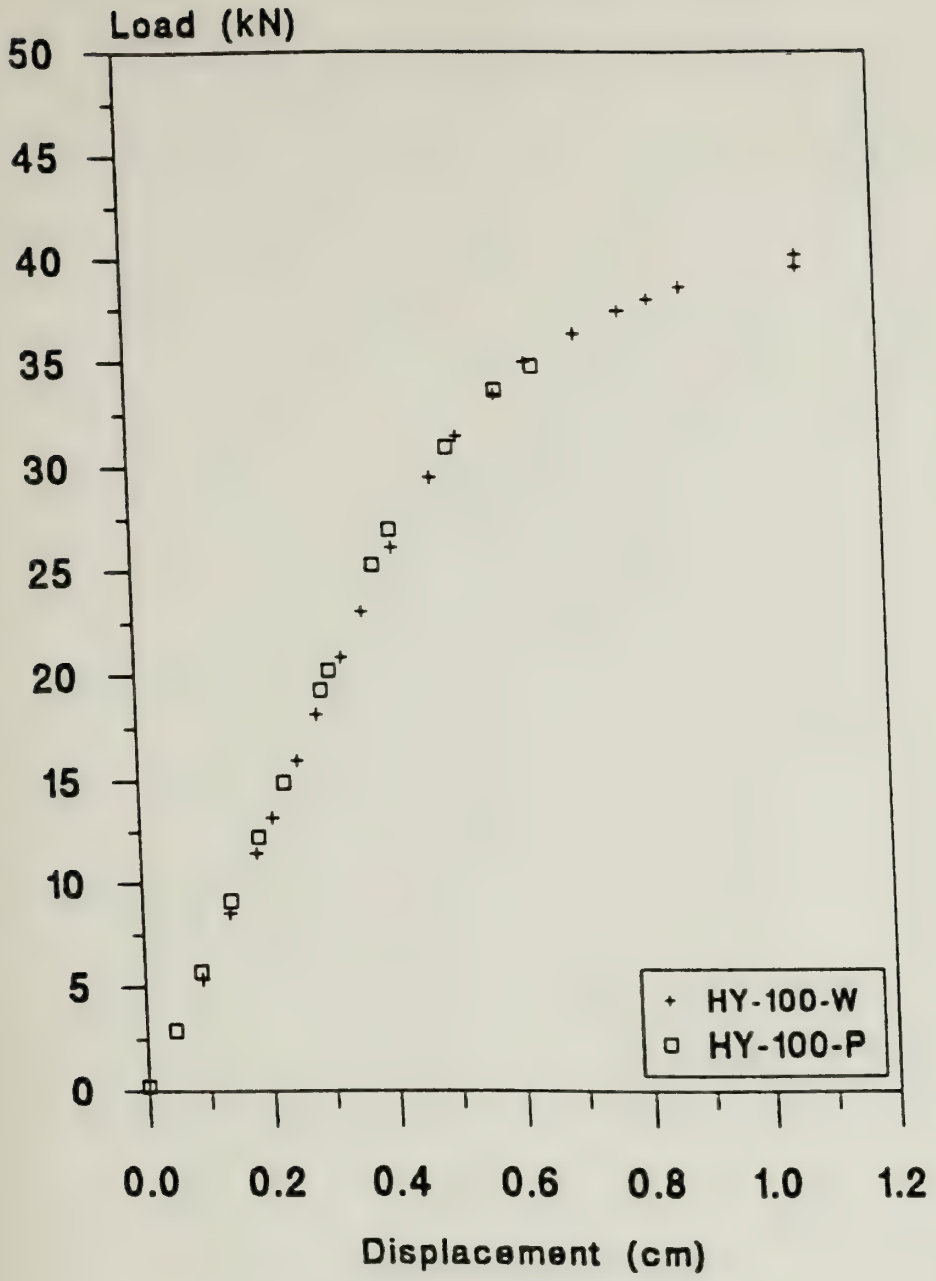

Figure 28: HY-100 Displacement-Load Curve

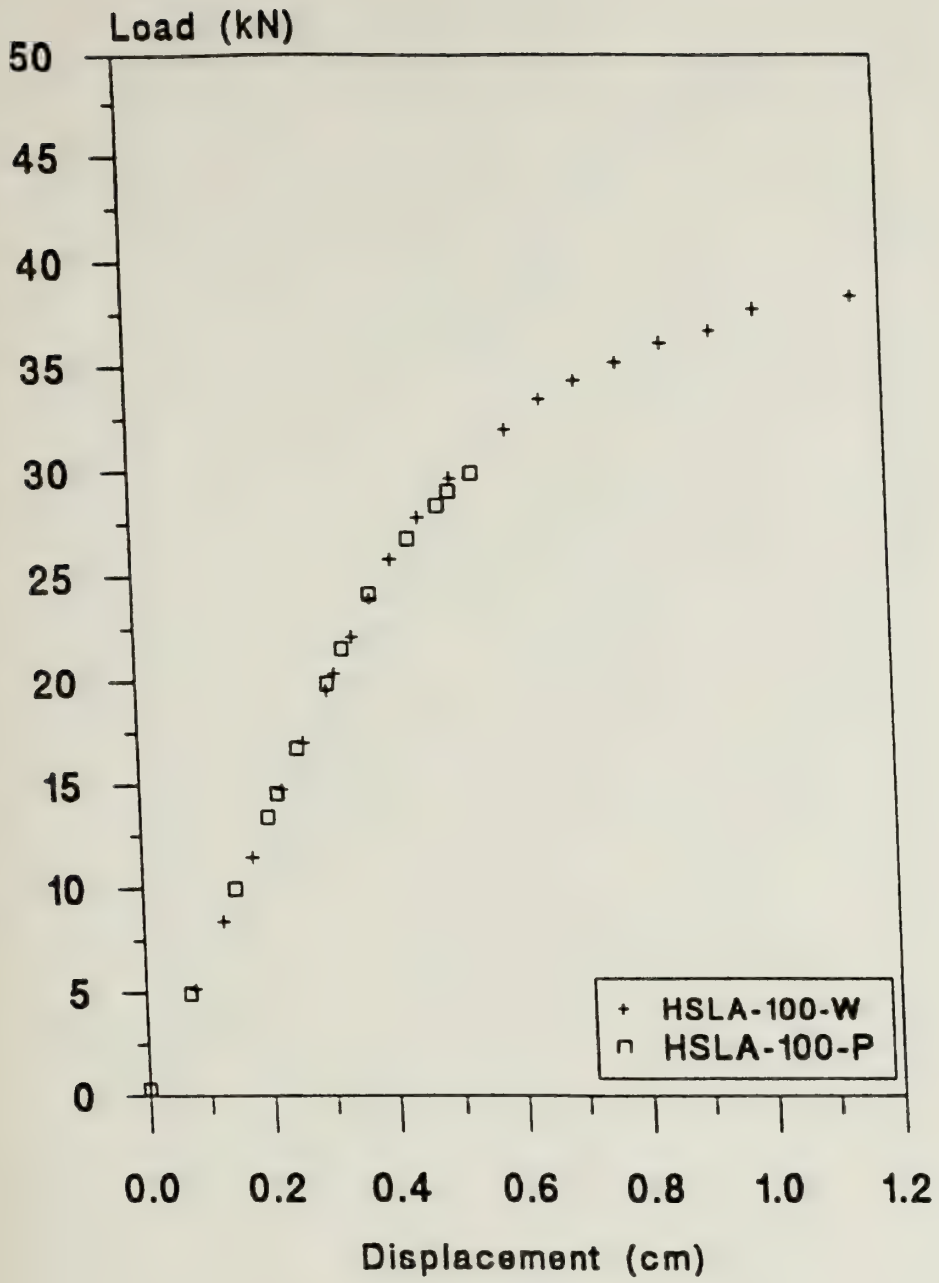

Figure 29: HSLA-100 Displacement-Load Curve

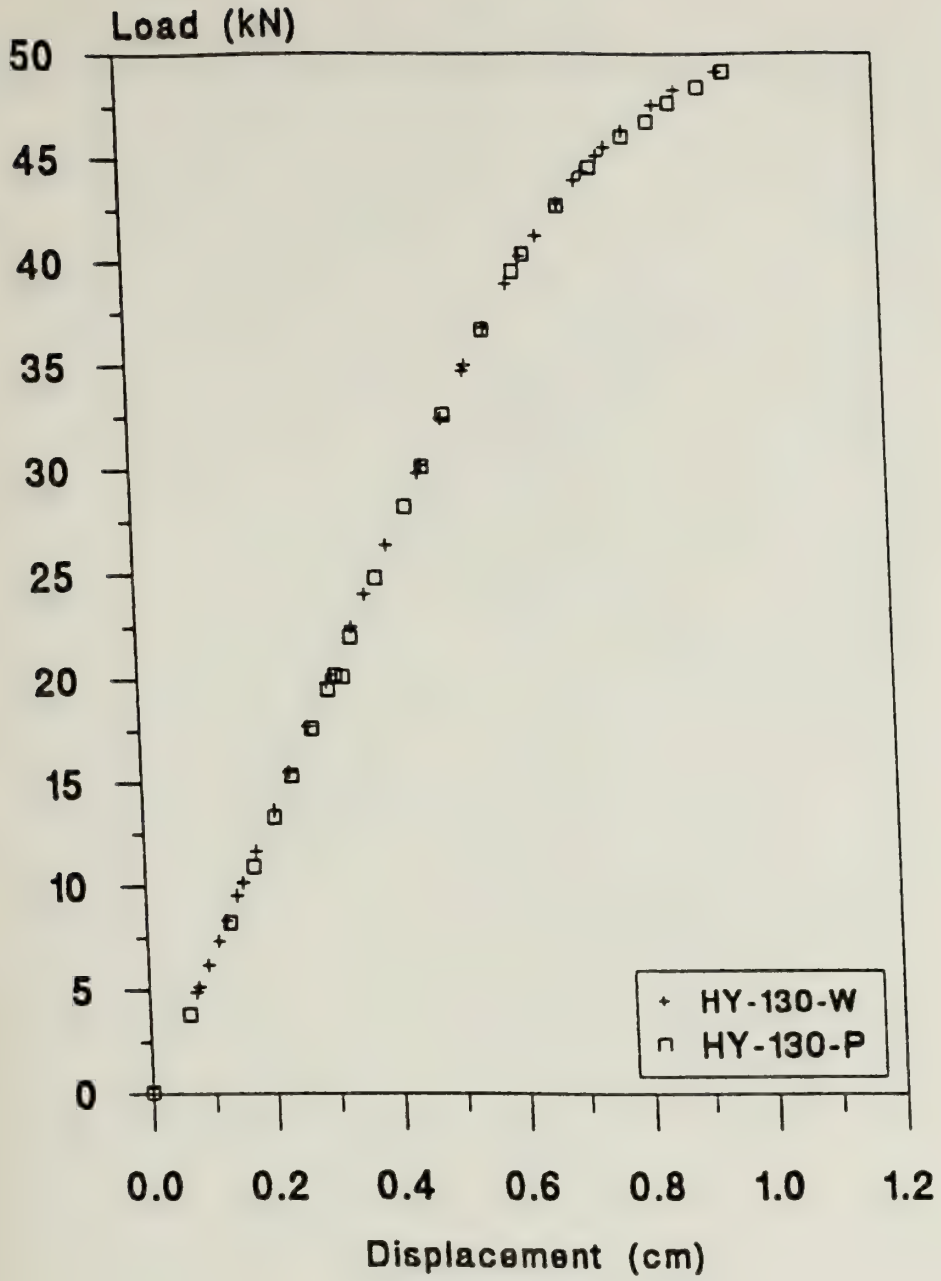

Figure 30: HY-130 Displacement-Load Curve

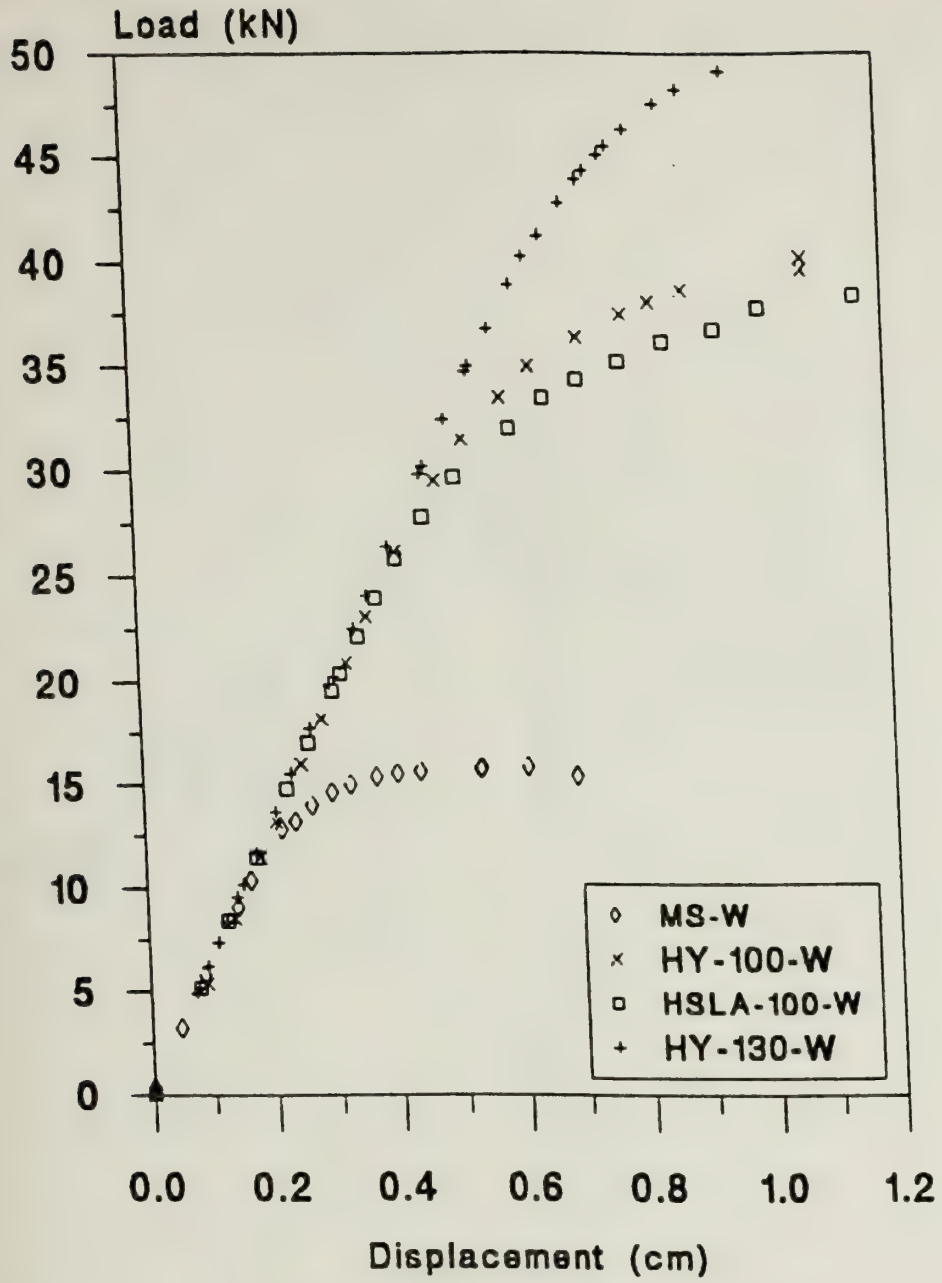

Figure 31: Combined Displacement-Load Curve

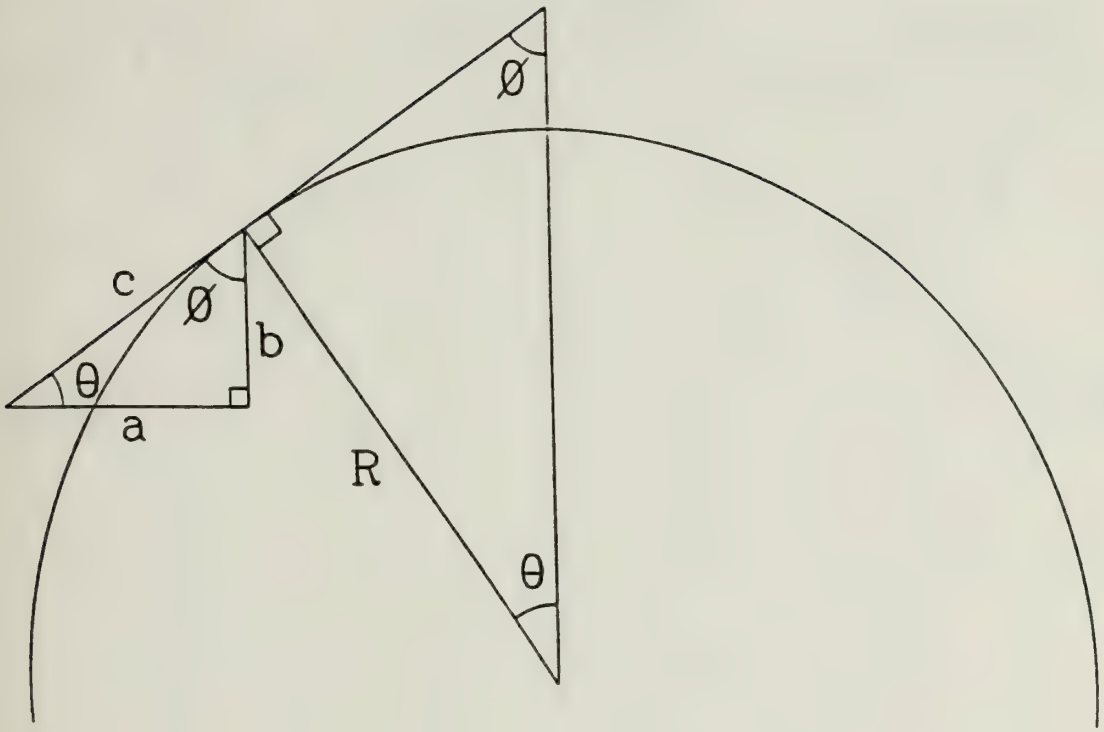

Figure 32: Similar Triangles

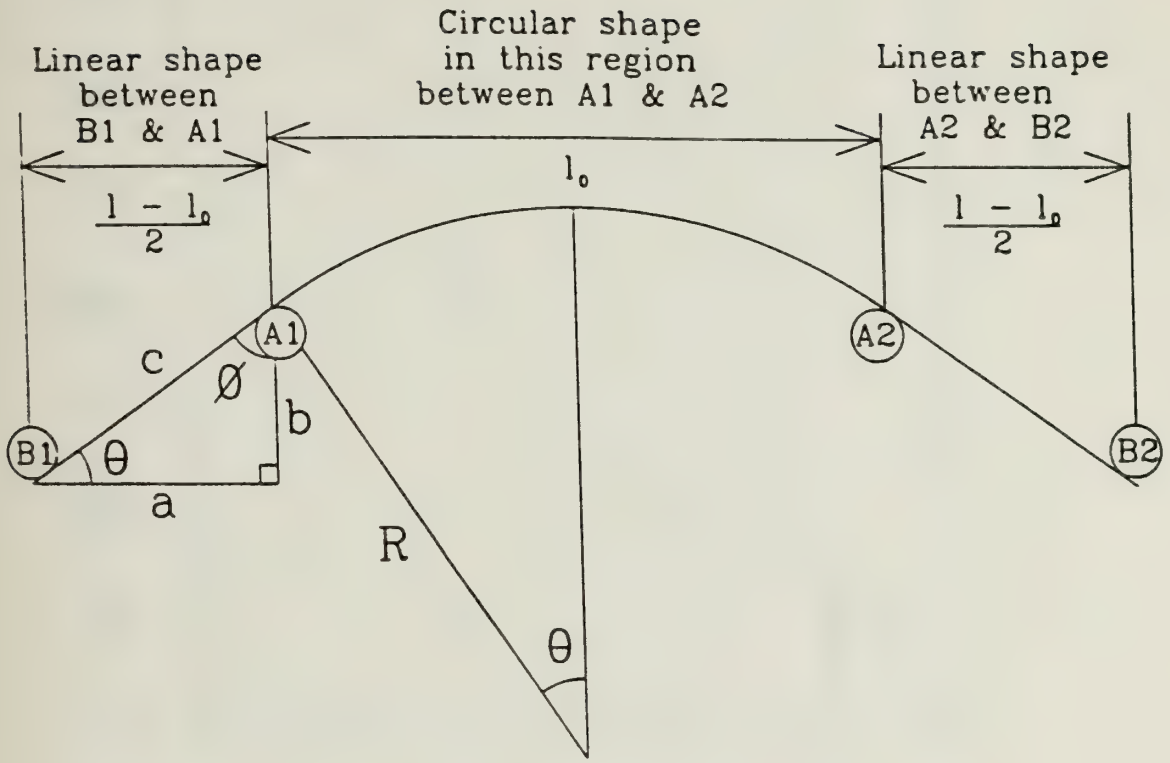

Figure 33: First Approximation of Curvature

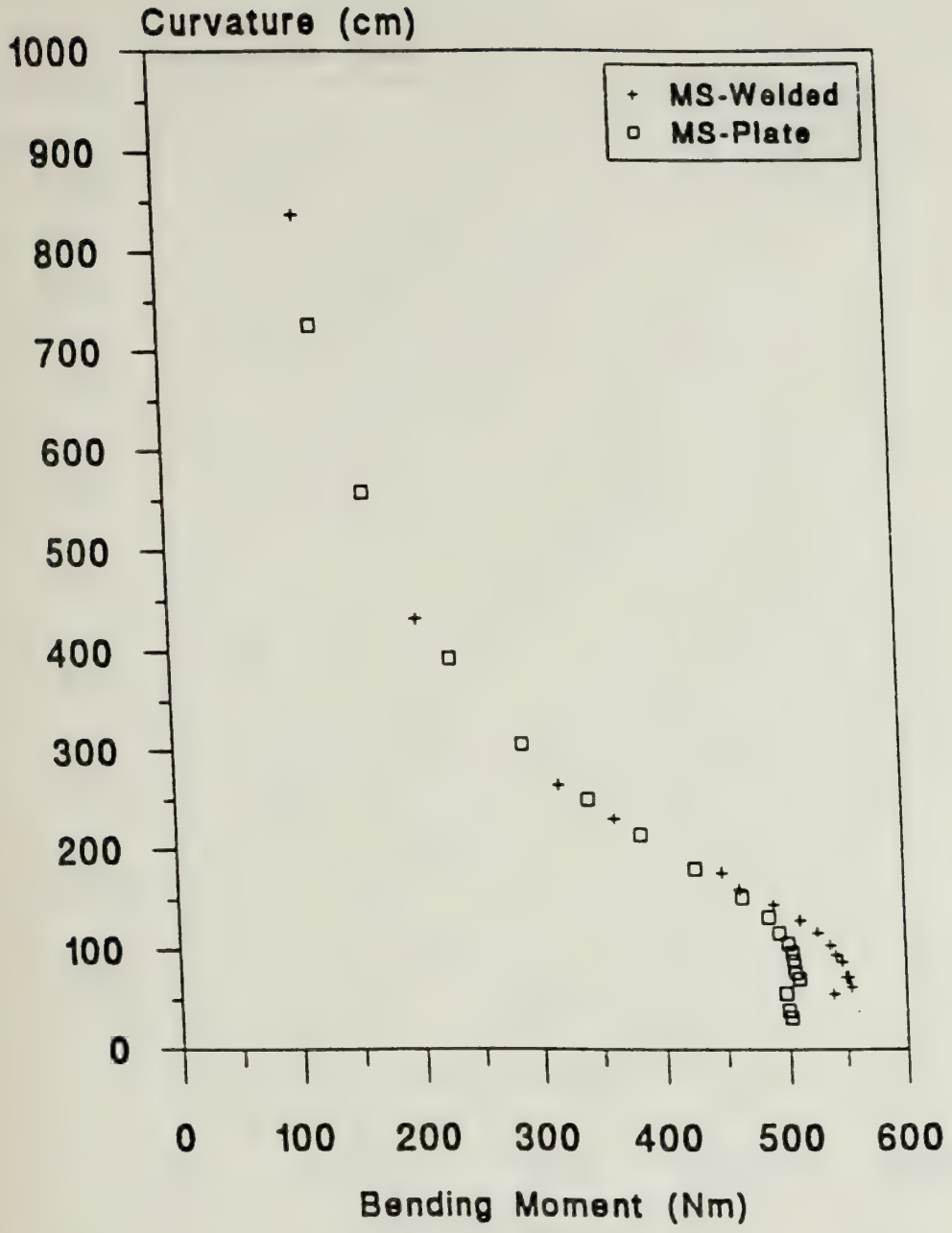

Figure 34: Mild Steel Moment-Curvature Diagram

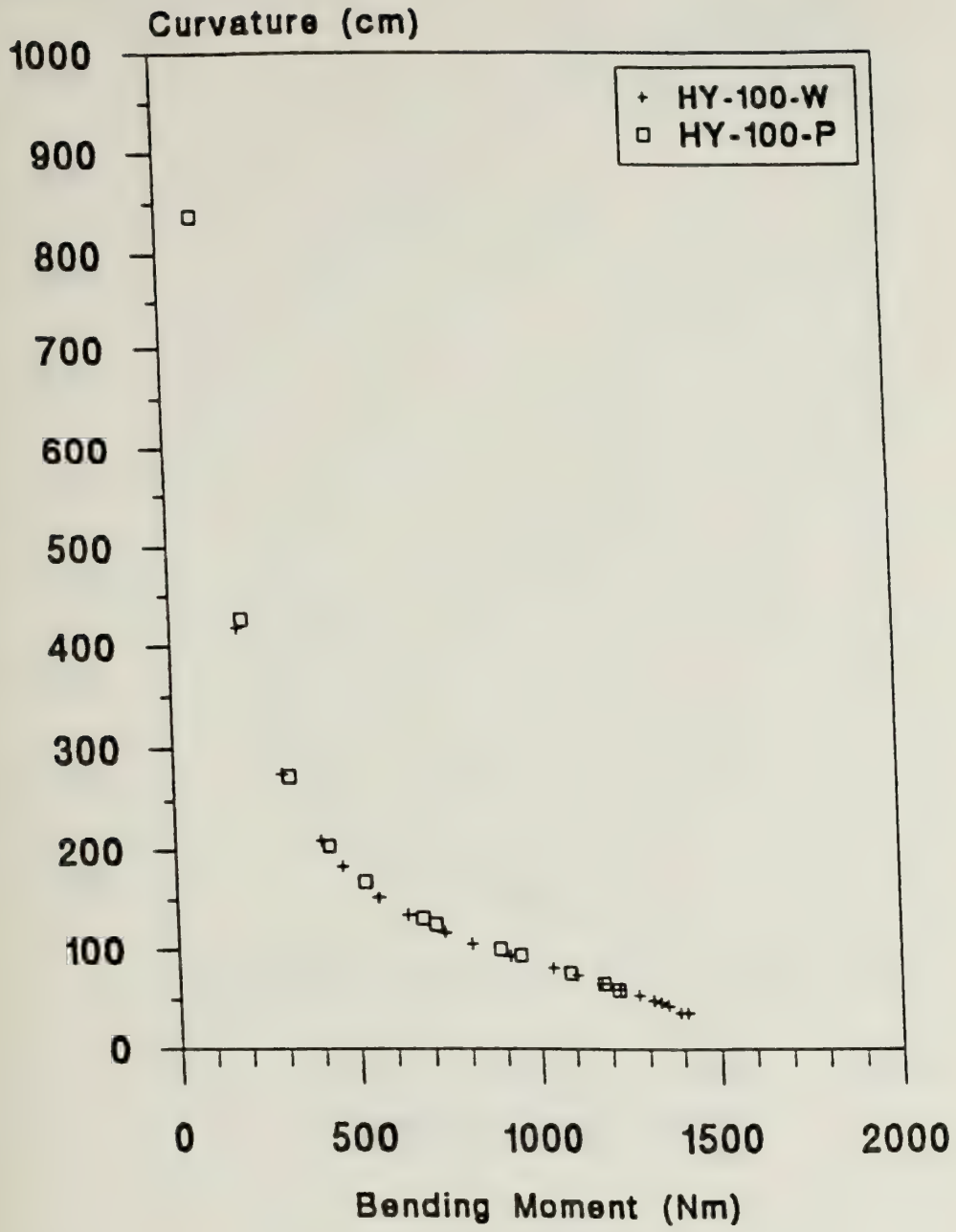

Figure 35: HY-100 Moment-Curvature Diagram

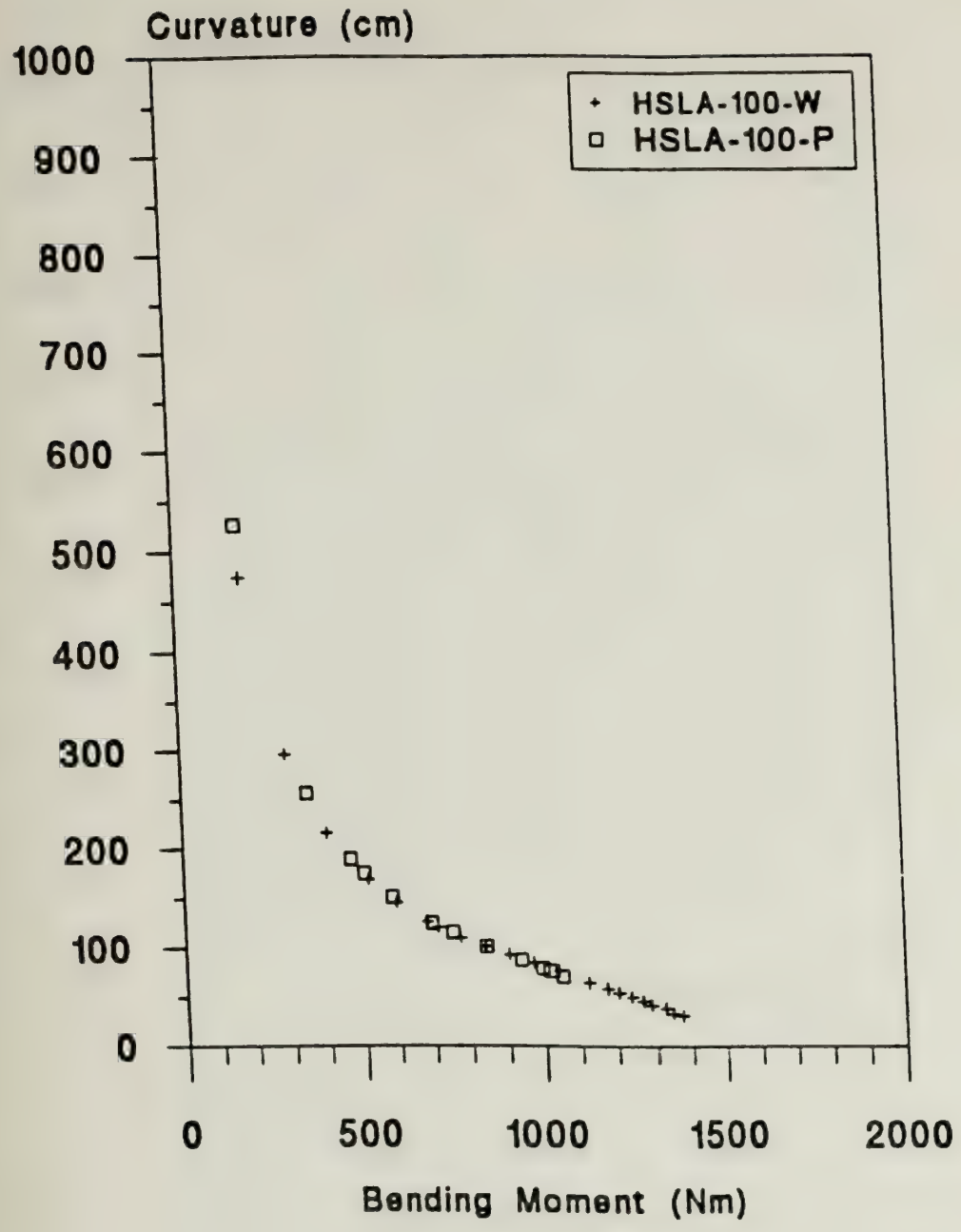

Figure 36: HSLA-100 Moment-Curvature Diagram

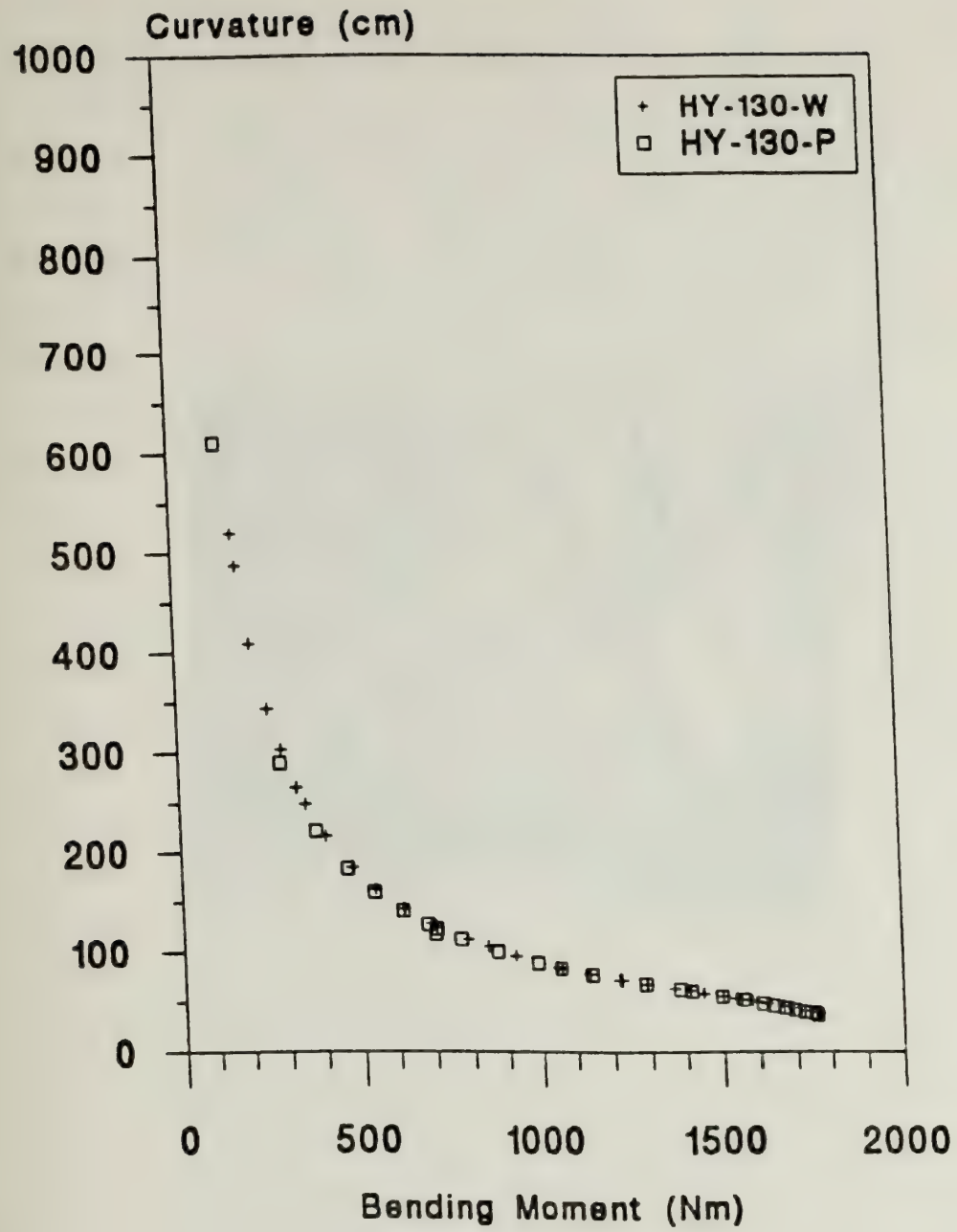

Figure 37: HY-130 Moment-Curvature Diagram

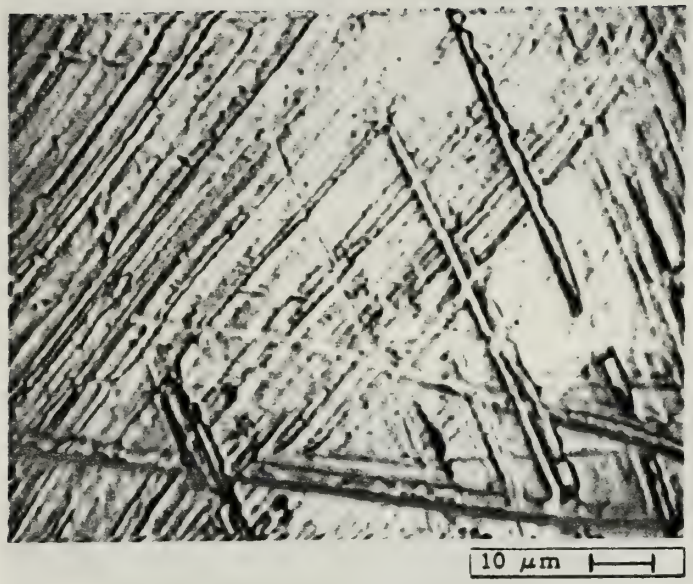

Figure 39: HY-130 Baseplate. No Load, 40x Objective Lens

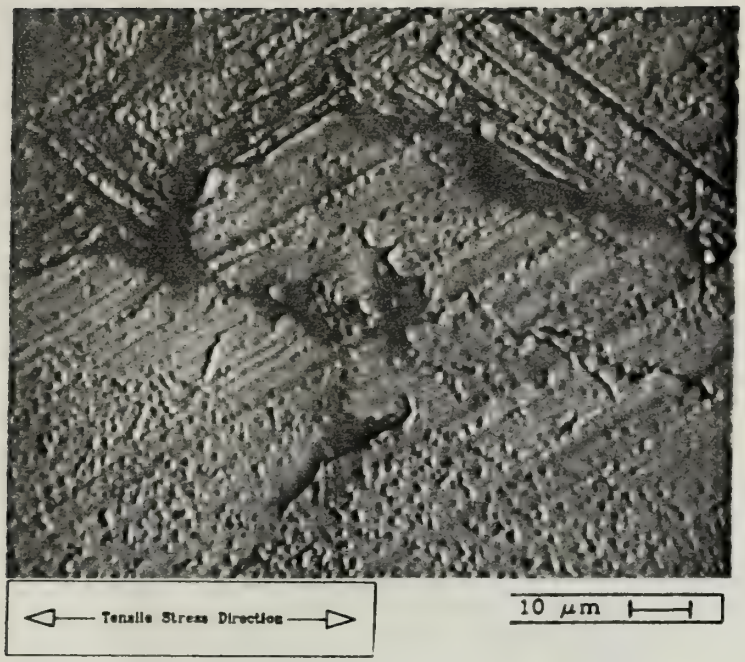

(a)

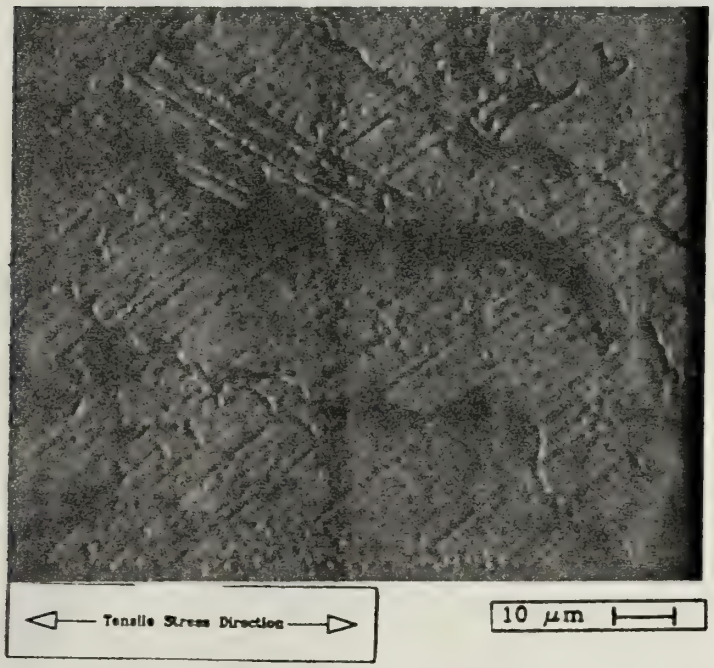

(b) 14 kN Load

Figure 40: Mild Steel, 40x Objective Lens

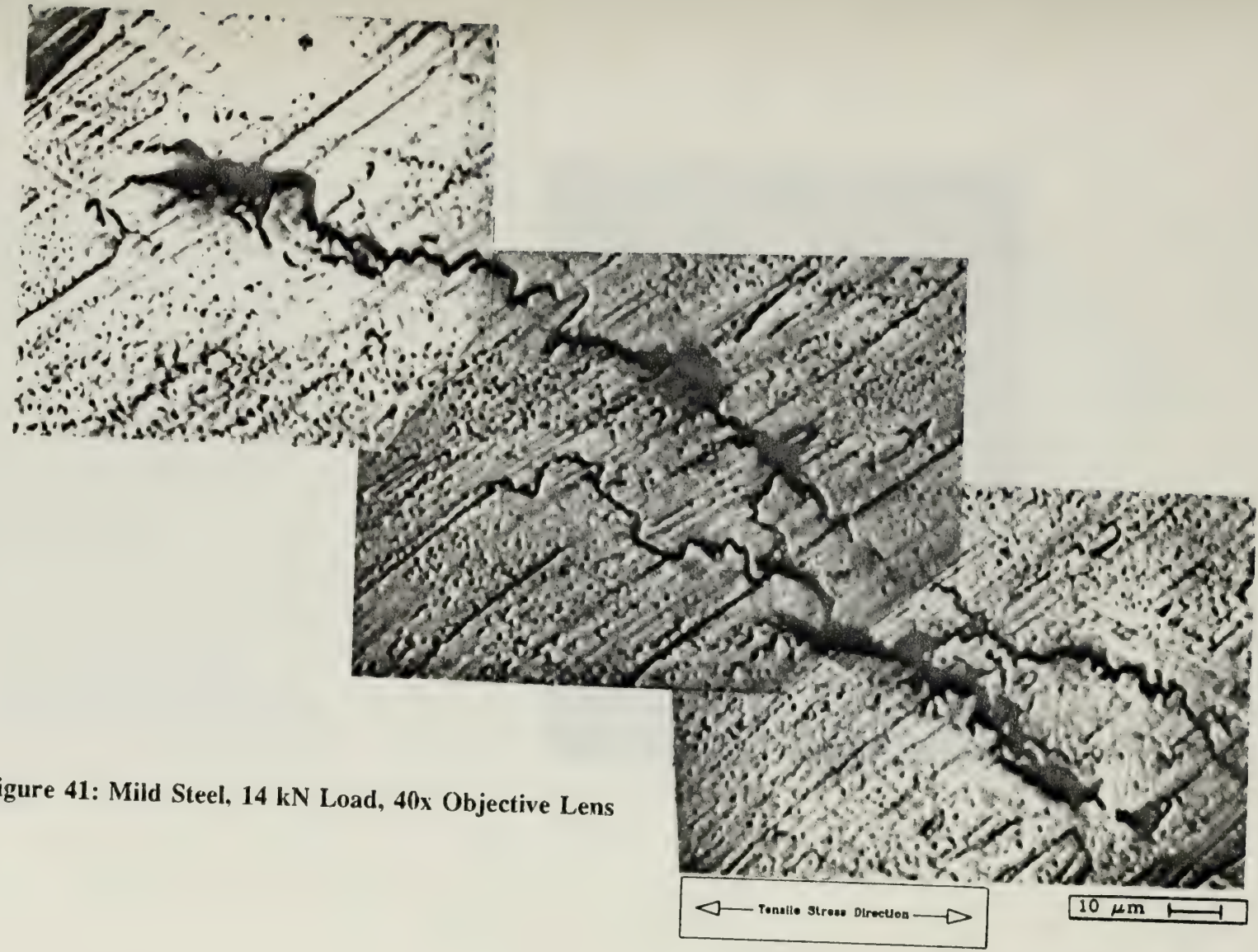

Figure 41: Mild Steel, 14 kN Load, 40x Objective Lens

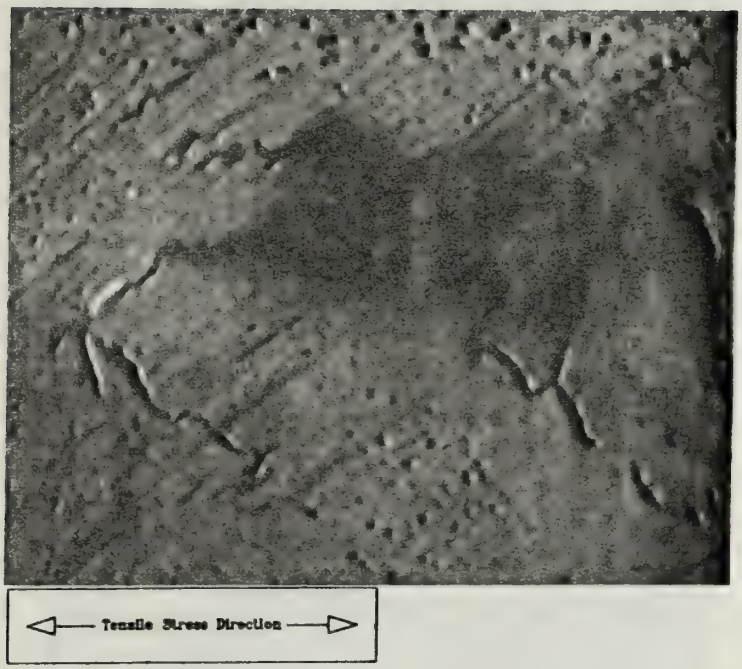

Figure 42: Mild Steel, 14 kN Load, 100x Objective Lens

Figure 43: HY-100, No Load, 40x Objective Lens

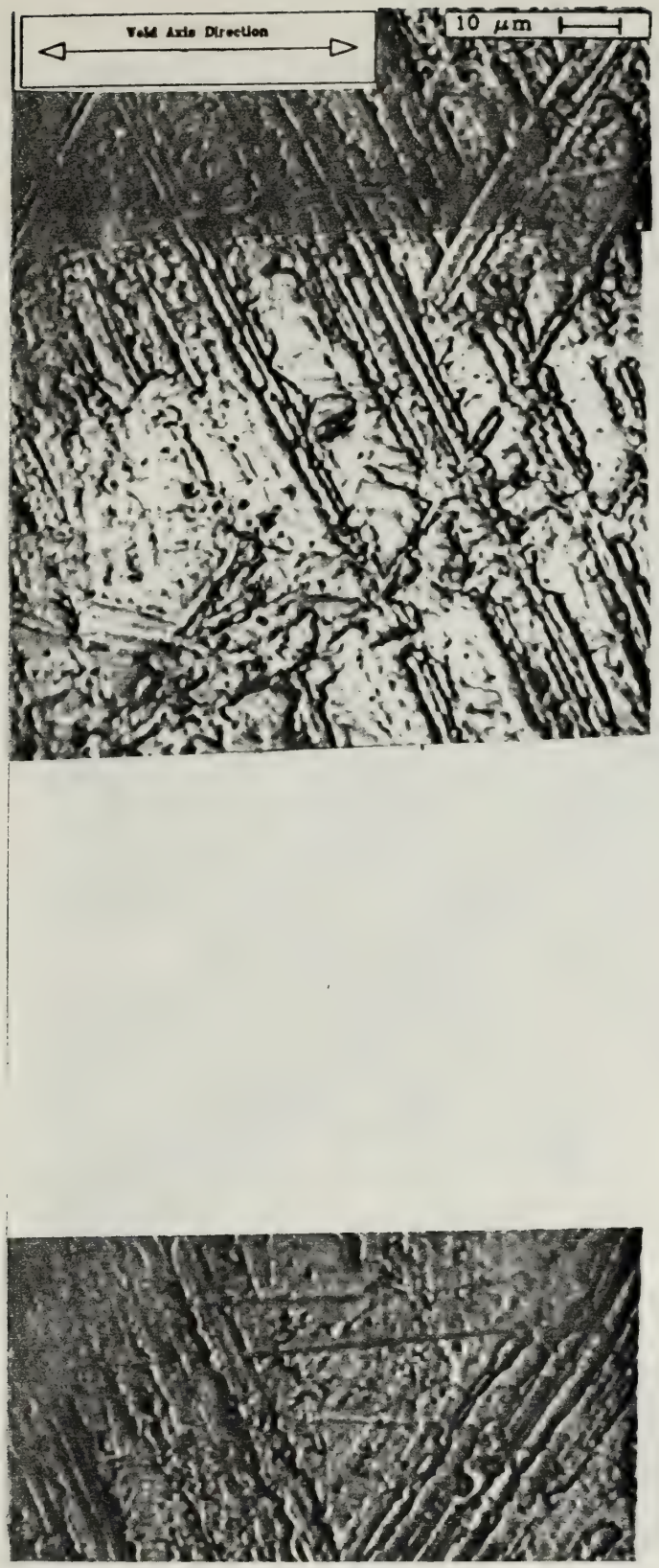

Figure 44: HY-100, No Load, 40x Objective Lens

Figure 45: HY-100, 20 kN Load, 40x Objective Lens

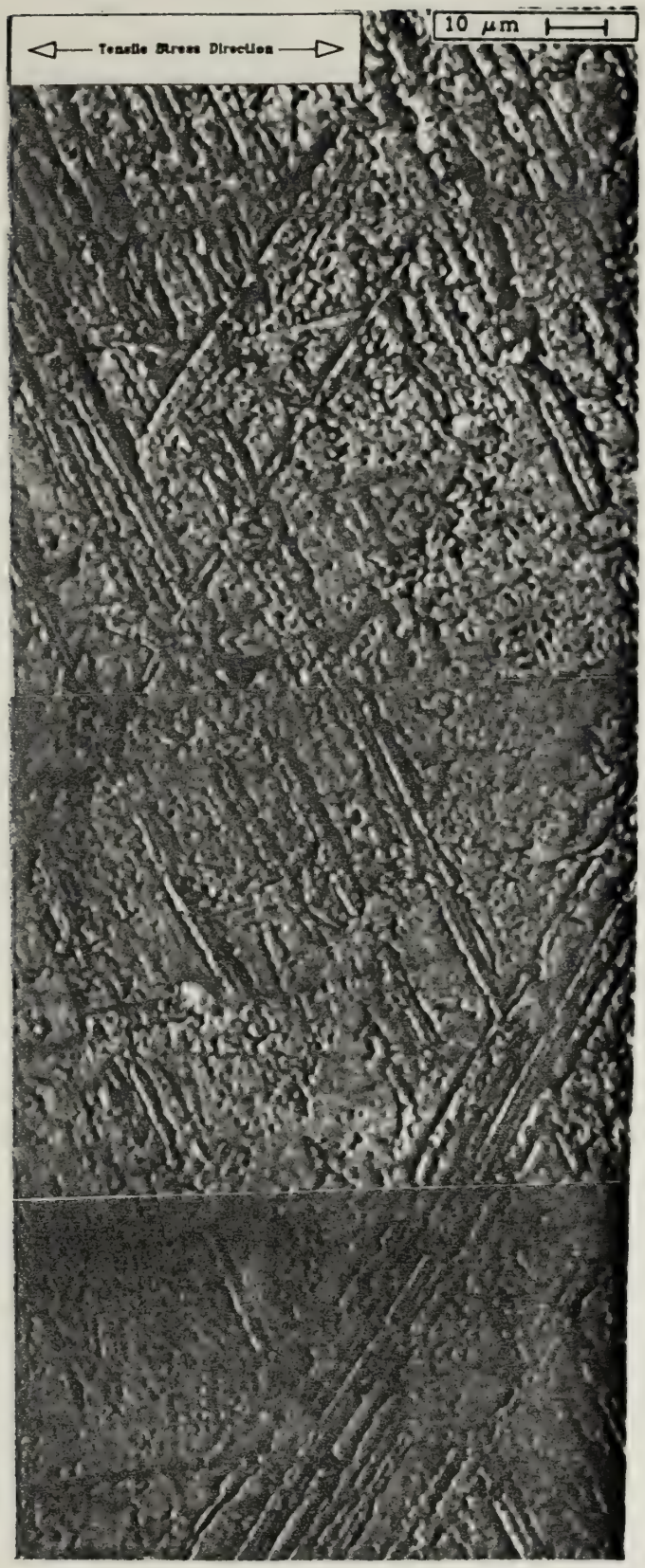

Figure 46: HY-100, 20 kN Load, 40x Objective Lens

Figure 47: HY-100, 33 kN Load, 40x Objective Lens

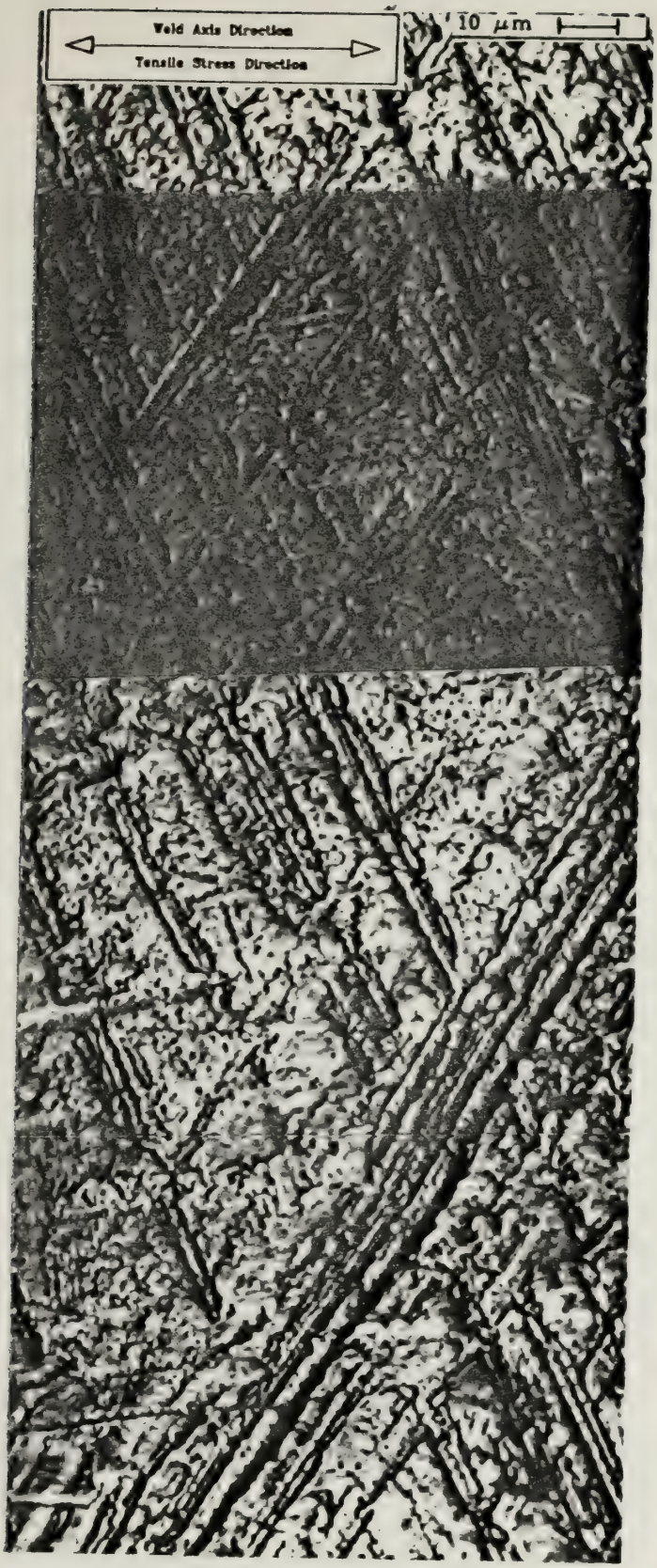

Figure 48: HY-100, 33kN Load, 40x Objective Lens

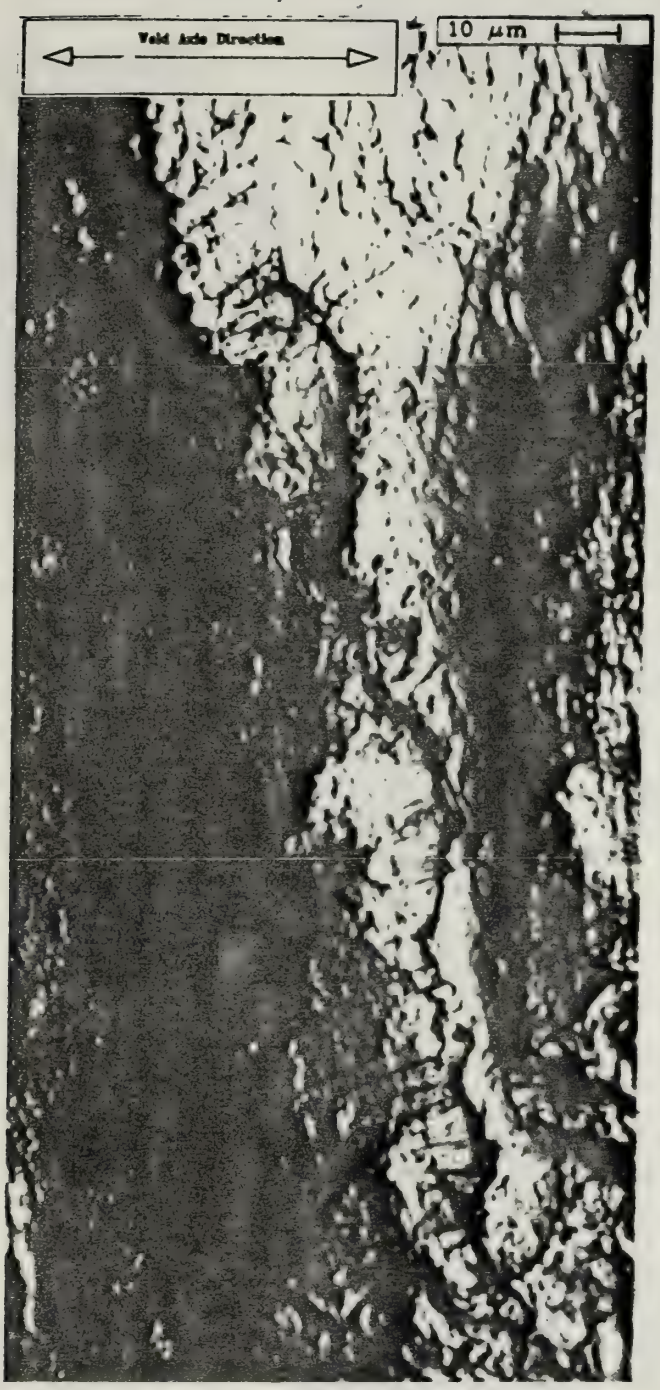

Figure 49: HY-100 Weld Metal, No Load, 40x Objective Lens

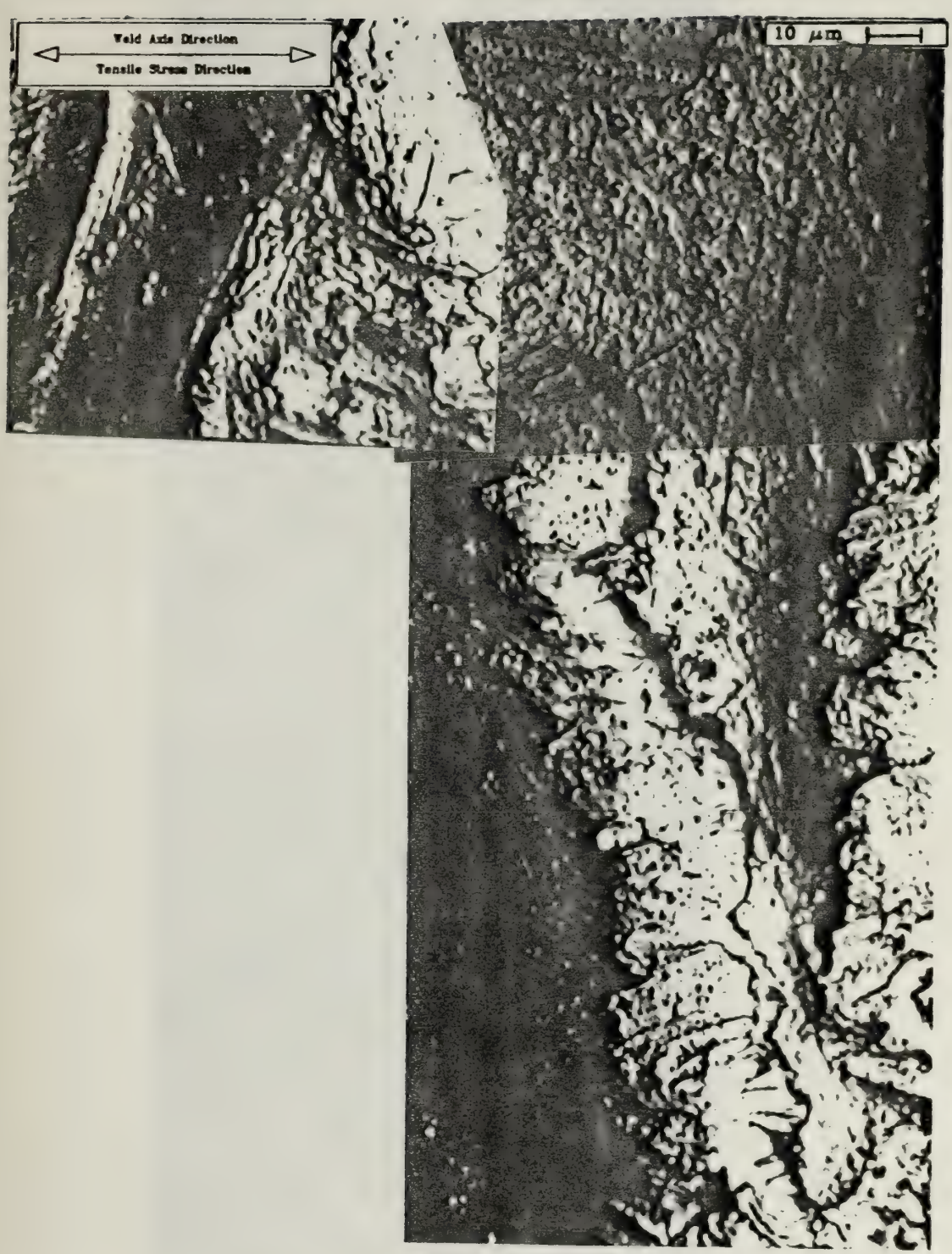

Figure 50: HY-100 Weld Metal, 33 kN Load, 40x Objective Lens

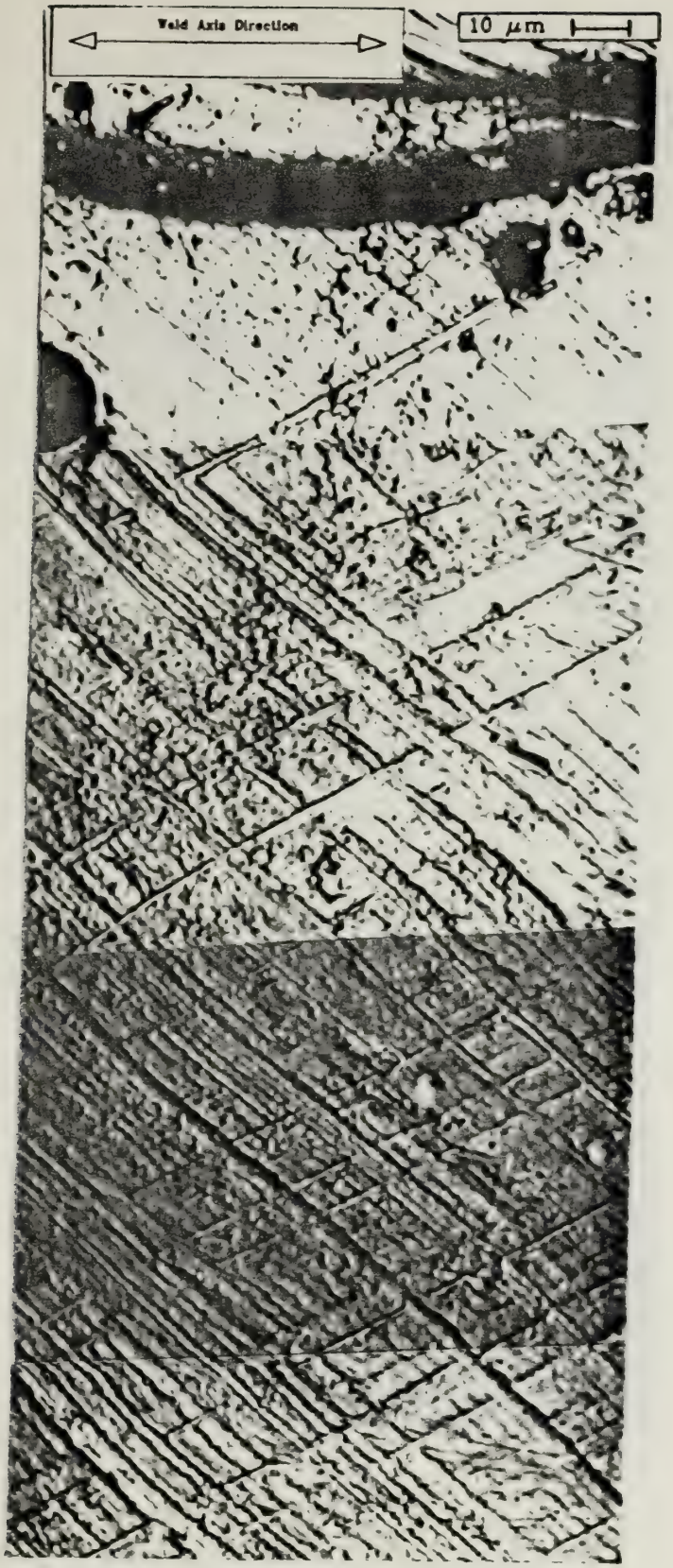

Figure 51: HSLA-100, No Load, 40x Objective Lens

Figure 52: HSLA-100, 30 kN Load, 40x Objective Lens

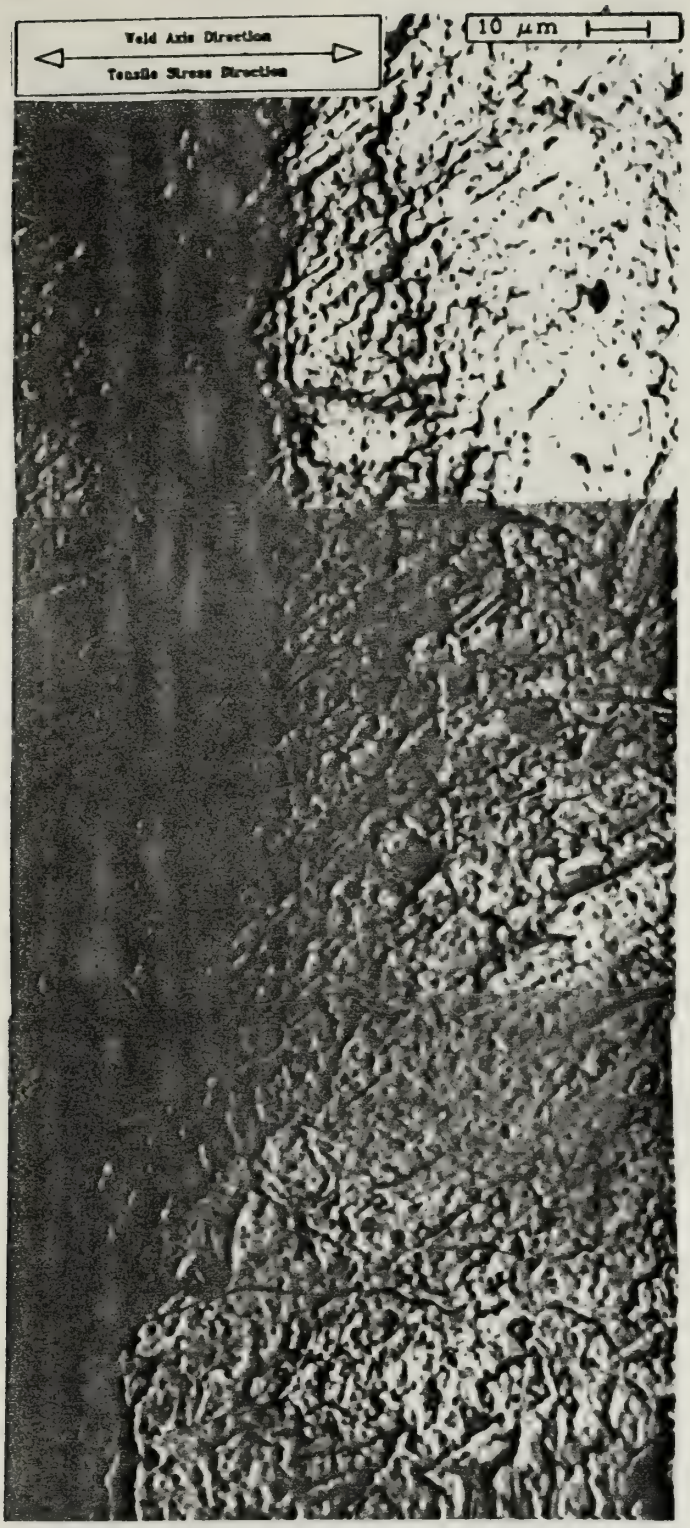

Figure 53: HSLA-100 Weld Metal, 30 kN Load, 40x Objective Lens

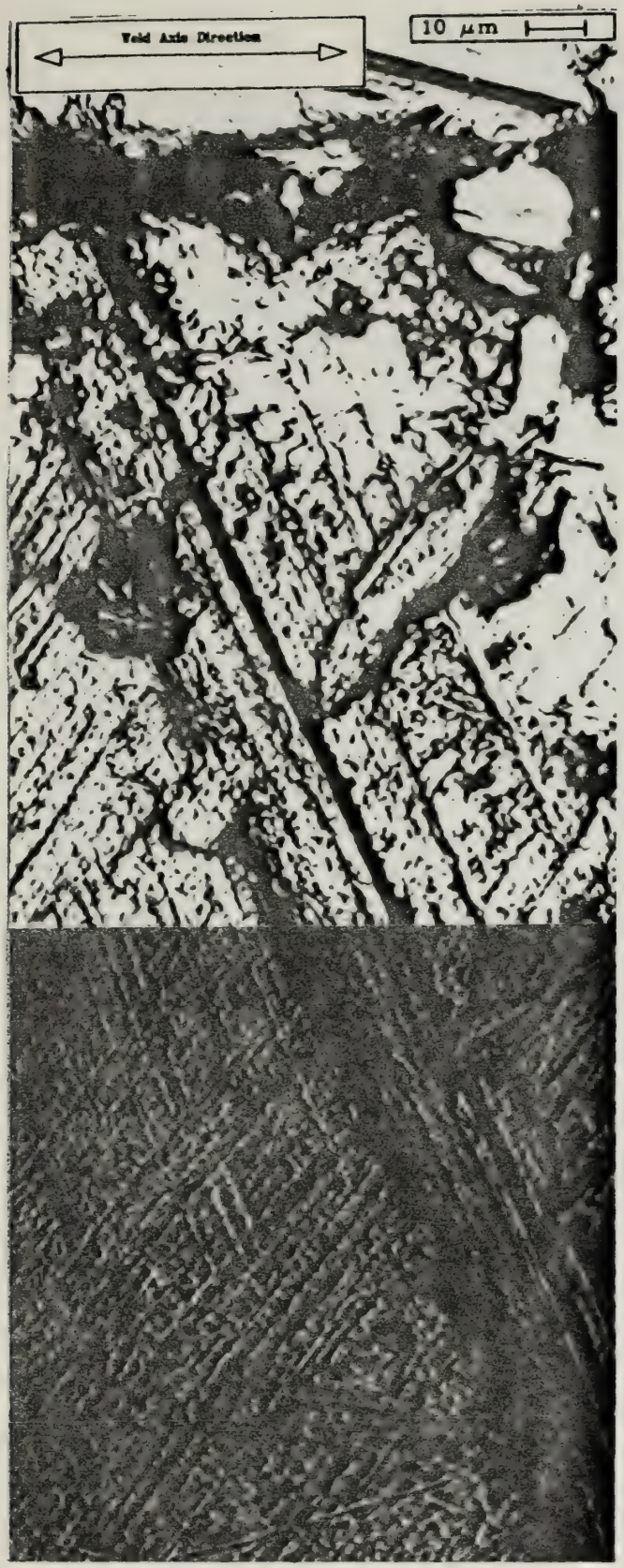

Figure 54: HY-130, No Load, 40x Objective Lens

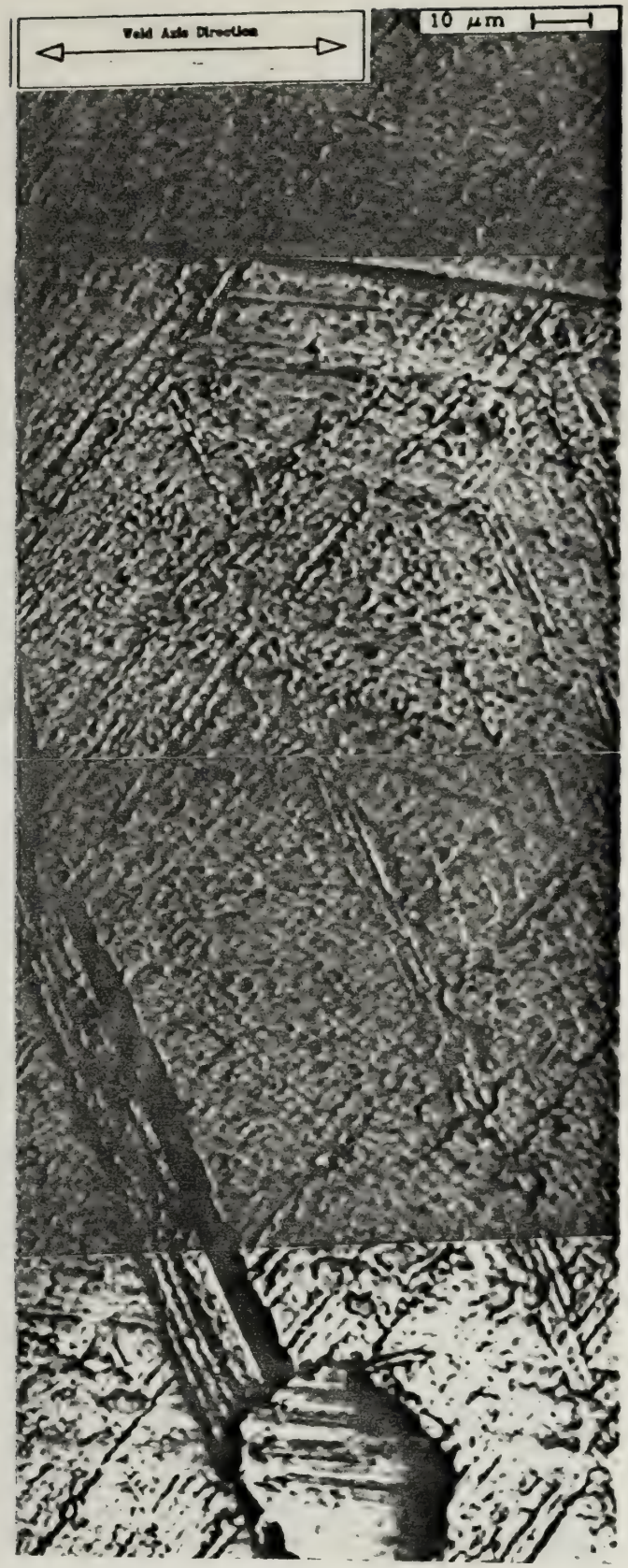

Figure 55: HY-130, No Load, 40x Objective Lens

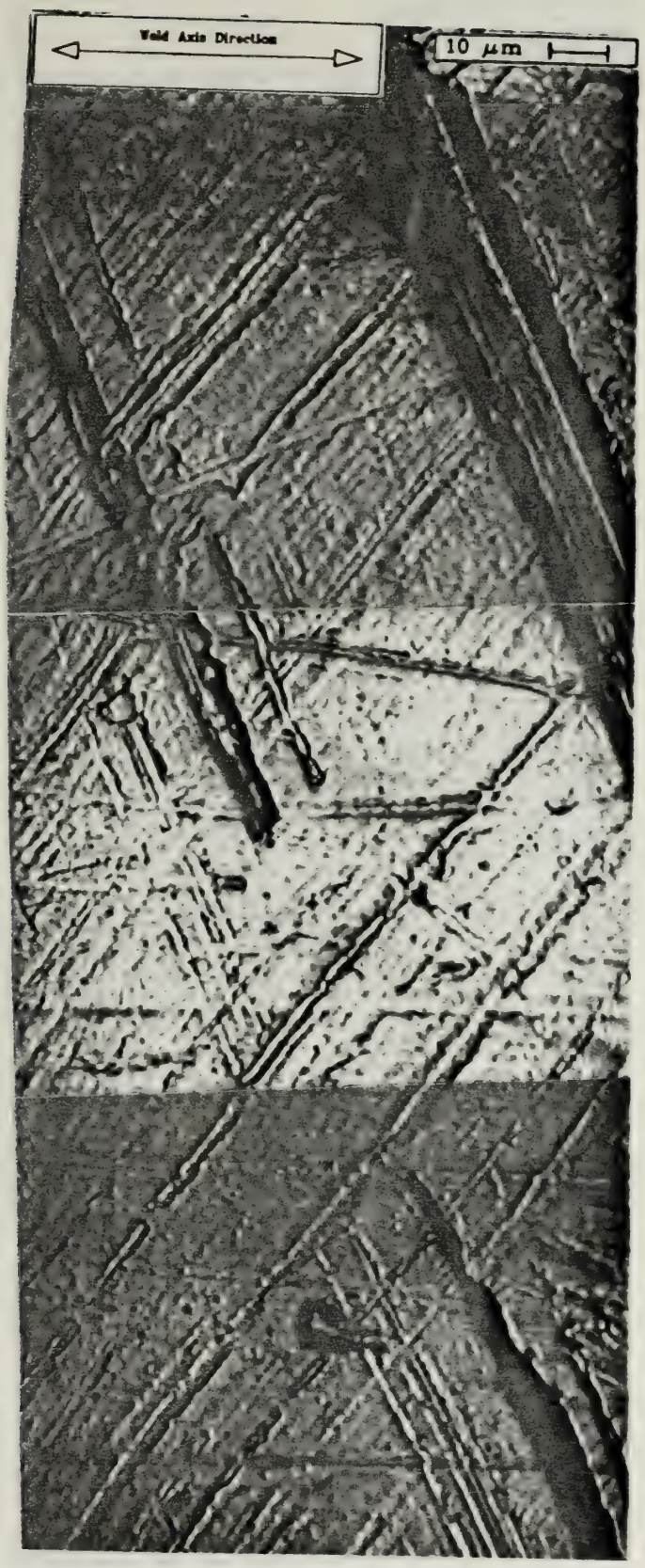

Figure 56: HY-130, No Load, 40x Objective Lens

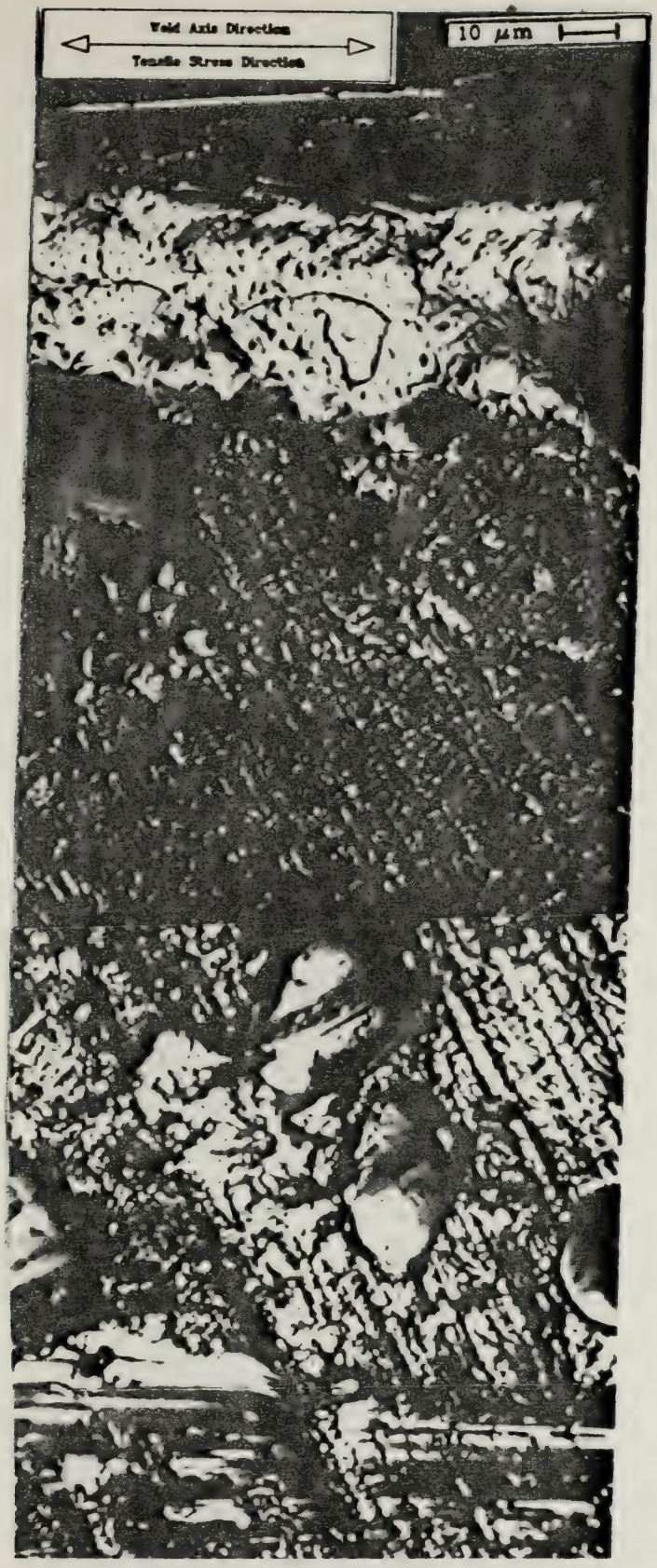

Figure 57: HY-130, 5 kN Load, 40x Objective Lens

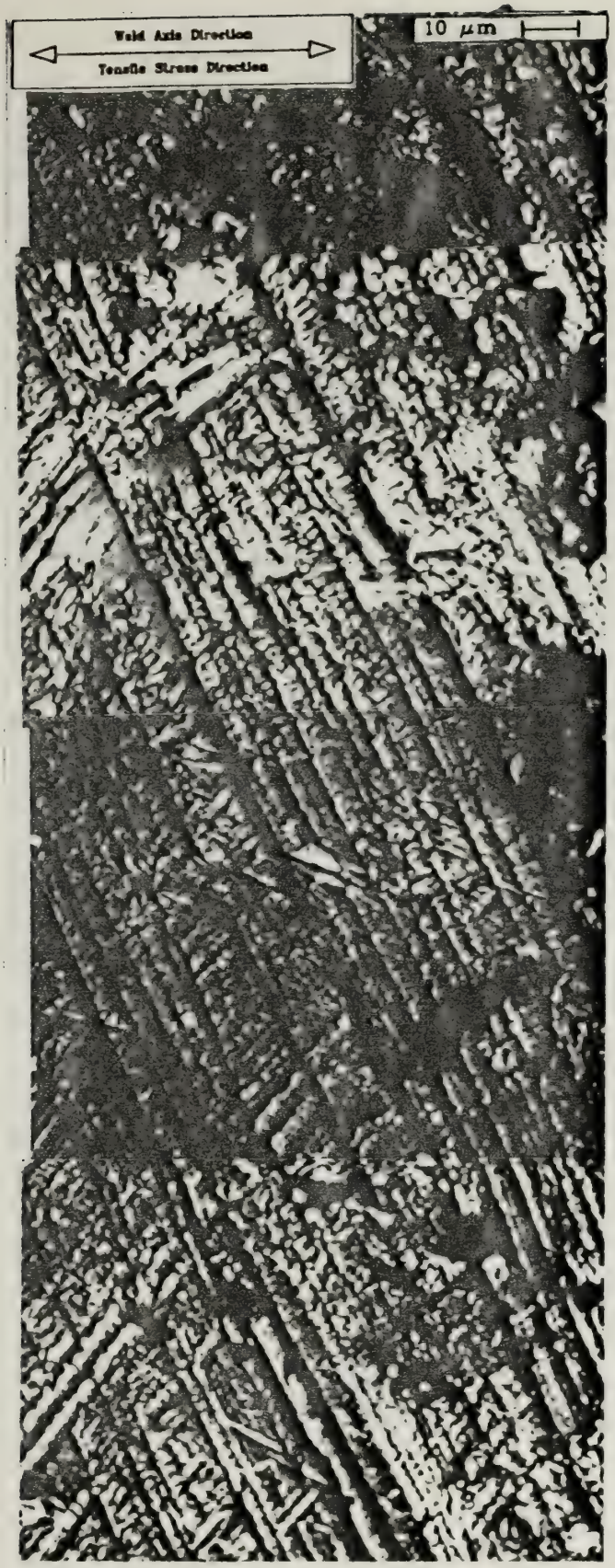

Figure 58: HY-130, 5 kN Load, 40x Objective Lens

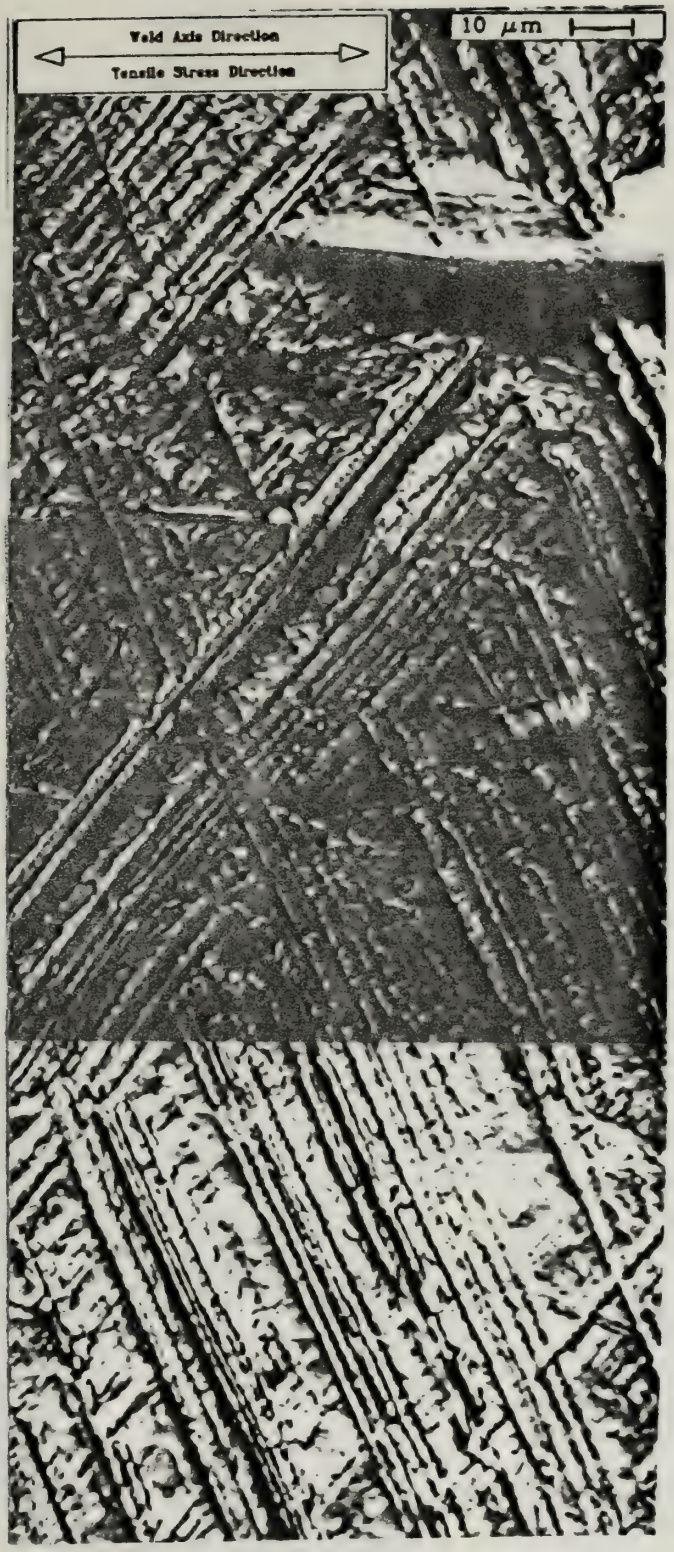

Figure 59: HY-130, 5 kN Load, 40x Objective Lens

Figure 60: HY-130, 40 kN Load, 40x Objective Lens

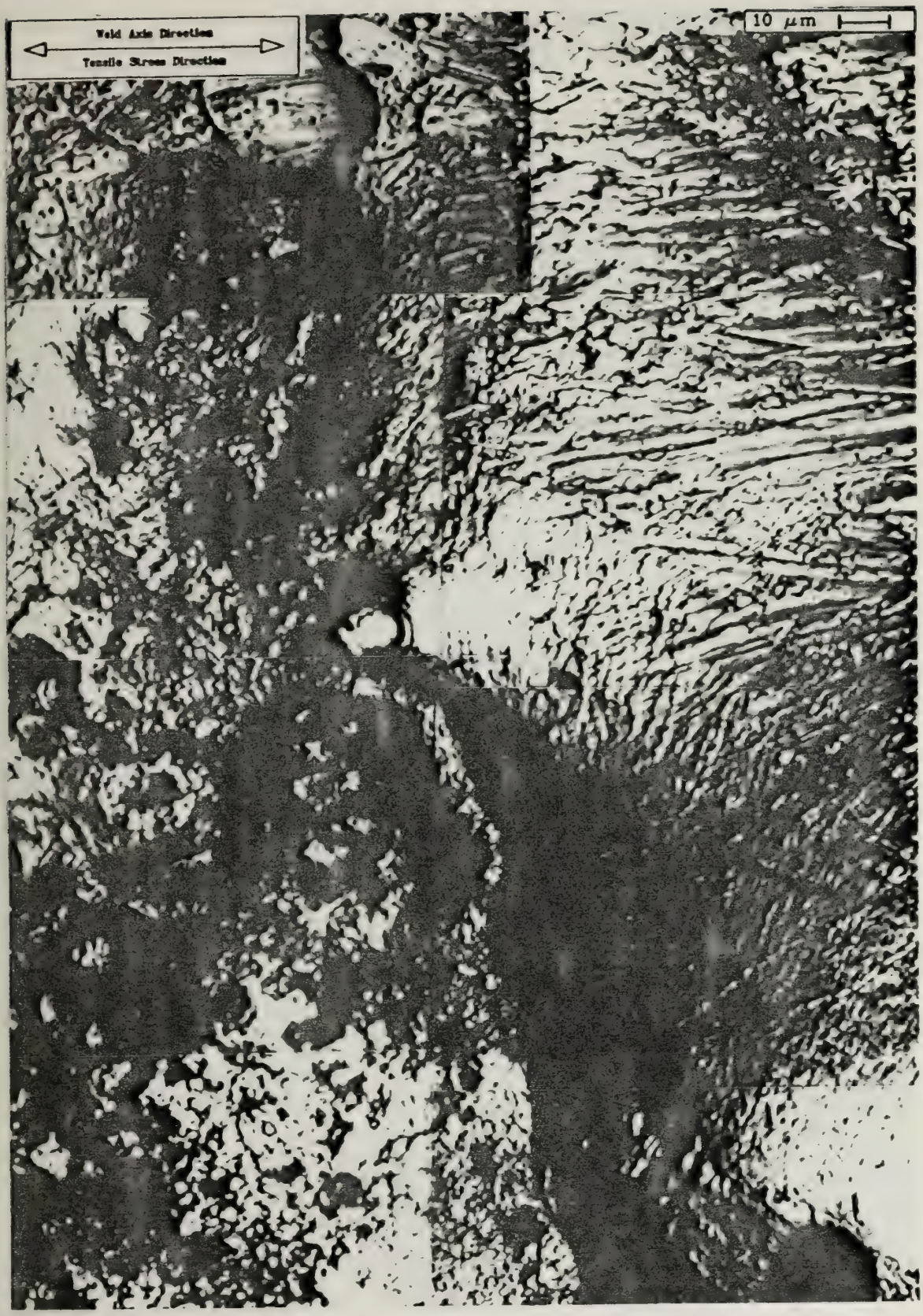

Figure 61: HY-130, 40 kN Load, 40x Objective Lens

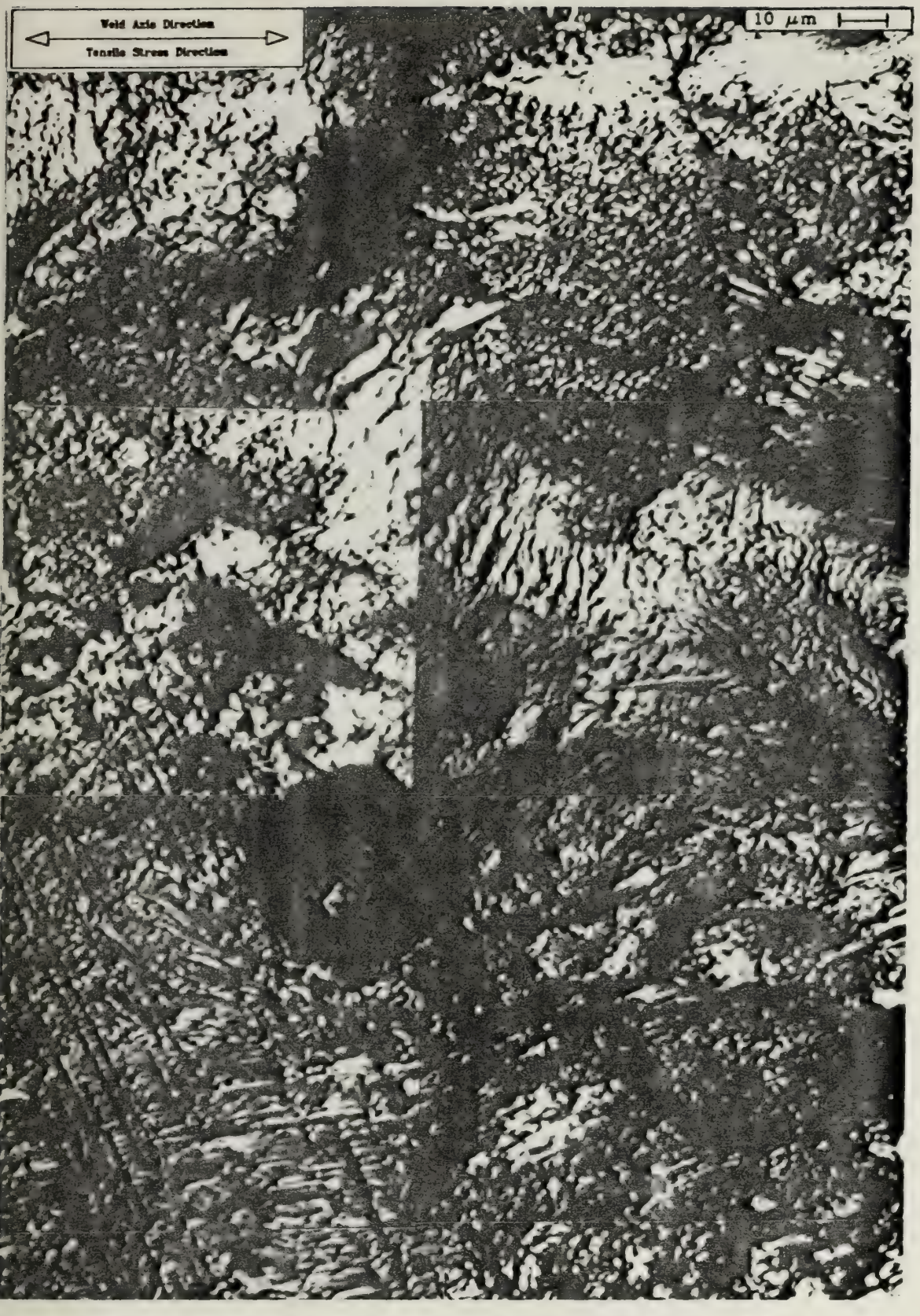

Figure 62: HY-130, 50 kN Load, 40x Objective Lens

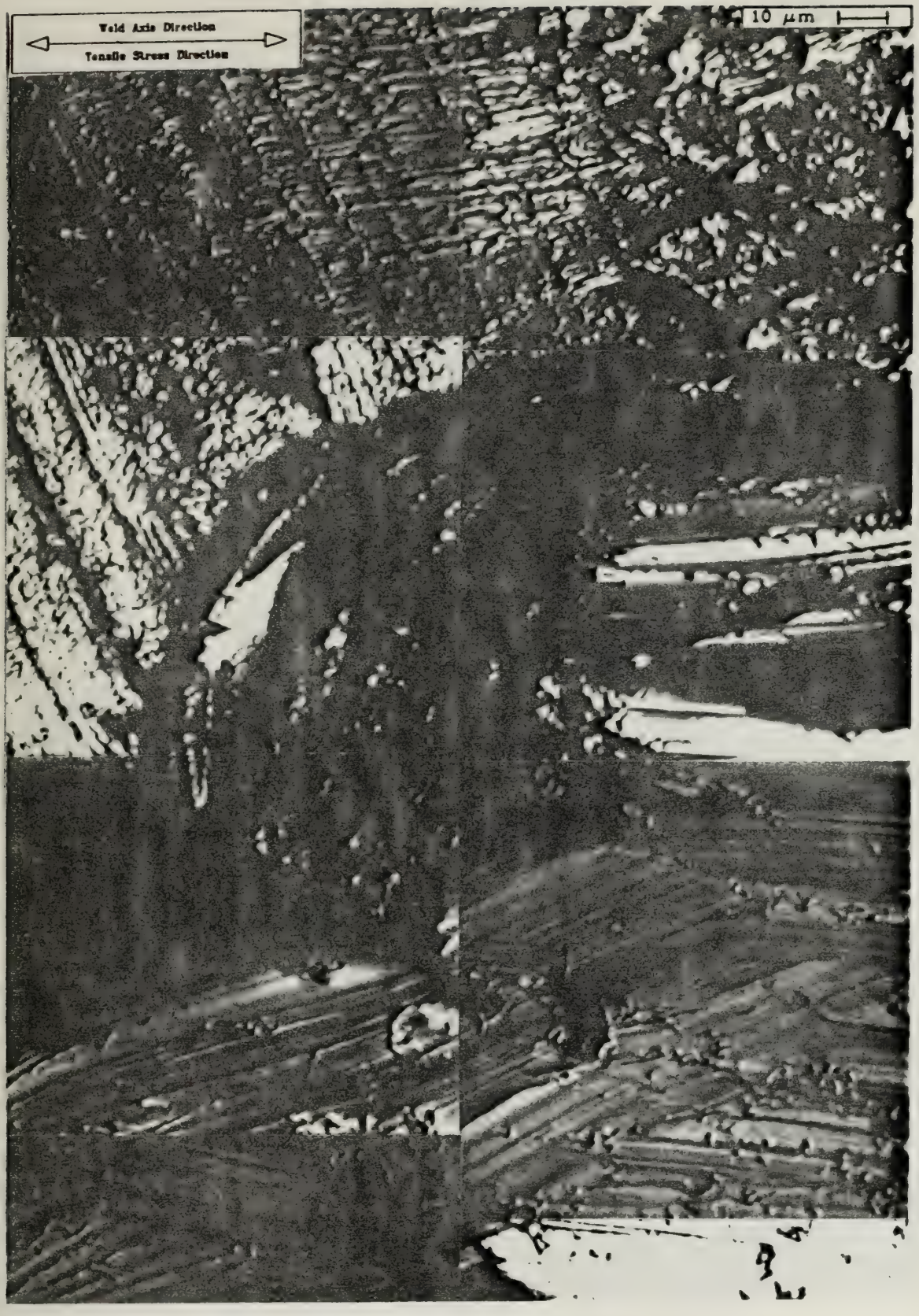

Figure 63: HY-130, 50 kN Load, 40x Objective Lens

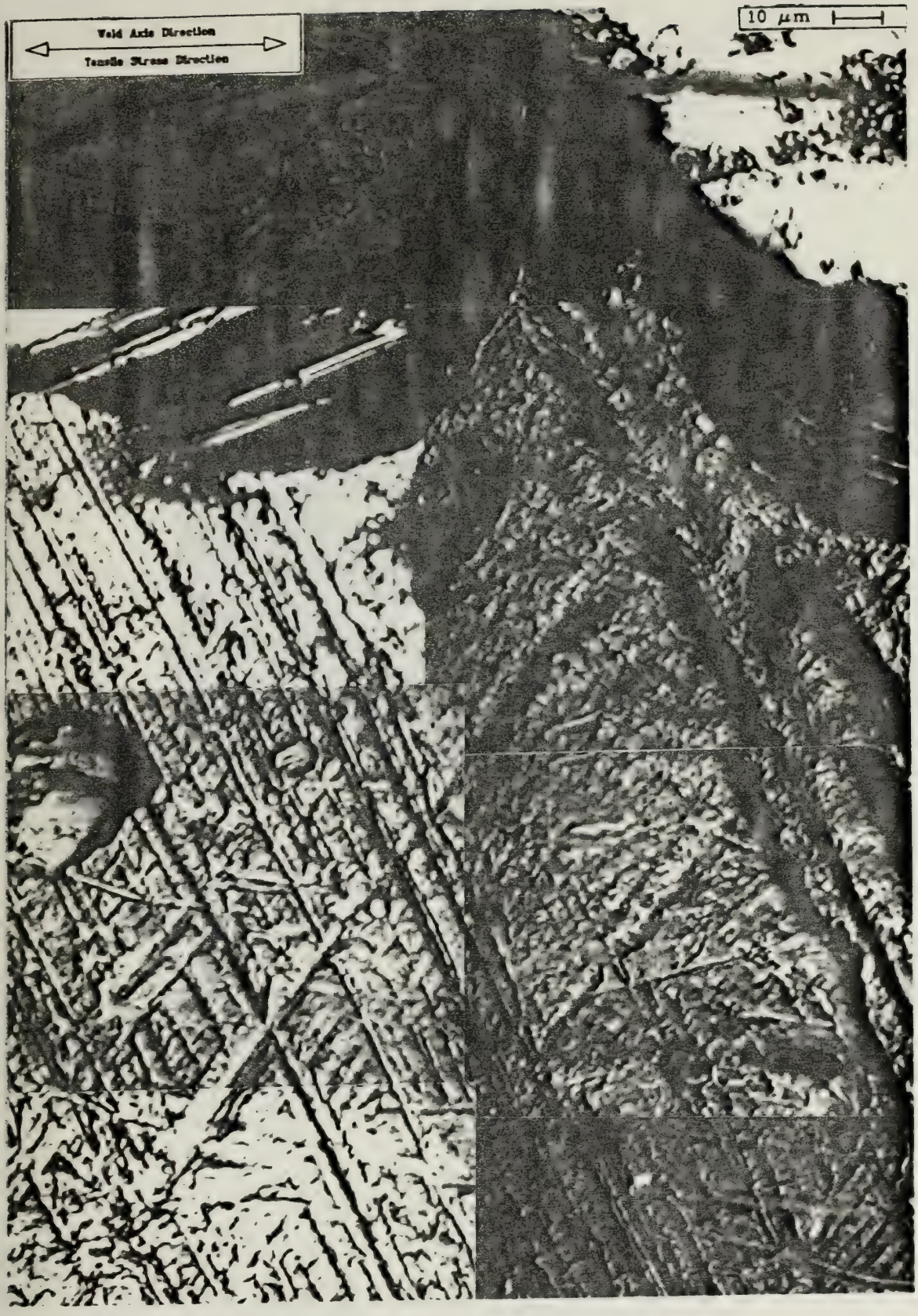

Figure 64: HY-130, 50 kN Load, 40x Objective Lens

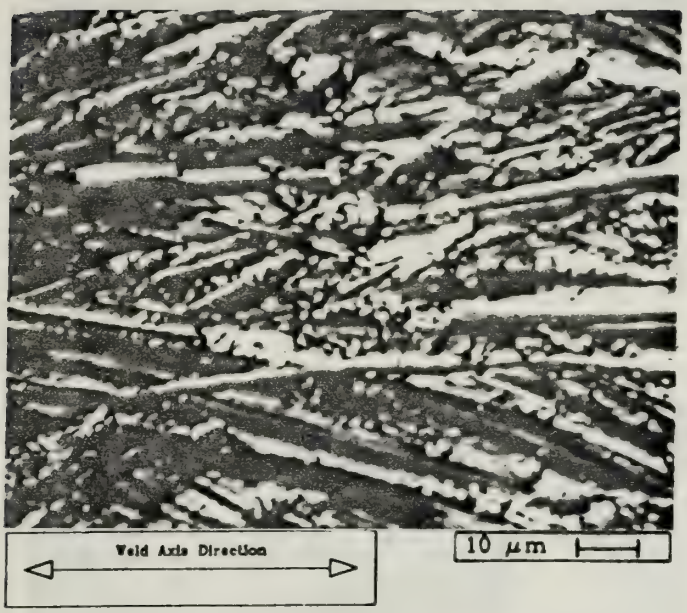

Figure 65: HY-130 Weld Metal, No Load, 40x Objective Lens

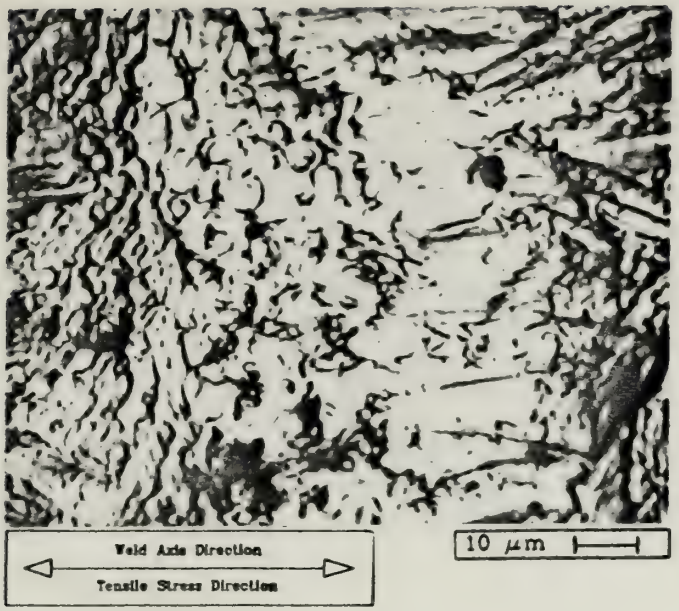

(a)

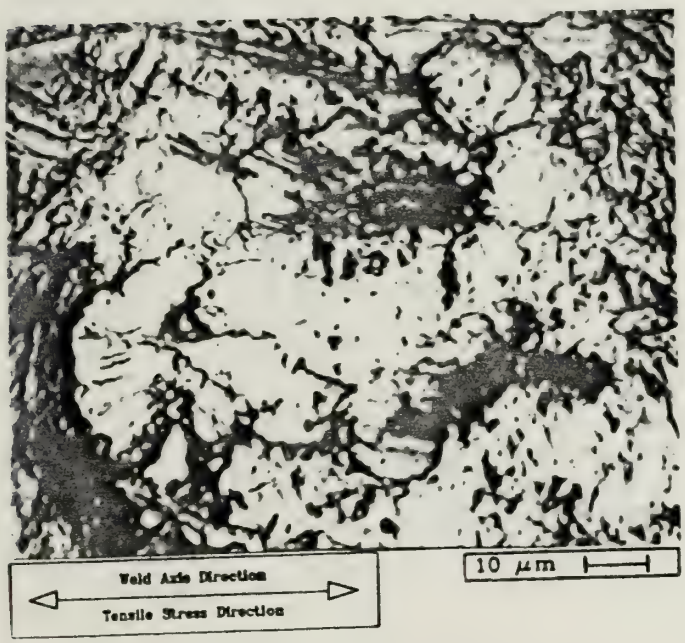

(b)

Figure 66: HY-130 Weld Metal, 5 kN Load, 40x Objective Lens

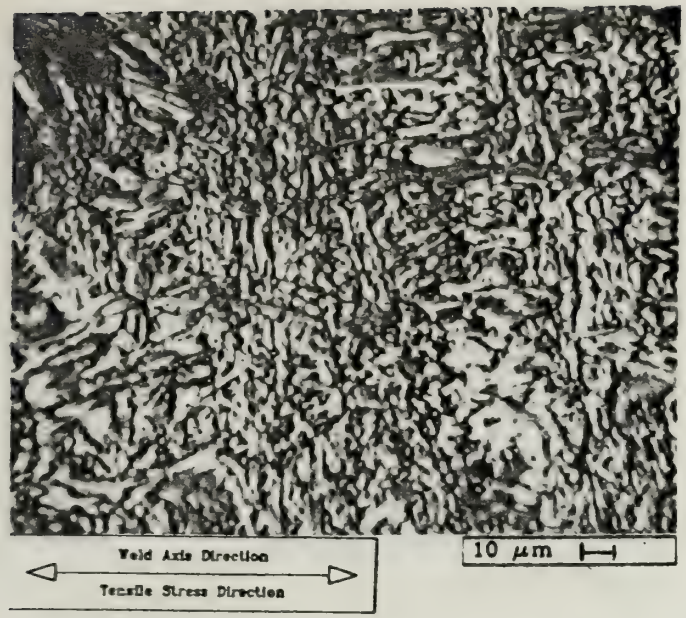

(a) 20x Objective Lens

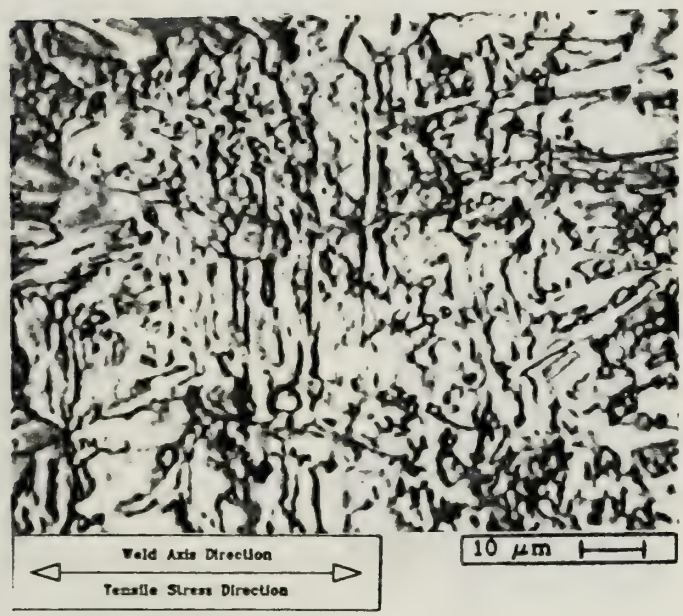

(b) 40 x Objective Lens

Figure 67: HY-130 Weld Metal, 40 kN Load

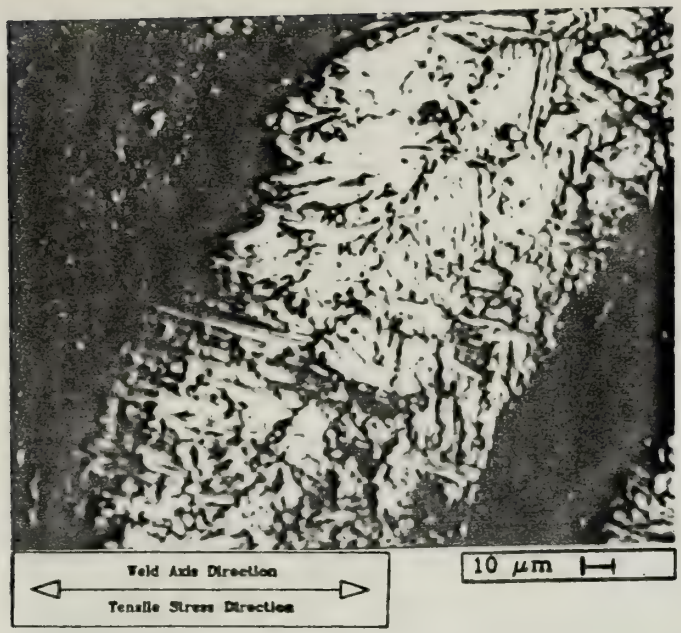

(a) 20x Objective Lens

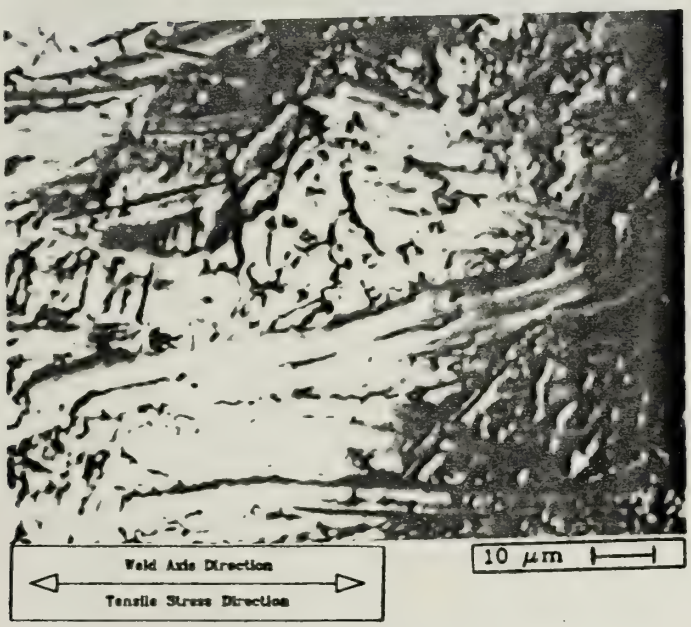

(b) 40x Objective Lens

Figure 68: HY-130 Weld Metal, 40 kN Load, 40x Objective Lens

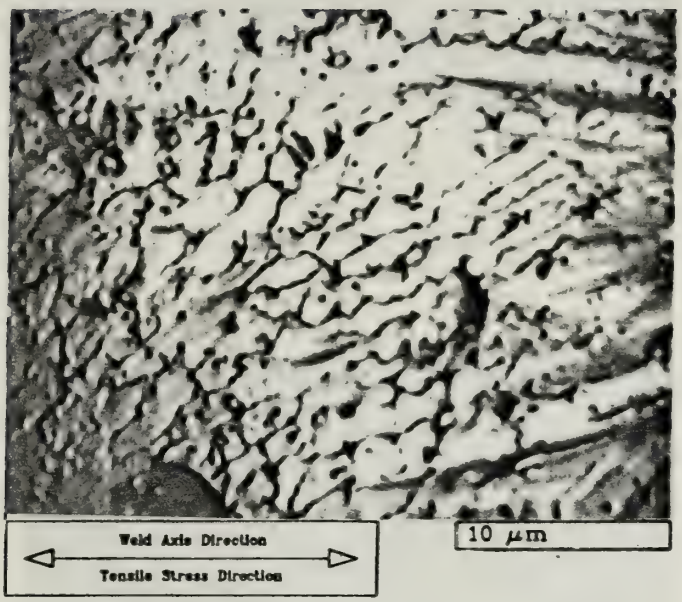

Figure 69: HY-130 Weld Metal, 40 kN Load

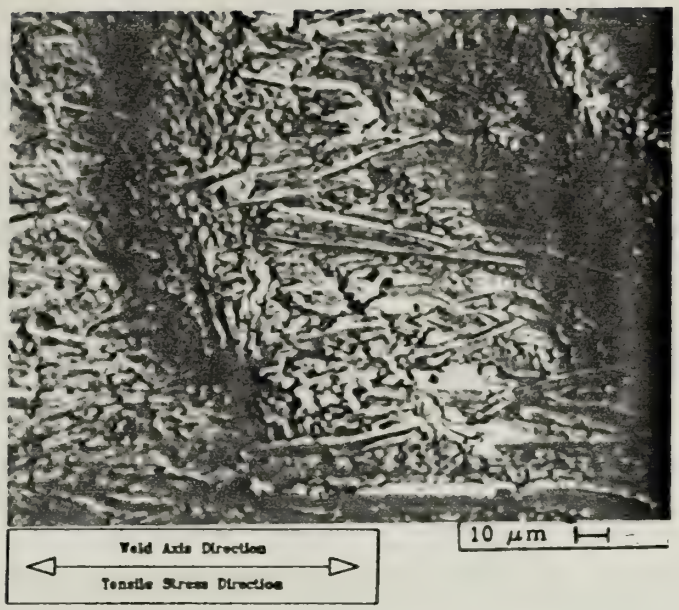

(a) 20x Objective Lens

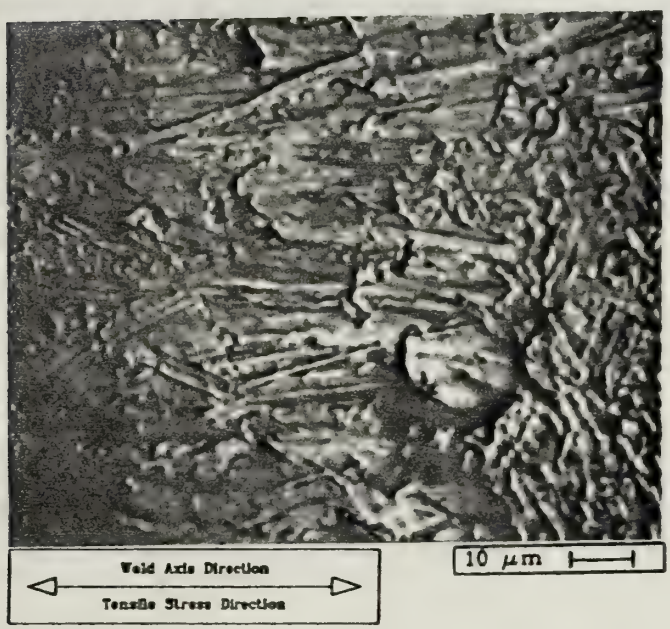

(b) 40x Objective Lens

Figure 70: HY-130 Weld Metal, 50 kN Load

References

Agapakis, J.E, Masubuchi, K. 1987, "Imaging and Machine Vision Fundamentals," Excerpts from a monograph on Computer Aided Welding Fabrication, Chapter VF, under preparation.

Agapakis, J.E, Chickering, B.R., Renwick, R.J., and Wall, M.R., 1987, "Manufacturing Applications of a Flexible Adaptive Robotic Welding System," Technical Paper, Society of Manufacturing Engineers, MS87-587

Ashby, M.F., and Jones, D.R.H., 1980, Engineering Materials 1: An Introduction to their Properties and Applications, Pergamon Press, New York

Ashby, M.F., and Jones, D.R.H., 1980, Engineering Materials 2: An Introduction to Microstructures, Processing, and Design, Pergamon Press, New York

Bass, R.A., 1989, Reduction of Residual Stress and Distortion in HY100 and HY130 High Strength Steels During Welding, Graduate Thesis for Master of Science in Naval Architecture and Marine Engineering, Massachusetts Institute of Technology, Cambridge, Massachusetts

Barnes, C.R., Ahmad, J., and M.F. Kanninen, 1985, "Dynamic Crack Propagation through Welded HY-80 Plates Under Blast Loading", Fracture Mechanics Sixteenth Symposium, ASTM STP 868, M.F. Kanninen and A.T. Hooper, Eds., American Society for Testing and Materials, Philadelphia, pp. 451-466.

Beyer, W.H., Ed, 1980, CRC Standard Mathematical Tables, 25th Edition, CRC Press, Boca Raton, Florida

Brednev, B.I. and B.S. Kasatkin, 1990, "Specific Work of Formation of Cold Crack Areas in Welding Low Alloy, High Strength Steels", Welding International (Translation), No. 4, 261-263

Brooks, J.A., and D.B. Dawson, 1979, "Microstructure - Property Relationships in High Strength Steel Welds", Weldments: Physical Metallurgy and Failure Phenomena, Lake George, N.Y. 27-30 Aug. 1978, General Electric Co., Schenectady, N.Y., pp. 305-328.

Brick, R.M., Pense, A.W., and Gordon,R.B., 1977, Structure and Properties of Engineering Materials, Fourth Edition, McGraw-Hill, New York

Chen, C., Thompson, A.W., and I.M. Bernstein, 1979,"Microstructure and Stress Corrosion Cracking of Low-Carbon Alloy Steel Welds: Part II - Fractographic Studies of Stress Corrosion Cracking of HY-130 Steel Weldments", Weldments: Physical

Metallurgy and Failure Phenomena, Lake George, N.Y., 27-30 Aug 1978, General Electric Co., Schenectady, N.Y., pp.305-328.

Chen, C., Thompson, A.W., and I.M. Bernstein, 1980, "The Correlation of Microstructure and Stress Corrosion Fracture of HY-130 Steel Weldments", Metallurgical Transactions, Vol, 11A, 1723-1730.

Clark, D.S., and Varney, W.R., 1962, Physical Metallurgy for Engineers, Second Edition, Van Nostrand, New York

Connor, L.P., editor, 1987, "Welding Technology", Welding Handbook, Eighth Edition, Volume 1, American Welding Society, Florida

Connor, L.P., editor, 1987, "Welding Processes", Welding Handbook, Eighth Edition, Volume 2, American Welding Society, Florida

Courtney, T.H., 1990, Mechanical Behavior of Materials, McGraw-Hill, New York

***

Cushing, J., 1992 (reference John's thesis)

Davidson, J.A., Konkol, P.J., and Sovak, J.F., 1989, "Assessing Fracture Toughness and Cracking Susceptibility of Steel Weldments - A Review" Welding Research Council Bulletin 345

DeGarmo, E.P.,et al., 1946, "The Effect of Weld Length Upon Residual Stresses of Unrestrained Butt Welds," Welding Journal 25 (8), Research Supplement, p. 4855-4865.

Dixon, B., 1981, "Weld Metal Solidification Cracking in Ferritic Steels - A Review", Australian Welding Journal, Summer, 23-30.

Douglas, S.A., 1992, Mechanisms of Forming Intergranular Microcracks and Microscopic Surface Discontinuities, MIT

Fraser, F.W. and E.A Metzbower, 1982, "Fractographic and Microstructural Analyses of Stress Corrosion Cracking in HY-130 Weldments", Welding Journal Research Supplement, 112S-116S.

Fujii, C.T., 1981, "Factors Influencing Stress Corrosion Cracking of High Strength Steel Weld Metals", Metallurgical Transactions, Vol. 12A, 1099-1105.

Fukagawa, M., 1982, "Study on Estimation of Crack Sensitivity of High Strength Steel Welded Joint by Weld Strain - Strain-Concentrated Type Multipass Weld Crack Test",

Fundamental and Practical Approaches to the Reliability of Welded Structures, Vol 2. Osaka, Japan, 24-26 Nov. 1982, pp.279-284.

Gifkins, R.C., 1970, Optical Microscopy of Metals, Sir Isaac Pitman and Sons, Ltd, London

Inagaki, M., 1965, "Welding Physical Metallurgy" Journal of Japan Welding Society

Kasatakin, B.S. and V.I. Brednev, 1985, "Special Features of the Mechanism by which Cold Cracks Form in Welded Joints in Low Alloy High Strength Steels", Automatic Welding,(Translation) August 1985, 5-9.

Kasatakin, B.S. and V.I. Brednev, 1985, "Special Features of the Mechanism by which Cold Cracks Form in Welded Joints in Low Alloy High Strength Steels", Automatic Welding,(Translation) August 1985, 5-9.

Kasatakin, B.S. and I.A. Kudentsov, 1979, "Research into Deformations Taking Place During the Development of Cold Cracks in Welded Joints in Low-Alloy High Strength Steel", Automatic Welding, (Translation) Vol 32, April 1979, 7-10.

Kasugi, T., Kazuo, E. and M. Ingaki, 1983, "Initiation and Propagation Behaviors of Weld Cold Crack with Fractographic Observation", Transactions of National Research Institute for Metals, Vol 25, No.2, 68-78.

Kessler, L.W., Semmens, J.E. and F. Agramonte, 1985, "Scanning Laser Acoustic Microscopy (SLAM): A New Tool for NDT", World Conference on Nondestructive Testing '85., Vol 2., Las Vegas, Nevada, 3-8 Nov 1985, American Society of Nondestructive Testing, Columbus, Ohio, pp. 995-1002.

Khripilivyi, A.A., 1988, " Special Features of Welding High Strength Multi-Layer Steels", Welding International, No. 12, 1054-1057.

Kihara, H., 1978, "Fractographic Investigation on Root Crack in the TRC Test of HY-130", Criteria for Preventing Service Failure in Welded Structures, Tokyo, Japan, 26-28 Sept 1978, The Japan Welding Society, Tokyo, Japan, pp. 263-268.

Kikuta, Y. and T. Araki, 1981, "Microscopic Redistribution Behaviours of Hydrogen and Fracture Morphology of Hydrogen-Assisted Cracks in High Strength Steel", Hydrogen Effects on Metals, I,M. Bernstein and A.W. Thompson, Eds., The Metallurgical Society of AIME, 1981, pp. 309-318.

Kutz, M., editor, 1986, Mechanical Engineers' Handbook, John Wiley & Sons, Inc., New York

Mase, G.E., 1970, "Theory and Problems of Continuum Mechanics", Schaum's Outline Series, McGraw-Hill, Inc., New York

Masubuchi, K., 1980, Analysis of Welded Structures, Pergamon Press, Oxford/New York

Masubuchi, K., and H. Yajima, 1986, "Fracture Characteristics of Weldments", Encyclopedia of Material Science and Engineering, Vol. 3, Headington Hill Hall, Oxford, pp.1847-1852.

Makhnenko, V.I. and T.G. Ryabuchuk, 1986, "Calculations to Evaluate the Degree to which the Metal at the Tip of a Crack Developing in the Heat-Affected Zone is Hydrogen Charged", Automatic Welding, (Translation), March 1986, 9-12.

Matsuda, F., 1985, "Effect of Oxygen Content on Cold Cracking Susceptibility in Weld Metal of High Strength Steel", Transactions of the Japanese Welding Research Institute, Vol. 14, No. 2, 335-342.

McClintock, F.A., and Argon, A.S., 1966, Mechanical Behavior of Materials, Addison-Wesley Publishing Co., Reading, Massachusetts

McMahon, C.J., 1981, "Effects of Hydrogen on Plastic Flow and Fracture in Iron and Steel", Hydrogen Effects on Metals, I,M. Bernstein and A.W. Thompson, Eds., The Metallurgical Society of AIME, pp. 219-233.

McPherson, R. and R.I. Presser, 1978, "The Mechanism of Reheat Cracking", Criteria for Preventing Service Failure in Welded Structures, Tokyo, Japan, 26-28 Sept 1978, The Japan Welding Society, Tokyo, Japan, pp.427-432.

Miller, K.J., 1991, "Metal Fatigue - Past, Current, and Future," Proceedings of the Institution of Mechanical Engineers, Twenty-seventh John Player Lecture

Montemarano, T.W., et al, 1986, "High Strength Low Alloy Steels in Naval Construction", Journal of Ship Production, Vol. 2, No. 3, 145-162

Nippes, E.F. and D.J. Xiong, 1988, "Investigation of Hydrogen-Assisted Cracking in FCA Welds on HY-80 Steel", Welding Journal Research Supplement, June 1988, 131S-137S.

Naval Sea Systems Command, 1990, Military Standard 1688A(SH), Fabrication, Welding, and Inspection of Hy-80/100 Submarine Applications, United States Navy, Washington, D.C.

Oberg, E., and Jones, F.D., 1968, Machinery's Handbook, Eighteenth Edition, Industrial Press, New York

Phillips, A.L., editor, 1960, Fundamentals of Welding Metallurgy, American Welding Society, New York (Same as Welding Handbook, Fifth Edition, Section I)

Popov, E., 1968, Introduction to Mechanics of Solids, Prentice Hall, New Jersey

Porter, D.A., and Easterling, K.E., 1981, Phase Transformations in Metals and Alloys, Chapman and Hall, New York

Shames, I.H., 1975, Introduction to Solid Mechanics, Second Edition, Prentice Hall, New Jersey

Sterenbogen, Yu A. and G.V. Burski, 1987, "A Method of Evaluating Cold Cracking Resistance of the Heat Affected Zone of Welded Joints in High Strength Steels". Welding International,(Translation), No. 12, 1106-1109.

Thompson, A.W. and I.M. Bernstein, 1981, "Microstructure and Hydrogen Embrittlement", Hydrogen Effects on Metals, I.M. Bernstein and A.W. Thompson, Eds., The Metallurgical Society of AIME, pp. 291-308.

Urednicek, M., 1978, " Fracture Mechanics Approach to Hydrogen-Induced Embrittlement of High Strength Steels", Metallurgical Society of CIM Annual Volume, Canadian Institute of Mining and Metallurgy, Montreal, Canada, pp.63-67.

Vander Voort, G.F., 1986, Applied Metallography, Van Nostrand Reinhold Company, New York

Wong, R.J., 1988, "The Effect Of Weld Metal Diffusible Hydrogen on the Cracking Susceptibility of HY-80 Steel", Hydrogen Embrittlement: Prevention and Control, ASTM STP 962, L. Raymond, ED., American Society for Testing and Materials, Philadelphia, pp. 274-286.

You, C.P., Hippsley, C.A. and J.F Knott, 1984, " Stress Relief Cracking Phenomena in High Strength Structural Steel", Metal Science, Vol 18, August 1984, 387-394.

Zanis, C.A., and P.W Holsberg, 1982, "Stress Corrosion Cracking in HY Steel Weldments", Current Solutions to Hydrogen Problems in Steels, Washington, D.C., 1-5 Nov 1982, American Society for Metals, Metals Park, Ohio, pp. 319-327.

Zanis, C.A., 1978, "Subcritical Cracking in High Strength Steel Weldments-A Materials Approach", SAMPE Quarterly, January 1978, 8-12.

Zhiming, Z., 1982, ""The Hydrogen Induced Cracking and Stress Corrosion Cracking in Welded Joints of Ultra High Strength Steel", Fundamental and Practical Approaches to the Reliability of Welded Structures, Vol 2. Osaka, Japan, 24-26 Nov. 1982, pp. 437-442.

Appendix A

Non-Destructive Testing Techniques, An Overview

Non-Destructive Testing, NDT, is a general term that refers to any test method that may be applied to a specimen without reducing its ability to perform its intended function.

Six common NDT techniques were predominant by the end of World War II: eddy current testing, ET, magnetic particle testing, MT, liquid dye penetrant testing, PT, radiographic testing, RT, ultrasonic testing, UT, and visual testing, VT. These methods remain the most common to this day, however, most of these test methods have been highly refined as technology advanced. Further, new developments and new requirements, especially in the aerospace industry, have led to new NDT testing methods such as strain testing, high sensitivity leak detection, thermal testing, infrared testing, and acoustical emission testing. Discussion will remain limited to the first six which predominate in the testing of welded structures.

Eddy current testing is used to detect surface and near-surface discontinuities, cracks, voids, inclusions, as well as variations in thickness and metal condition. Hardness and heat treatment condition may be determined for alloys whose characteristics are well known. Eddy current testing may be performed on both ferromagnetic and non-ferromagnetic metals.

When an electromagnetic coil, energized by alternating current, is placed near a metal sample, eddy currents are induced in the piece. Thus, these eddy currents are circulating alternating electrical currents in a conducting material induced by an adjacent alternating magnetic field. A crack or other discontinuity in the material disrupts the eddy current flow, causing a back scattering of electron flow. The induced eddy currents are strongest near the surface of the test specimen and decay exponentially with depth.

The standard depth of penetration is defined as the depth below the surface where the density of the eddy current is 37% of the density at the surface. Penetration varies inversely with the electrical conductivity and magnetic permeability of the metal and with the frequency of the alternating eddy currents. A specimen must have a thickness of at least two to three times the standard depth in order to avoid thickness effects.

The disturbances in the eddy current flow are detected using either the exciting coil, also termed the probe, or a second coil, termed a sensing or pickup coil. As the probe is moved across the specimen, the variances in the induced field can be interpreted by an impedance analysis, phase analysis, or a modulation analysis, thus, any discontinuity that significantly alters the flow of eddy currents can be detected. The discontinuities that are readily detectable include seams, laps, cracks, slivers, pits, open welds, oxides, and pinholes. With special probes, discontinuities as small as 0.135×10^{-3} m (6×10^{-5} inches) may be detected at or near the specimen surface. When discontinuities of the same size are located at progressively greater depths, it becomes increasingly difficult to detect them. Orientation of the flaw can be important. Cracks or other planar discontinuities must be nearly perpendicular to the eddy current flow in order to be detected.

MT

Magnetic particle testing is a non-destructive test method for detecting flaws at or near the surface of ferromagnetic materials. This method is useful for detecting of surface or sub-surface flaws, cracks, porosity, non-metallic inclusions, and weld defects.

When a magnetic field is established in a piece of ferromagnetic material containing one or more discontinuities in the path of the magnetic flux, minute poles are established within the discontinuities. The discontinuities are visualized by applying magnetic

particles, commonly iron powder, to the specimen surface. The powder may be dry or suspended in an emulsion. The poles established about the discontinuities have a stronger attraction for the magnetic particles than the surrounding surface of the material. Since a crack or other flaw disrupts the even flow of the lines of magnetic force through a specimen, the anomalies are located by the distinctive patterns formed by the iron powder. This effect is optimized when the magnetizing current flows parallel to the principal direction of a flaw. Through elementary electromagnetic theory, the magnetic field will be perpendicular to the direction of the flaw (right hand rule).

The surface of the specimen must be free of dirt, grease, lint, or other contaminants that might prevent the magnetic particles from moving freely.

The specimen may be magnetized in a number of ways which include alternating current (AC) and direct current (DC) techniques. AC is best for finding surface discontinuities; filtered or pulsed DC works well for subsurface discontinuities. Typically, optimum current levels, and therefore the optimum magnetic field strengths, are found empirically. All materials that are inspected using MT will retain some residual magnetism. If necessary, this residual effect may be eliminated by degaussing techniques, typically using a 60 Hz AC power.

Liquid penetrant testing, or dye penetrant testing has become very popular in industry because it is widely applicable. Unlike MT, The PT technique is not limited to ferrous materials. PT locates defects that are open to the surface in solid, non-porous materials by detecting highly visible liquids that are held by the flaws through capillary action. Thus, PT is used to detect porosity, laps, cold shuts, lack of weld bond, and cracks as long as they are open to the surface. This test can be considered an extension of visual testing, VT, discussed below.

The penetrant is a colored or fluorescent liquid with the ability to effectively wet the surface of an object, form a relatively uniform coating, and become drawn into cracks, cavities, and other cavities that are open to the surface. The penetrant is washed off of the surface with the aid of an emulsifier, thereby removing all excess deposits. A developer is then applied to the surface. The developer, talc powder being an example, draws traces of penetrant from the cracks and cavities, and yields a high contrast indication of the anomaly. The colored penetrant, usually red, forms highly visible indications; the fluorescent penetrant is visualized by using an ultra violet light source.

The surface of the material to be inspected must be clean and dry. Sandblasted, shotblasted, or peened surfaces are not recommended since these techniques can hide small openings. After inspection, the surface must be cleaned since the PT chemical

system may interfere with subsequent operations such as plating, etching, and painting. There is evidence that improper cleaning may lead to corrosion fatigue susceptibility.

RT

Radiographic testing, RT, employs X-rays or gamma rays to penetrate an object. Discontinuities within the volume of material that comprise the object impede the radiation less than the homogenous medium. Therefore, an image may be constructed on a recording or viewing medium. Usually, photographic film or sensitized paper is used to obtain permanent records of the test[1]. In this way, RT is used to find internal flaws and defects, cracks, seams, porosity, holes, and inclusions. It can also be used to determine thickness variations and check assemblies.

UT

UT is used to detect internal defects, cracks, lack of bond, laminations, inclusions, porosity, and grain structure. It can also be used for finding thickness variations and laminar flaws.

---

[1]Recording devices also include florescent screens and various types of electronic radiation detectors.

In this non-destructive method, beams of high frequency sound waves are introduced into a test object to detect and locate surface and internal discontinuities. The sound wave frequencies used in weld inspection are between 1 and 6 Mhz. Most weld testing is performed at 2.25 MHz. Higher frequencies, near 5 Mhz, are used in locating and evaluating discontinuities in thin wall weldments. The sound beam is directed into an object on a predictable path, and is reflected at interfaces or other interruptions in material continuity. The reflected beam is analyzed to define the presence and locations of discontinuities.

Principal advantages of UT compared to other NDT methods for weldments include:

Detection of discontinuities in thick sections.

A relative high sensitivity to small discontinuities.

Depth, position, and size of discontinuities can be determined.

Inspection can be performed from one surface in some cases.

The equipment is portable.

The equipment and procedure is nonhazardous to personnel or other equipment.

Ultrasonic testing has the following disadvantages:

The setup and operation require trained and experienced personnel.

Rough or highly convoluted surfaces cannot be adequately inspected.

Discontinuities at the surface are difficult to detect.

A couplant is needed between the transducer and the piece being inspected.

Reference standards are required to calibrate the equipment.

VT

Visual testing is the most basic form of non-destructive testing. For the most part, VT consists of simply looking at the welded area. Gages, magnifying glasses, and other tools are used in specific applications.

This method is fast and inexpensive, not normally requiring special equipment. In steels, it only detects flaws at the surface.

Table A-1

Non-Destructive Inspection Techniques

Method	Major Advantages	Major Limitations and Disadvantages
ET	- 0.135×10^{-3} m discontinuities are detectable - Instantaneous detection of continuities - Mechanical contact not usually required - Adaptable to high speed scanning and automatic feedback - Can detect subsurface flaws	- depth limit varies with material properties - Ferromagnetic materials make interpretation difficult - Moderate capital investment in equipment and training - Detection is largely operator dependant
MT	- A relatively simple test - Highly sensitive to small crack-like flaws - Can detect subsurface flaws - Heat treatment of specimen does not affect results - Can be automated - Relatively inexpensive capital investment	- Ferromagnetic materials only - Surface must be clean and relatively smooth - Detection is largely operator dependent for shipboard inspections - Records are limited to photographs and notations
PT	- A simple test - Not limited to ferrous materials - Inexpensive - Covers large areas	- No porous materials - Only detects flaws open to the surface - Cannot be used in very hot or very cold environments - Surface must be clean and dry - Detection is largely operator dependent - Records are limited to photographs and notations

Table A-1

Non-Destructive Inspection Techniques

RT	- Inspects the volume of a specimen - Not limited to material type, both metallic and non-metallic - Permanent record produced - Covers large areas	- Radiation hazard to personnel - Results are not immediate - Expensive. Large capital investment in equipment and training - Detection is largely operator dependent
UT	- Not limited to ferrous materials - Detects flaws at substantial depths, revealing the internal nature of the material - Can detect minute flaws - Accurate sizing and location of defects - May be automated	- Geometry of specimen may impede testing - Moderate capital investment in equipment and training - Detection is largely operator dependent - Requires a direct mechanical coupling to the specimen - Covers small areas - Attenuation in coarse grained materials
VT	- Inexpensive - Covers large areas rapidly	- Detection is largely operator dependent - Only detects flaws visible on the surface

Appendix B

The Confocal He-Ne Laser Microscope.

Overview

The scanning confocal laser microscope was developed by the Lasertec Corporation.[2] The confocal imaging system uses the coherent light of a laser and conventional light microscope optics, combining them with a beam splitter and photodetector array. This permits rapid identification of specific areas of a large image that are in focus. As the microscope is swept through the range of focus positions necessary to visualize all levels of a surface, an image processor collects sequential in-focus areas. A full picture is constructed in much the same way as a jigsaw puzzle picture: each individual piece is an in-focus image assembled to form a large image from which meaningful information may be extracted.

The instrument consists of a conventional optical microscope combined with a scanning laser, a confocal imaging system, and an image processing unit. The laser microscope

---

[2] Lasertec Corporation, 4-10-4 Tsunashimahigashi Kohoku-ku, Yokahama 223 Japan. Tel: (045) 544-4111;

Lasertec USA Inc., 2001 Gateway Place Suite 130. San Jose. California 95110 U.S.A. Tel: (408) 437-1430

system is depicted in Figures B-1 and B-2. The image processor sends an output signal to a 12 inch video monitor where the image is displayed. The instrument is also equipped with a Z-axis controller which serves to move the microscope up and down over a specimen stage which can also be adjusted in the X- and Y- directions.

the Confocal Imaging System

The confocal imaging system provides high resolution imaging, 0.25 μm with Nikon Optiphot 100x 0.95NA objective lens, making it very quick and easy for the image processing unit to determine when any given point is in focus. A diagram of the confocal imaging system is shown in Figure B-1. The laser beam is focussed onto the surface of the specimen and a portion of the light is reflected back into the objective lens. These reflected rays are then deflected by a beam splitter and refocussed onto the detector through a pinhole. When the surface is out of focus, instead of a sharply focussed point, the reflected rays form a cone of light at the pinhole opening. Therefore, less light reaches the detector when an image is out of focus; peak light intensities coincide with areas that are in focus. The processing unit uses the peaks at each point in the field to construct sharply focussed images, eliminating the much more complicated job of ascertaining whether an image is blurry. The image processing unit supports the unique capabilities of the instrument which include:

Extended focus

Lateral surface measurements

Surface profilometry

Optics and Image Magnification

The heart of the system is the optical microscope which has the capacity to mount five objective lenses on its rotating turret. Objective lenses with magnifications from 1x to 200X and various numerical apertures are available from Nikon. The image displayed on the television monitor is approximately 60 times larger than the image produced within the optical microscope, therefore, a multiplicative factor of 60 is applied to the objective lens power to obtain the magnification of the displayed image.

$$Displayed\ Magnification = 60\ [Objective\ Lens\ Power] \quad (1)$$

Table B-1

Laser Microscope Display Statistics

Objective Lens	Magnification on 12" Monitor	Field of View (μm)	Scanning Line Density (μm/line)
10. x	600. x	410 x 325	0.68
20. x	1200. x	205 x 163	0.34
40. x	2400. x	125 x 82	0.17
50. x	3000. x	82 x 65	0.14
80. x	4800. x	51 x 41	0.08
100. x	6000. x	41 x 32	0.07

The scanning laser consists of a fixed He-Ne laser source radiating at 6328 Å, combined with an acousto-optical derive (AOD) and a galvanometer mirror. The AOD is accomplishes the vertical (Y-axis) scanning. The galvanometer mirror deflects the laser beam so it scans the specimen surface vertically (in the direction of the X-axis). The laser microscope achieves video rate scanning, 1/30 second to complete one scan and obtain an image.

Main Features and Advantages of the System:

The operating parameters and specifications for the system are detailed in Table B-2. The principal features of the instrument include the following:

Extended Focus:

The extended focus feature enables the processing unit to compose an image with virtually unlimited depth of field. This is a great advantage when observing objects that have 3-dimensional surface features that cannot be accommodated by the thin range of focus of conventional optical systems, a particular problem at higher magnifications. With the extended focus capabilities offered by the confocal optics and image processor, the thin planes of focus are stored in memory as the processor identifies the peak light intensities for each pixel. The final image is a mosaic of the stored peak signals, thus a large focussed image is displayed.

Lateral Surface Measurements:

With the monitor in Measurement Screen Mode, dashed vertical cursor lines can be manually directed on the video monitor to measure distances down to 0.25 μm.

Surface Profilometry:

The profile of the surface, analogous to the edge of a cross-section, may be determined by using surface profilometry. Differences in elevation and slopes can

be observed and quantified. With the processor in the Measurement Screen Mode, the solid horizontal line is positioned along the region where the surface profile is desired. The Z-axis controller is then used to move the stage through the focal range for the area of interest. This may be performed manually or automatically. The image processor coordinates the peak intensities with the z-coordinate of the microscope. A smoothing algorithm is applied to the raw data, and an altitude profile is constructed for the selected region. Differences in elevation can then be measured through the controls of the processor unit.

High-resolution, high-magnification image by confocal optics

Critical dimension measurement (CD measurement) function. Repeatability: 3σ = 0.03 μm

Real-time image at television rates. By use of an acoustic-optical scanner for scanning the laser beam, a sample can be observed in real time, facilitating the search for and focusing of the sample, as well as observation of a moving sample.

Pretreatment of the sample is not required, however the sample must be clean and dry.

Low intensity monochromatic illumination minimizes thermal damage to heat sensitive specimens.

Observation of light-emitting objects.

Slow scan function:

This feature allows observation of samples with low reflection factors. By delaying the scan speed of the laser beam, the storage time of the optical sensor is lengthened. As a result, observation of a low reflection sample becomes possible. The sensitivity is proportional to the slow scan rate. When using the slow scan function, the use of frame memory is necessary. Eleven slow scan rates are available for selection.

Gamma Function:

The correlation between the amount of light input to the optical sensor and the video signal output is adjustable between three gamma function profiles. Normally, a linear function is used for viewing. Here, γ_{hv} = constant. With a decreasing gamma function slope, γ_{hv} = negative, the darker portions of the image are lightened, and the brighter portions of the image are darkened. This serves to improve the contrast of the darker areas which result from lower relative reflectivity. Using an increasing gamma function slope, γ_{hv} = positive, lighter portions of the image are brightened more, and darker portions are darkened

further, thereby increasing contrast. This position is used to study the bright portions of images.

Optimal signal source for various image processing capabilities

Output Signal Recording:

The video signal output can be recorded by connecting it to a standard VCR. The video signal output may also be connected to an image processing unit to enhance visualization.

Table B-2

Laser Microscope Operating Parameters and Specifications
(data from Lasertec)

Category	Parameter and Specification	
Make and Model	Lasertec Corporation Model 1LM11 Scanning Laser Microscope	
Resolution	0.25 μm with Nikon Optiphot 100x 0.95NA objective lens	
He-Ne Laser Light Source	Wavelength	6328 Å
	Output at laser body	1.50 mW
	Output at exit if 5x 0.1NA objective lens	0.14 mW
Scanning Speed	Horizontal	15,730 Hz
	Vertical	60 Hz
	Interlace	2 : 1
Signal Output	Video signal output	1 Vp-p (75 Ω at terminal)
	Synchronization signal output	1 Vp-p (negative, 75 Ω at terminal)
	Composite (video plus synchronous signal)	1 Vp-p (75 Ω at terminal)
Slow Scan Rates	2, 4, 8, 16, 32, 64, 128, 256, 512, 1024, 2048	
Frame Memory	1,137(H) x 525(Y) x 8 bits	
Critical Dimension Measurement	Minimum measurement unit	0.01 μm
	Dimensional measurement repeatability	± 0.03 μm (3σ)
Dimensions and Weight	Camera Head	105 x 310 x 83 mm; 5.0 kg
	Control Unit	420 x 105 x 490 mm; 10.0 kg
	Base	
	Monitor (B&W)	302 x 305 x 336 mm; 9.8 kg
	System Footprint	
Power	110/115 VAC 50/60 Hz	

Table B-2

Laser Microscope Operating Parameters and Specifications
(data from Lasertec)

Category	Parameter and Specification	
Ambient Operating Environment	Temperature	5 to 40 ℃
	Relative humidity	80% or less

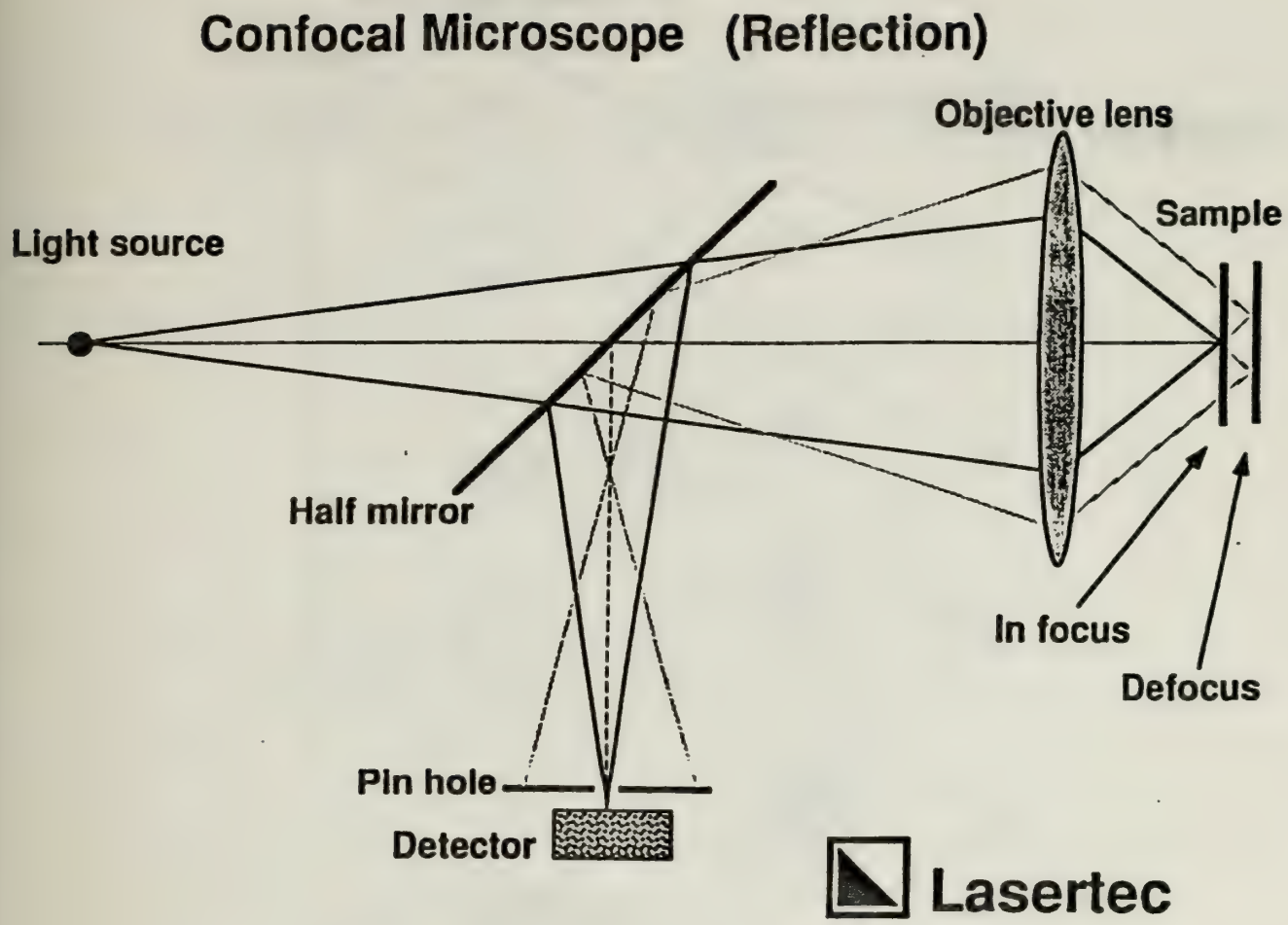

Figure B-1: Confocal Imaging System

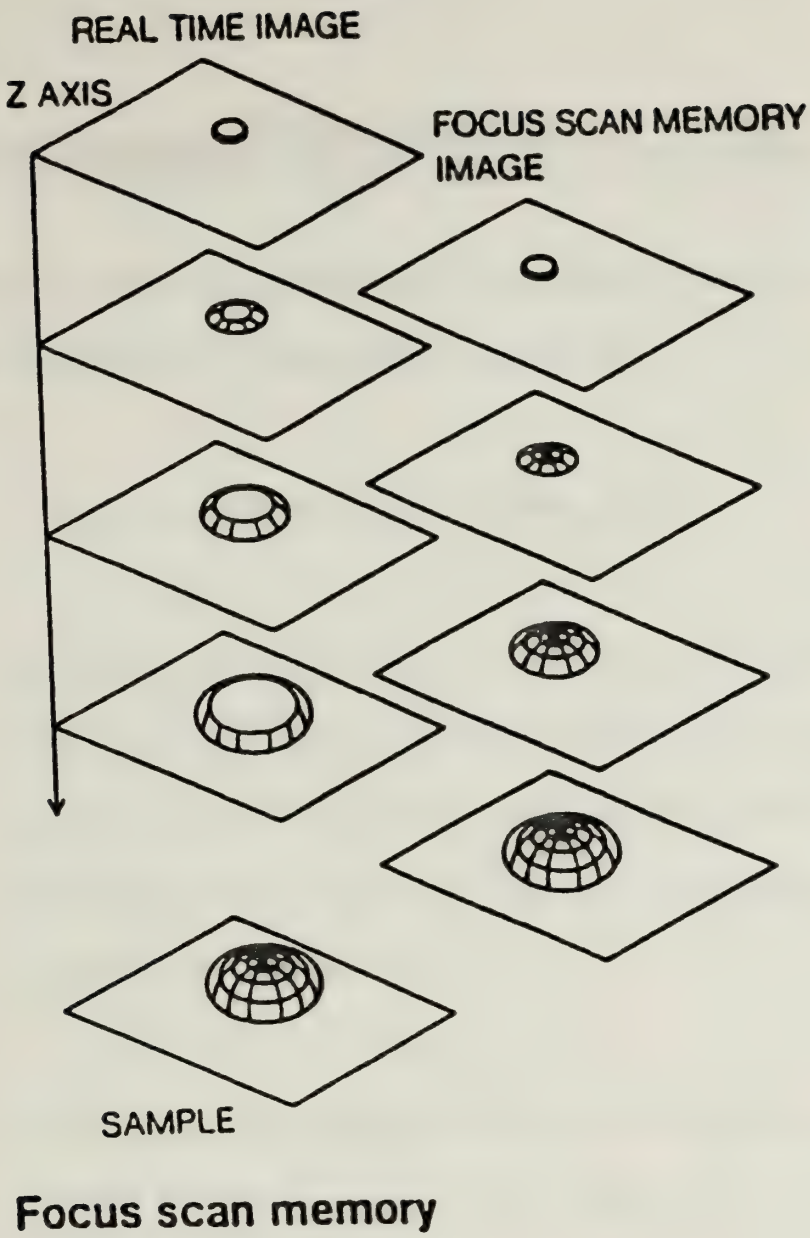

Figure B-2: Focus Scan Memory

Appendix C

Replication Technique

The following instructions were obtained from those supplied with the replicating kit (Catalog Number 12000) from Ladd Research Industries, Inc.[3]

1. Cut off an appropriate length of replicating tape.

2. Brush a drop or two of solution on the surface that is to be replicated. The concentration of the replicating solution has been determined from Ladd's experimental data over a long period of time. If for some reason thinning is desired, add acetone. This solution should not be used on painted or lacquered surfaces.

3. Press a 1" piece of tape firmly on the solution coated area, being careful to apply the tape so as to squeeze out air bubbles.

4. Allow tape to dry thoroughly before stripping it off the specimen. Usually 1 through 5 minutes is sufficient time for drying. On rough surfaces

[3]Ladd Research Industries, Inc., P.O. Box 1005, Burlington, VT 05402

where considerable solution has to be used, drying may take 15 to 30 minutes.

5. Strip the replica from the surface. This replica will generally show dirt from the surface. It is best to discard this replica and repeat steps 1 through 5 unless the purpose is to study the original material on the surface.

6. Fasten the edges of the replica to a glass microscope slide using scotch tape. (Triple M is preferred). Place in a vacuum evaporator and shadow with chrome, platinum-palladium, or platinum-carbon. For light microscopy, Ladd recommends shadowing with aluminum.

   In this investigation, the replicas were shadowed with gold. This enabled the replica to be viewed using both the laser microscope as well as the scanning electron microscope.

Appendix D

Literature Review

Introduction

A literature review was conducted to establish the current mechanism hypotheses causing microcracking and microscopic surface discontinuities in welds and the possible methods for reducing the occurrence of these defects.

The review was conducted using metallurgical and materials publication databases. Key words used for the review of cracking mechanisms included: welds, cracking, high strength, residual, thermal, stress, and hydrogen. The search was limited to references published within the last 15 years. Over 300 references were found. The titles were reviewed and 93 abstracts were obtained. From these abstracts, a total of 29 articles were pulled for review. Roughly 80% of the articles were reviewed in detail, with an emphasis on the introductory and concluding paragraphs. The remaining 20% of the review was extracted from the abstracts.

A separate survey of the literature for details on laser microscopy used the instrumentation database. The key words used were laser, laser microscopy, and microscopy. Only a handful of articles were found, all dealing with the scanning laser

acoustic microscope (SLAM). Only one of these articles was reviewed. There were no references found that just describe the laser microscope or its use. The extent of this literature review was primarily limited to cracking and cracking mechanisms in high strength steels due to the shear volume of material available on the general subject. As it is, this review is far from being comprehensive.

High strength steels are of interest due to the known high sensitivity of these steels to cracking and since they are being used more frequently today in the fabrication of high technology welded structures.

Portions of this discussion were made possible through the efforts of Stephanie Douglas.

Laser Microscopy:

Kessler (1985) reviewed the scanning acoustic laser microscope (SLAM) as a new tool for NDT. The SLAM technique uses high frequency sound coupled with rapid real time imaging to locate, size and differentiate flaws found in a variety of materials, including metals, ceramics, polymers, and composites. The operating frequency is extended out to several hundred MHz, making it possible to achieve very high resolution and obtain images of optically opaque or translucent materials. This acoustic microscope makes use

of a focused laser beam which acts as a small point-to-point ultrasonic sensor or receiving transducer. The laser can scan a sample area at the rate of 30 images per second.

The acoustic capability of this microscope allows for the imaging of internal structures such as porosity, cracks, voids, and disbonds of adhesively bonded joints. It can also detect changes in the elasticity of a material. The acoustic energy is brought to the sample through the microscope stage. The are various stages in order to operate at different frequencies. Higher frequencies are used to obtain better resolution and lower frequencies are used to obtain deeper penetration. The ultrasound is brought from the transducer (in the microscope stage) to the sample through a liquid.

The advantages of the SLAM technique include:

1) nondestructive

2) rapid high resolution imaging

3) defect location and characterization

4) many complex shapes can be accommodated

5) ideal for bond evaluation.

The disadvantages of the SLAM technique include:

1) immersion in fluid for ultrasonic coupling

2) excessive porosity or structure can mask flaws.

Hot Cracking:

Dixon (1981) reviewed weld metal solidification cracking in ferritic steels, including descriptions of its various forms, the theories that explain their formation, an examination of the effect of composition on the sensitivity to cracking and the effect of welding parameters on cracking. Weld metal solidification cracking is prevalent in nickel and aluminum based alloys, and austenitic stainless steels. Its presence in ferritic steels varies widely but can be a serious problem in high strength quenched and tempered steels. It can also be exacerbated by high heat input welding processes on thick sections that have highly restrained joints.

Solidification cracking is characteristically interdendritic. Cracks are commonly identified by their location in the weld bead. Flare cracks are those found near the fusion boundary, centerline cracks lie along the weld centerline normally below the surface, and crater cracks are found at the end of the weld run. Cracking is particularly prevalent at or near the surface of a multipass weld where the localized strains are severe. Cracks form at temperatures approaching the solidus of the weld metal when low melting point constituents segregate to dendrite boundaries. The thermal shrinkage (2-6%) associated with the solidification process imposes strains across the liquid films at the dendrite interfaces, causing them to rupture.

The various forms of solidification cracking described include segregation cracking in the weld metal, liquation cracking in the HAZ, liquation cracking in the weld metal of multipass welds, and ductility tip cracking in the weld metal and HAZ.

Dixon lists as the theories most commonly accepted for solidification cracking, the shrinkage-brittleness theory, strain theory, Borland's generalized theory, and Prokhorov's theory.

The solidification process is thought to be comprised of four distinct stages. These stages are primary dendrite formation, dendrite interlocking, grain boundary development, and solidification. (Dixon, 1981) The primary dendrite formation phase allows solid and liquid phases present to be capable of relative movement. In the dendrite interlocking phase, the liquid phase is capable of relative movement between dendrite boundaries. When the grain boundaries begin to develop, the solid crystals no longer allow the relative movement of the liquid phase. This stage is associated with the critical solidification range (CSR). Shrinkage strains begin to develop and if these localized strains exceed some critical value, cracking will occur. Finally in the fourth stage, the liquid has solidified completely.

The strain theory, originally proposed by Pellini, suggests that cracks cannot occur during the "mushy " stage of solidification, since shrinkage strains are uniformly distributed. Cracking is caused by the presence of liquid films between solidification grains.

The Borland theory suggests that a wide freezing range is not sufficient for cracking to occur. The liquid must also be distributed over the grain surfaces in such a way that high strains have the opportunity to be built up on the narrow solid bridges connecting adjacent grains. If the liquid is confined to the interstices at grain triple points, the grains have a greater surface area over which they can form strong bonds that are capable of withstanding high welding strains.

Prokhorov's theory relates temperature and strain rates within the solidifying metal to crack susceptibility range (CSR). The temperature over which cracking occurs is the brittle temperature range (BTR). This range is the same as the CSR except that it extends below the solidus. Within the BTR, most of the strains are absorbed by local distortion of ductile intergranular phases. However, when the strain rate is too rapid the grain boundary films can rupture and form cracks. (Dixon, 1981)

The individual elements that affect cracking include carbon, sulphur, phosphorous, manganese, oxygen, silicon, aluminum, niobium, cerium, copper titanium, and boron. In ferritic welds, carbon, sulphur, phosphorous, niobium, copper, boron, and nickel are considered crack promoters. Manganese, oxygen, cerium, and chromium are regarded as crack inhibitors. There is disagreement as to the effect of silicon, aluminum, and titanium.

The welding parameters that affect crack sensitivity include surface profile, travel speed, arc oscillation, powdered filler metal, flux, plate strength and thickness, preheat, and joint preparation. The parameters that raise the level of strain across the solidification front increase the sensitivity to cracking. Concave surface profiles, high weld depth/width ratios, increased plate thickness, unsatisfactory joint preparation, and localized preheat treatments tend to promote cracking. Cracking may be reduced by controlling the solidification structure. This can be accomplished by using shallow joint profiles, arc oscillation or pulsation, and multipass welding.

McPherson (1978) discusses the mechanism of reheat cracking in low alloy steels (Ni-Cr-Mo-V). It suggests that the major contribution to reheat cracking arises from prior austenite grain boundary embrittlement, at 600°C, associated with the segregation of traces of boron in the presence of aluminum.

Cracking occurs under the action of residual stresses in the HAZ within the temperature range of 550-650°C, after this region has been heated above 1100°C. Susceptibility of this kind of cracking is composition-dependent and steels containing vanadium are a particular problem. The mechanism of reheat cracking was originally thought to be caused by alloy carbides being taken into solution during austenization in the weld HAZ. The carbides such as V_4C_3 and Mo_2C, precipitate out to strengthen the grain interiors. This leads to the constraint of deformation in the grain boundaries until the stress exceeds the available grain boundary ductility. Other factors are now considered to also be

involved. It is suggested that trace elements may influence the grain boundary properties. Impurities usually regarded as deleterious to ductility are Al, Cu, B, P, S, As, Sb, and Sn. Steels doped with Al and Cu showed some evidence of embrittlement while the steels doped with boron to levels as low as 3 ppm in the presence of aluminum showed evidence of severe embrittlement. The other impurities showed no apparent effect. Factors such as welding procedures and joint geometry which determine the residual stress level and distribution in a weldment may also influence reheat cracking susceptibility.

Cold Cracking:

Brednev (1990) examines the dependence of critical specific work values used for local deformation on form factors which determine the cold cracking susceptibility of metal. Chemical composition and diffusible hydrogen content cooling conditions influence the susceptibility. It suggests a criterion, A_{2cr}, which characterizes the critical energy capacity of local plastic deformation in delayed fracture of a welded joint, considering both force and deformation. A_{2cr} is defined as the product of the critical stress level and the critical local plastic strain.

There is a positive effect of preheating on the cold cracking resistance is reflected mainly in a reduction of the degree of localization of microplastic strains, their deconcentration

and an increase of the basis over which microplastic yielding takes place. This increases the amount of energy used for local plastic deformation prior to the formation of a failure zone. Preheat causes a reduction in cooling rate. The reduction in cooling rate increases the critical energy capacity of local plastic deformation. Forced cooling increases the critical stresses but does not support the development of microplastic strains and stress relaxation, and only delays the fracture process.

Kasatkin (1979) investigates the macro-mechanism of the formation of cold cracks during the welding of low alloy high strength steels and analyzes the kinetics of the stresses and strains involved. The development of residual stresses is accompanied by relaxation processes whose intensity depends on the relationship between the centers of relaxation and macro defects developing in high strength metal. This is a result of plastic deformation and the diffusion of hydrogen at temperatures between 150 and 500°C. New cold crack nuclei are not likely to initiate at temperatures below 50°C, but the development of existing cracks may be accelerated, depending on the selective localization of deformations at temperatures of 500-150°C during cooling.

Kasatkin (1985) discusses special features of the mechanism of cold cracking in welded joints HSLA steels in relation to cooling conditions and amount of diffusible[4] hydrogen in the weld.

[4] The term diffusible hydrogen is commonly used in the literature to describe atomic hydrogen that is capable of "diffusing" through the lattice structure of the metal.

There are three reasons for the development of cold cracks:

1) Martensitic structure

2) Diffusible hydrogen in the weld and HAZ

3) High tensile stresses caused by nonuniform cooling during welding.

It is necessary to analyze the special features of the mechanism of cracking beyond these factors by investigating the kinetics of the plastic deformation which can result in the initiation of microcrack nuclei and their development to a critical size. The high rate at which plastic deformation takes place in the unsteady temperature field during welding plays a decisive role in the formation of the structure, the distribution of diffusible hydrogen, and consequently the formation of cold cracks. Plastic deformation develops least when welds are cooled rapidly after welding where conditions provide higher cooling rates from the martensitic transformation temperature. As the cooling rate is reduced, plastic deformation develops while cracks are being originated. The high rate of movements during the initial period after loading of preheated specimens, and the change associated with this in the accumulated energy, the structure and distribution of diffusible hydrogen, have a substantial effect on the deformation process and breakdown of the metal.

It is shown through the time-movement relationships presented that the process of the development of cold cracks is linked with creep in unsteady conditions in welded joints. The amount of time after cooling has a great effect on the likelihood of microcracks forming and developing to failure. The magnitude of the stresses necessary to activate the process of intergranular slip, which is a necessary condition for microcracking, is also important. The likelihood of slip occurring along grain boundaries is governed by the grain size and the grain structure.

The resistance to delayed breakdown decreases at cooling rates below 22-24°C/sec. The authors suggest that this phenomenon is associated with the formation of finer grained martensite in the HAZ during rapid cooling and that hydrogen diffusion is impeded during the rapid cooling phase. The presence of a fine grained martensitic structure reduces the intensity with which microplastic deformations are localized, making it more difficult for sub-microcracks to form.

The activation of intergranular deformation under load during cooling is made easier by the active development of plastic deformation caused by heating and deformation cycles during welding. This causes the structure to be unstable, particularly during the martensitic and bainitic transformations. The stabilization of the structure and the stress strain state after welding tends to abruptly improve the resistance to cracking since it is more difficult for creep to take place. During martensite transformation, the rate of plastic deformation in the HAZ is governed by the total density of mobile dislocations

formed during the high temperature deformation of austenite as well as during the formation of martensite. Previous high temperature deformation along grain boundaries and the unstable structure intensify intergranular slip as the tensile stresses increase, at temperatures below 200°C.

Inclusions and impurities around grain boundaries play an important role in the initiation of sub-microcracks during intergranular slip. The active growth of these sub-microcracks is caused by trapped vacancies initiated during rapid cooling, plastic deformation, and martensitic transformation.

To prevent delayed breakdown, it is preferable to use highly concentrated heat sources, and preheat to 100-150°C. Isothermal holding after welding is effective at temperatures of 500-600°C. Conversely, very high cooling rates at martensitic transformation temperatures limit the height of the steps at the grain boundaries and retard the diffusion of hydrogen. Reducing the grain size and the first order tensile stresses (ie. by peening) decreases the likelihood of sub-microcrack formation.

Kasugi (1983) investigated fractographically the initiation and propagation of weld cold cracks SM50 and HT80 steel. Factors considered were the hydrogen content, stress level, and microstructure. Fracture modes were intergranular fracture surface (IG), quasi-cleavage (QC), intermediate fracture surface of QC and dimple fracture (CD), and dimple

fracture surface (D). The aspects of hydrogen affecting crack propagation are categorized as:

1) Diffusible hydrogen content and its distribution in the weld zone.

2) Diffusion of hydrogen as affected by microstructure.

3) The redistribution of hydrogen in a weld zone is induced by an applied stress.

Fractographic observation revealed that the cracks initiated and propagated in the HAZ, along the fusion line, when stress levels were low (near the critical stress level) and the hydrogen content was low. When the hydrogen content was high with low stress levels and the hydrogen content was low with high stress levels, the cracks tended to initiate in the HAZ and propagate into the weld metal. The cracks initiated and propagated into the weld metal with high hydrogen content and high stress levels. The high-hydrogen content was approximately three times higher than the low-hydrogen content in these experiments.

Kihara (1978) study investigated the high crack sensitivity of HY-130 in shielded metal arc (SMA) welds by observing the root crack surface fractured in the tensile restraint (TRC) test. At low applied stress, the crack propagated predominantly through the weld metal and was largely intergranular. As applied stress increased, the area of intergranular fracture decreased. The intergranular region was found to be nearly perpendicular to the

applied stress and consisted of intergranular fracture along columnar crystal boundaries of prior austenite. This region was found to be at the root edge. There was a micro solidification crack found at the root edge that grew into a large intergranular crack. This was considered to be a rare example. Cracking in HY-130 is generally considered to be hydrogen-induced.

Kikuta (1978) investigated the microscopic redistribution of hydrogen and its effect on fracture morphology. Tension tests, an internal friction monitoring experiment, and an electrochemical hydrogen flux monitoring test conducted. The fracture morphologies as viewed with a scanning electron microscope showed hydrogen accumulated in the area of the dislocation on slip planes in grain boundaries.

Hydrogen-assisted cracking results in transgranular and intergranular cracking in the HAZ. The transgranular cracks were observed with subcracks along the boundary of lath and crystallographic martensite, forming on {110} planes. The intergranular cracking was observed with tongue-like patterns and microcracks on a part of the grain boundary surface. The intergranular cracking mode is dominant because grain boundary dislocation densities have been estimated to be three orders of magnitude higher than dislocation densities interior to the grain at modest strain and because hydrogen supersaturates in the region.

Makhnenko (1986) quantitatively evaluated the degree to which the hydrogen concentration may increase with time at the tips of crack-like defects in the HAZ with relation to the residual stress and the dimensions of the defects.

High hydrogen concentration is linked with the inconsistent distribution of residual stress and plastic deformation over a cross section of the weld. Longitudinal cold cracks develop primarily in the fusion zone where longitudinal and transverse stress are nearly equal. The depth of penetration of the above cracks into the base metal is dependent on the level of longitudinal stress and the crack resistance of the metal. During crack development, there is a drop in resistance of the metal at the crack tip. There may also be saturation of the metal by hydrogen diffusion at the crack tip caused by a corresponding concentration of stresses.

The mechanism of delayed breakdown can be explained in regions of increased mean stresses, where the hydrogen concentrates, which are created by the residual stresses in the region of the geometrical stress raisers in the HAZ. Depending on the concentration of hydrogen in this region, the resistance to cleavage fracture can change.

The author presents a two-dimensional analysis of the hydrogen concentration at the crack tip by diffusion as related to the crack dimension. The hydrogen concentration was found to be nearly equal in the crack tip region and the peripheral region when residual stresses in the longitudinal direction less than 98 MPa. However, when the residual stresses are

greater than 490 MPa, the hydrogen concentration can be several times greater in the crack tip region as compared to the peripheral region. This is also a function of time due to the diffusion process of hydrogen.

Matsuda (1985) investigated the effect of oxygen on cold cracking in high strength steel. In an HY-130 weldment system, the oxygen content changes in the range of 15-210 ppm were measured in terms of solidification behavior, microstructure, inclusions, and formation and migration of austenite boundaries. Intergranular fracture increased with an increase in oxygen content. The study found that intergranular fracture surfaces including oxygen had many microvoids and "microcones" (micro-projections that match up with the microvoids). There were many inclusions near the prior austenite grain boundary. These inclusions caused microvoids and microcones on the intergranular fracture surface. The migration of austenite boundary from the solidification boundary reduced with an increase in oxygen content. The inclusions precipitating on the solidification boundary were able to hinder this migration.

McMahon (1981) focused on the mechanism and the physical nature of hydrogen on deformation and fracture in iron and steel. The key features are: 1) that hydrogen alters the binding energy of the crystal lattice in such a way that the cohesive energy is reduced and screw dislocation mobilization is increased while edge dislocation mobilization is decreased and 2) that hydrogen is trapped by particle/matrix interfaces thereby enhancing

plastic rupture, and by dislocation cores which permit dislocation "sweep-in" from the surface and glide-plane decohesion.

In quenched and tempered steels, hydrogen induced fracture is intergranular decohesion, usually along prior austenite grain boundaries. Hydrogen has been found to produce brittle fracture by decohesion of grain boundaries already weakened by impurity segregation. It is characterized by apparently brittle cracking on {110} or {112} planes. It occurs in the plates or laths of tempered bainitic or martensitic steels. This is a result of the collection of atomic hydrogen in heavily dislocated slip bands. This is a strain controlled fracture mode that produces Mode II cracking. For a given impurity concentration, the stress intensity required for macrocrack growth decreases as the hydrogen concentration increases.

Nippes (1988) investigated weld metal hydrogen content and hydrogen-assisted cracking in flux cored arc welds in HY-80. Welds were made with as-received flux cored electrodes and special moisture resistant electrodes. Flux cored (as opposed to flux covered) electrodes offer low moisture content filler material.

The hydrogen content of the electrodes was found to be 2 ppm and 1.36 ppm, respectively. The critical hydrogen content was determined to be 4-5 ppm, with extensive cracking occurring at 9-10 ppm. Susceptibility to hydrogen cracking was determined by an augmented strain cracking test. This test is designed to produce a known reproducible

strain in the outer elements of a weld specimen. The augmented strain required to produce cracking was 0.6% for the as-received electrode and 1.5% for the moisture resistant electrode. Crack initiation and propagation were measured by acoustic emission. Crack initiation was found to be in the coarse grained or partly melted HAZ and propagated in to the weld and base metal.

HAZ cracking was usually perpendicular to the stress direction and was underbead and removed from the toe on either side of the weld. Despite the orientation of inclusions parallel to the primary stress directions, these inclusions sometimes act as crack initiators. Crack propagation was normally intergranular, along prior austenite grain boundaries.

Sterenbogen (1987) discussed the resistance of high strength steels to cold cracking or hydrogen delayed cracking. The need exists to develop and improve simple and reliable methods of evaluating cold cracking resistance. A new testing method utilizing flat test specimens without notches to evaluate cold cracking resistance was presented.

Cold cracking occurs more frequently in the HAZ where phase transformations result in the formation of a structure with a high level of local microstresses. The maximum critical stress is a commonly used parameter to evaluate cold cracking resistance. This stress is defined as the maximum stress at which the specimens do not fail within 24 hours. This parameter is influenced by specimen size, composition, and thermal cycle of welding. As specimen width increases, the critical stress decreases. The reduction in

critical stress is influenced by the increasing degree of strain localization and formation and growth of a plane stress state with increasing width. The critical stress increases with the reduction in the mean cooling rate in the HAZ metal. This is due to the self-tempering of the resulting martensite, reduction of local microstresses and more efficient hydrogen removal from the HAZ. A proposed criterion for cold cracking resistance, particularly for large specimens, was recommended as the ratio of the maximum critical stress to the yield strength. If this ratio is greater than one, then cracks do not form in the HAZ of the welded joint.

Thompson (1981) reviewed the role of microstructure in hydrogen embrittlement. It discusses the results of several pertinent crack initiation and propagation experimental studies including martensitic, pearlitic, and spheroidic 1045 bend test, and bainitic 4140 bend tests.

The problem of hydrogen assisted cracking has two intimately connected parts: crack initiation and crack growth. There is evidence that cracks initiate below the surface of the material in the presence of internal hydrogen and slow crack growth can occur by repeated re-initiation ahead of crack tips and joining up with the main crack. Also, the presence of substantial pressures of external gaseous hydrogen can cause cracks to originate at the surface of the material. When subsurface initiation does occur, there is evidence that it occurs at locations of maximum triaxial stress. Hydrogen is transported to these locations, whether it originates internally or externally, by normal lattice

diffusion, dislocation core or grain boundary diffusion, or dislocation transport. Once hydrogen is available at these sites, cracks can be initiated from them. The crack can then proceed by intergranular cracking, interphase cracking, by acceleration of microvoid coalescence at carbide particles, or by transgranular cleavage. The "trapping" strength of hydrogen can affect the cracking rate in different microstructures. Hydrogen can be trapped in defects in steel that include dislocations, impurity atoms, inclusion particles, interfaces between the matrix and carbide particles, internal cracks and voids, and grain boundaries.

Urednicek (1978) presented a quantitative relationship expressing the effect of residual longitudinal stress on cold crack nucleation in the HAZ of a root pass of a butt weld in high strength steel. In general, the thermal stresses induced during welding are attributed to the restraint of free thermal expansion and contraction by the surrounding structural elements in a welded structure. In the HAZ of butt welds, the transverse residual stresses induced by external restraint govern the formation of cold cracks in this region. In longer welds on thick plate, the stresses and strains produced by internal restraint are triaxial and are due to inhomogeneous heating and cooling. The relationships discussed are in terms of the stress intensity factor which applies to cracks once nucleated, if stress levels are below 2/3 of the yield strength. The approach allows for the assessment of the effect of the longitudinal residual stress on a reduction in the critical plastic zone size under plane strain conditions, and on the subsequent intensification of hydrogen buildup up at the elastic-plastic boundary.

Wong (1988) discussed the effect of diffusible hydrogen on cracking susceptibility of HY-80 steel and measures of cracking resistance determined by implant weldability tests and rigidly restrained cracking (RRC) tests.

The implant weldability test involves inserting a cylindrical sample of the material under study into a hole drilled in a 25 mm thick welding pad. A weld bead is then deposited on the pad, fusing the specimen to the pad and creating a HAZ in the specimen. The hydrogen level introduced corresponds to the electrode and its exposure condition. The specimen is then statically loaded to a desired stress. The time to fracture is measured up to a limit of 1000 minutes. By conducting this test to different stress levels, the lower critical stress threshold (LCS) can be evaluated. The LCS can then be a measure of crack susceptibility.

The proportionality constant has been found to be in the range of 0.045-.050. This calculated stress can be compared to the LCS to predict cracking during this test.

Hydrogen cracking is controlled by weld preheat and interpass temperatures and the amount of hydrogen contained in the welding electrode. Hydrogen cracking in high strength steels is more prevalent in the HAZ. The susceptibility of the HAZ to hydrogen cracking can be evaluated by its hardness through the use of a carbon equivalent formula. The high carbon equivalent and thus the high carbon content of HY-80 result in hard HAZ microstructures during welding.

Stress Corrosion Cracking:

Brooks (1979) investigated the microstructure-property relationship in high strength steels. The particular steel investigated was HP-9-4-20, a steel used in aerospace and ordnance applications. It has a high yield strength (180 ksi), high toughness (CVN =55-60 ft-lb) and good weldability. In thick weld sections, the mechanical properties of the weld metal are similar to the base metal with or without heat treatment. During tempering, both the hardness and tensile strength decrease, while toughness and yield strength increase. The resistance to stress corrosion cracking is high in both the HAZ and fusion zone.

In sections without heat treatment in GTA welds, the tempering occurs by the heat of the subsequent filler passes which can consist of fifty or more passes. In thin sections, this is not possible. However, the investigation showed that a tempering thermal cycle can occur in a standing edge weld configuration. This configuration allows the weld to be tempered without other sources of post-weld heat treatment in the same fashion as the thick plate sections. The standing edge can then be machined off after welding is completed. The benefit of this method is an improvement in the stress corrosion resistance over a nontempered weld configuration. The HAZ requires a tempering thermal cycle of 1200°F and the fusion zone requires a tempering thermal cycle of 2000°F.

Chen (1979) investigated the stress corrosion failure in HY-130 weld metals produced in wedge opening load (WOL) and cantilever beam (CB) specimens and related the level of cracking resistance through the fracture separation process to the microstructure of the weld. The study showed that the welding variables are important factors in determining the microstructure, mechanical properties, and SCC performance of the weld. The specimens susceptible to SCC exhibited a more brittle fracture appearance (intergranular and quasi-cleavage). The solidification microstructure did not appear to have a great effect on the operating crack path. GTA welds appeared to have a greater resistance to SCC due to a more refined structure than GMA and SMA welds.
The susceptibility to cracking in these welds appeared to be dependent on the amount of retained austenite and the amount of untempered and/or twinned martensite.

Chen (1980) investigated the correlation of microstructure and stress corrosion fracture of HY-130 steel weldments. Multipass welding can produce various microstructures in the weld and HAZ which results in intimately mixed fracture modes in SCC specimens. It is shown that the refined microstructures were most resistant to SCC, and the accompanying fracture mode was microvoid coalescence. More brittle fracture modes associated with the columnar/coarse equiaxed grain structures of untempered martensite or bainite were less resistant to SCC.

Fraser (1982) investigated the correlation of fracture morphology and the corresponding microstructure with SCC resistance of HY-130 weld metal as welding conditions and heat

treatment varied. GTA, SMA, and GMA welds were investigated. No single microstructure was identified in the HY-130 weldment system as yielding consistently high K_{iscc} values (which indicates high resistance to SCC). However, it was shown that a highly refined and relatively homogenous microstructure is important to high SCC resistance. The ability to reheat the weld metal through low deposition rate processes such as GTA produced a uniform, refined, tempered microstructure that fractured predominantly by microvoid coalescence (MVC). GMA and SMA processes produced a coarse grained, non-uniform microstructure which fractured by intergranular separation and cleavage. Heat treatment of GMA welds to deliberately refine the microstructure resulted in fracture by MVC and improved the resistance to SCC. Limited variations in the alloying elements in the weld metal had no apparent effect on SCC resistance.

Fujii (1981) examined the factors influencing stress corrosion cracking in high strength steels including the relative influences of yield strength, electrochemical potential, welding process, and weld metal composition. Weldments using 120S, 140S, AX140 and HY-130 filler material were welded by GMA and GTA welding processes. The multipass welding processes produced very complex martensitic-bainitic type microstructures. The GTA welds were considerably more fine grained, highly tempered, and contained less oxygen and nitrogen than the GMA weld metals. The GTA weld metals exhibited enhanced fracture toughness but only HY-130 and 140S exhibited an increased resistance to stress corrosion cracking. A low sulphur content appears to have a major influence on increasing resistance to SCC. The role of sulphur is presumed to be that of a catalytic

poison for the hydrogen recombination reaction, which increases with nascent hydrogen absorption.

Fukagawa (1982) estimated the crack sensitivity of a multipass welded joint whose restraint intensity is relatively small through the investigation of welding deformation, residual stress and variation of weld strain in large welded joint specimens.

In large double-sided welded joints, large "rotational distortion" (bending distortion) occurs. This causes large tensile residual stress and weld strain in the transverse direction of the weld line at the toe and the reinforcement of the weld metal of the backside weld. The reinforcement of the weld metal on the backside exhibited higher residual stress that the toe of the weld. The cracks were caused by the concentration of the weld strain at these points, coupled with the effect of diffusible hydrogen. The surface crack ratio increased with the amount of diffusible hydrogen. The shape of the cracking, and the preheat and interpass temperatures required for the prevention of cracking varies depending on the steel, the electrode, and the welding atmosphere.

HT80 generally exhibits a higher crack sensitivity than HT60. However, HT60 sometimes exhibits higher crack sensitivity due to the higher rotational distortion, weld strain, and diffusible hydrogen than HT80 weld metal.

Zanis (1978) presented the approach of the U.S. Navy technology development program on "subcritical cracking" of high strength steel weldments. Subcritical stress corrosion and hydrogen stress cracking is to be investigated in the program in order to ensure integrity of marine structures fabricated with steel weldments in the range of 100 to 200 ksi. This author defines the term subcritical cracking (SCC) as slow stable crack extension under static loading in seawater at stress intensities below K_{ic} (critical stress intensity factor for fracture in air) due to stress corrosion of hydrogen stress cracking. Stress corrosion is the behavior observed in freely corroding steel in seawater while hydrogen stress cracking applies to steel which is coupled to a sacrificial anode.

In HY-130 weldment systems, the base metal SCC fractures consist of mixtures of microvoid coalescence (MVC) and cleavage separation. The amount of cleavage observed increases with increasingly negative electrochemical potential. The weld metals with lower K_{iscc} values exhibit increasing amounts of brittle intergranular separation as the electrochemical potential becomes more negative.

Zanis (1982) investigated stress corrosion cracking (SCC) in HY-100 and HY-130 weldments using GMA and GTA welding processes. SCC refers to slow stable crack growth below K_{ic} (plane-strain fracture toughness).

Strength level is the dominant factor in controlling the SCC threshold (K_{iscc}) in these steels. The resistance to SCC decreases with increasing strength. The weld microstructure

is the most significant factor in determining this threshold. The weld microstructure is determined by welding parameters, filler metal composition, and welding process. Welding parameters that result in repeated reheating of the weld metal during fabrication and which eliminate martensite from the microstructure are necessary for maximum SCC resistance in HY-130 weld metals. The parameters are normally those associated with low deposition rate welding processes such as GTA welding. The predominantly acicular ferrite microstructure of HY-100 GMA weld metal has a significantly higher K_{iscc} than the mixed martensite and bainite microstructure of HY-130 GMA welds (121 and 63 $MPa/m^{1/2}$). The grain size of HY-100 and HY-130 are ASTM 6 and ASTM 8-9, respectively.

Weld metal sulphur content did not affect the K_{iscc} of either weld metal when tested in seawater at severe levels of cathodic protection . HY-100 base metal and weld metal was found to be resistant to SCC in seawater even under conditions of severe cathodic polarization.

Zhiming (1982) investigated the effects of environmental humidity and welding technology on crack sensitivity of ultra-high strength steel using a four point bend test and surface crack tensile tests. Specimens were welded by TIG welding and pulsed TIG welding processes. The pulsed TIG specimens showed less susceptibility to cracking than those welded by TIG welding. In the partially melted zone, hydrogen diffused from the weld metal and concentrated along the melting boundaries. Initiation of microcracking

was accompanied by evolution of hydrogen bubbles at the grain boundaries. In the quenched zone, hydrogen cracking is caused by embrittlement of twinned martensite. TIG welding produced coarsened lath martensite and twinned martensite. The pulsed TIG welding produced refined lath martensite and alloyed carbide. The formation of the twinned martensite is dependent on the carbon level. A transition from lath to twinned martensite was found in steel with a carbon content ranging from 0.1 to 1.0 weight percent.

The susceptibility to stress corrosion cracking in the HAZ increases with increasing hardness, and the greatest susceptibility is in the coarsened grain quenched zone. This is due to the presence of lath and twinned martensite in the quenched zone.

Miscellaneous

Barnes (1985) investigated the problem of crack initiation, propagation and arrest in HY-80 weldments under rapidly applied loading. The authors provide a good background on the development of elastic-plastic dynamic fracture mechanics techniques as applied to rapid loading. The paper presents both experimental and analytical results using an approach that quantifies a parameter called the crack tip opening angle (CTOA). The results indicate that the presence of weld-induced residual stresses strongly affects the crack length at arrest.

Khriplivyi (1988) discussed the special features of welding high strength multilayer steels. Multi-layer high strength steels combine high strength layers alternately with layers of lower strength but higher ductility. This results in high service strength characteristics not achievable in single layer steels by alloying, plastic deformation, or heat treatment. The features of the formation of the stress state in the HAZ of two layer joints can be used successfully for increasing the cold cracking resistance of the welded joints in two and multi-layer steels.

Masubuchi (1986) article discussed the unique fracture characteristics of weldments. The basic mechanisms of fracture include ductile fracture, brittle fracture, fatigue fracture, and stress corrosion cracking. The metallurgical heterogeneity of the weld and base metal determines the metallurgical structure of the HAZ. Residual stresses and distortions can promote fracture. Welding causes various types of distortions including transverse shrinkage, longitudinal shrinkage and angular distortion. Weld defects, such as cracks, porosity, and slag inclusions, also promote fracture.

Brittle fracture in weldments can be characterized by fracture appearance, temperature, stress at failure, origins of failures, and fracture propagation. Brittle fracture in weldments can be prevented by ensuring the base metal and weld metal have adequate fracture toughness. The fracture toughness of a material is affected by the crystal structure, chemical composition, and microstructure. The fracture toughness generally decreases with increasing strength level. The Charpy V-notch test, crack opening

displacement (COD) test, drop weight test, and dynamic tear test are common tests used to evaluate the fracture toughness of a material. Linear-elastic fracture mechanics (LEFM) is most often used to describe brittle fracture in weldments. Unstable brittle fracture will occur when the K-value exceeds the critical stress intensity factor.

Fatigue fracture occurs after repeated loadings and can be made more serious by corrosion. The type of welded joint can affect fatigue strength. A butt weld has a higher fatigue strength than a fillet weld due to the stress concentrations present in the fillet weld especially near the toe of the weld. Fatigue fractures often initiate from small, unimportant, incidental welds. The rate of fatigue crack growth at nominal stresses below 2/3 yield can be analyzed by applying linear elastic fracture mechanics.

Stress corrosion cracking (SCC) is a brittle fracture of a material exposed to certain corrosive environments. Steel will suffer from SCC when exposed to alkalis, some nitrates and hydrogen sulfide. Weldments with high tensile residual stresses are particularly vulnerable to SCC, even without any external loading.

You (1984) investigated the susceptibility of HY-80 to stress relief cracking (SRC). Since the coarse grained HAZ is the most susceptible microstructure to cracking, a comparison is made between the cracking behavior in the HAZ of a metal inert gas butt weld and a plate material with a simulated HAZ microstructure.

In both cases, cracking occurred under applied load of a magnitude typical of in service residual stresses and that the severity of cracking was similar. If the crack is constrained to propagate into fine grained material, it will eventually arrest in grain sizes less than 15 microns. In multipass weldments, regions of coarse grained HAZ are often separated by areas refined by later passes and therefore these welds have a lower susceptibility to SRC. Two fracture modes, low ductility intergranular fracture (LDIGF) and intergranular microvoid coalescence (IGMVC), were found in both conditions.

LDIGF is characterized by relatively smooth intergranular facets with some associated surface particles and occurs at the low end of the temperature spectrum (450-600°C). IGMVC is characterized by heavily cavitated intergranular facets and occurs at temperatures above 600°C. Factors affecting this mechanism include:

1) the stress intensifying geometry of the weld

2) intergranular segregation of embrittling residual impurities, which may be enhanced by the crack tip stress field

3) precipitation of grain boundary carbides, which are thought to act as crack nuclei and which may also cause an increase in grain boundary impurity levels through solute rejection

4) local crack tip deformation resulting from the decrease in yield stress with increasing temperature.

It is possible that crack propagation through this mechanism occurs in a brittle fashion in discrete steps or that the cracks extend by a microcavitation mechanism. There is a limited role for microductility, especially as the rate of crack growth decreases with the decrease in stress intensity at higher temperatures. The role of crack propagation can be characterized by a function of stress intensity (K) and temperature. Stress intensity is controlled by crack length and stress level only if below 2/3 yield, which relaxes with increasing temperature and time. This study showed in both specimens that the LDIGF mode is dominate in the regime of low temperature (450-600°C) and high stresses.

The IGMVC cavitation in the simulated material has been shown to be associated with MnS particles precipitated on or close to grain boundaries during the HAZ thermal cycle. This mode was found to be dominant at high temperature (greater than 600°C) and low stresses.

Quantitative prediction of SRC is complex and requires knowledge of residual stress levels, stress relaxation characteristics of the weldment, and the relationship between the stress intensifying geometry and the susceptible coarse grained material.

Appendix E

Experimental Results

	Force (kN)	x (cm)	delta x (cm)	Moment (Nm)	Curvature (cm)
MILD STEEL WELDED					
Replica	0.32	5.650	0.0001	11.15	********
	3.24	5.604	0.046	113.47	838.97
	5.78	5.561	0.089	202.44	432.62
	8.09	5.505	0.145	318.22	285.57
Replica	10.38	5.483	0.167	383.30	230.80
	12.82	5.432	0.218	448.70	176.69
	13.23	5.411	0.239	463.05	161.18
	14.00	5.384	0.266	490.00	144.84
	14.60	5.352	0.298	511.00	129.31
	15.00	5.321	0.329	525.00	117.15
	15.34	5.279	0.371	536.90	103.92
	15.46	5.244	0.406	541.60	94.99
	15.62	5.208	0.442	546.70	87.28
	15.69	5.116	0.534	549.15	72.31
	15.75	5.113	0.537	551.25	71.91
	15.82	5.036	0.614	553.70	62.94
Replica	15.38	4.857	0.693	538.30	55.83
MILD STEEL PLATE					
Replica	0.30	5.584	0.0001	10.55	********
	2.28	5.532	0.032	78.83	1203.14
	3.58	5.511	0.053	125.44	728.44
	4.67	5.495	0.069	163.28	558.00
	6.56	5.486	0.098	228.50	382.90
	8.26	5.436	0.126	289.73	305.61
	9.79	5.410	0.154	342.55	250.06
	10.99	5.385	0.179	384.65	215.15
	12.21	5.351	0.213	427.35	180.83
	13.28	5.312	0.252	464.80	152.88
	13.89	5.273	0.291	486.15	132.42
	14.12	5.233	0.331	494.20	116.44
	14.31	5.201	0.363	500.85	106.20
	14.40	5.167	0.397	504.00	97.13
	14.43	5.128	0.436	505.05	88.47
	14.47	5.097	0.467	506.45	77.88
	14.54	5.020	0.544	508.90	70.99
	14.23	4.874	0.69	498.05	58.07
	14.28	4.589	0.975	499.80	39.87
	14.35	4.386	1.198	502.25	32.58

	Force (kN)	x (cm)	delta x (cm)	Moment (Nm)	Curvature (cm)
HY-100 WELDED					
Replica	0.00	5.627	0.0001	0.04	********
	5.37	5.535	0.092	166.09	418.51
	8.58	5.487	0.14	300.18	275.05
	11.50	5.443	0.184	402.50	208.31
	13.22	5.417	0.21	462.70	183.42
	15.98	5.375	0.252	558.60	152.88
	18.18	5.341	0.286	636.30	134.73
Replica	20.90	5.298	0.329	731.50	117.15
	23.09	5.263	0.364	808.15	105.91
	28.14	5.214	0.413	914.60	83.38
	29.55	5.150	0.477	1034.25	80.90
Replica	31.55	5.104	0.523	1104.25	73.62
	33.50	5.043	0.584	1172.50	66.15
	35.00	4.991	0.636	1225.00	60.78
	36.41	4.912	0.715	1274.35	54.13
	37.54	4.841	0.786	1313.90	48.29
	38.12	4.797	0.83	1334.20	46.71
	38.67	4.743	0.884	1353.45	43.90
Replica	40.24	4.554	1.073	1408.40	38.30
	39.67	4.554	1.073	1388.45	38.30
HY-100 PLATE					
Replica	0.20	5.555	0.0001	7.00	********
	2.90	5.509	0.048	101.57	836.97
	5.78	5.465	0.09	201.48	427.81
	9.13	5.414	0.141	319.55	273.11
	12.24	5.367	0.188	428.40	204.86
	14.95	5.328	0.229	523.25	168.21
	19.30	5.281	0.294	675.50	131.07
	20.26	5.247	0.308	709.10	125.12
	25.32	5.171	0.384	886.20	100.41
	27.03	5.143	0.412	946.05	93.61
	31.00	5.048	0.507	1085.00	76.14
Replica	33.74	4.988	0.567	1180.90	65.82
	34.88	4.907	0.648	1220.80	59.87

	Force (kN)	x (cm)	delta x (cm)	Moment (Nm)	Curvature (cm)
HSLA-100 WELDED					
Replica	0.04	5.622	0.0001	1.31	********
	5.16	5.541	0.081	160.43	475.34
	8.39	5.492	0.13	283.76	296.20
	11.49	5.444	0.178	402.15	216.36
	14.75	5.394	0.228	516.25	168.95
	17.02	5.358	0.264	595.70	146.94
	19.50	5.318	0.304	682.50	126.76
Replica	20.37	5.304	0.318	712.95	121.19
	22.13	5.274	0.348	774.55	110.77
	23.97	5.242	0.38	838.95	101.48
	25.83	5.208	0.414	904.05	93.18
	27.80	5.164	0.458	973.00	84.24
Replica	28.72	5.113	0.509	1040.20	75.84
	32.03	5.022	0.6	1121.05	64.40
	33.60	4.984	0.638	1172.60	58.77
	34.40	4.808	0.713	1204.00	54.28
	35.30	4.842	0.78	1235.50	49.68
	36.22	4.770	0.852	1267.70	45.52
	36.82	4.680	0.832	1288.70	41.67
	37.84	4.620	1.002	1324.40	38.81
	38.44	4.467	1.155	1345.40	33.78
	39.15	4.362	1.26	1370.25	31.05
HSLA-100 PLATE					
Replica	0.33	5.569	0.0001	11.57	********
	4.95	5.496	0.073	173.29	527.43
	8.98	5.419	0.15	348.18	256.73
	13.43	5.366	0.203	470.05	189.73
	14.54	5.349	0.22	508.90	175.09
	16.73	5.315	0.254	585.55	151.67
Replica	19.91	5.262	0.307	696.85	125.53
	21.56	5.236	0.333	754.60	115.75
	24.14	5.189	0.38	844.90	101.48
	26.84	5.128	0.441	939.40	87.47
	28.40	5.081	0.488	994.00	79.08
	29.05	5.063	0.506	1016.75	76.29
Replica	29.96	5.027	0.542	1048.60	71.25

	Force (kN)	x (cm)	delta x (cm)	Moment (Nm)	Curvature (cm)
HY-130 WELDED					
Replica	0.24	5.586	0.0001	8.42	********
	4.89	5.521	0.074	171.19	520.30
	5.18	5.516	0.079	180.43	487.37
	6.19	5.501	0.094	216.58	408.61
	7.37	5.483	0.112	257.78	343.79
	8.34	5.468	0.127	291.78	303.20
	8.54	5.450	0.145	333.97	265.57
Replica	10.18	5.440	0.155	355.80	248.45
	11.67	5.417	0.178	408.45	216.36
	13.69	5.388	0.209	478.15	184.29
	15.48	5.359	0.236	541.80	163.23
	17.89	5.326	0.269	618.15	143.23
	18.81	5.294	0.301	693.35	128.03
Replica	20.20	5.287	0.308	707.00	125.12
	22.50	5.252	0.343	787.50	112.38
	24.08	5.229	0.366	842.10	105.33
	28.43	5.193	0.402	925.05	95.93
	29.65	5.140	0.455	1044.75	84.79
Replica	30.24	5.134	0.461	1058.40	83.70
	32.45	5.099	0.496	1135.75	77.82
	34.77	5.062	0.533	1216.85	72.44
	35.00	5.059	0.536	1225.00	72.04
	36.85	5.026	0.569	1289.75	67.89
	38.85	4.988	0.607	1363.25	63.66
Replica	40.24	4.963	0.632	1408.40	61.17
	41.25	4.935	0.66	1443.75	58.59
	42.79	4.899	0.696	1497.65	55.59
	43.90	4.870	0.725	1536.50	53.39
	44.30	4.858	0.737	1550.50	52.53
	45.10	4.834	0.761	1578.50	50.89
	45.49	4.822	0.773	1592.15	50.11
	46.28	4.795	0.8	1619.80	48.44
	47.53	4.744	0.851	1663.55	45.57
	48.27	4.707	0.888	1689.45	43.70
	49.16	4.840	0.955	1720.60	40.69
Replica	50.17	4.607	0.988	1755.95	39.35
	50.33	4.590	1.005	1761.55	38.70
HY-130 PLATE					
Replica	0.07	5.550	0.0001	2.39	********
	3.81	5.487	0.003	133.42	611.14
	8.27	5.417	0.133	289.45	289.53
	10.98	5.378	0.174	384.30	221.33
	13.38	5.340	0.21	467.80	183.42
	15.37	5.309	0.241	537.95	159.65
	17.57	5.278	0.274	614.95	140.62
	18.48	5.247	0.303	681.10	127.18
Replica	20.19	5.236	0.314	706.85	122.73
	20.11	5.223	0.327	703.85	117.87
	22.01	5.209	0.341	770.35	113.04
	24.85	5.167	0.383	869.75	100.67
	28.22	5.116	0.434	987.70	88.88
	30.15	5.087	0.463	1055.25	83.34
	32.61	5.049	0.501	1141.35	77.04

	Force (kN)	x (cm)	delta x (cm)	Moment (Nm)	Curvature (cm)
	38.76	4.963	0.567	1288.60	68.12
	39.51	4.930	0.62	1382.85	62.34
Replica	40.35	4.912	0.638	1412.25	60.59
	42.70	4.855	0.695	1494.50	55.67
	44.51	4.801	0.749	1557.85	51.70
	46.02	4.750	0.8	1610.70	48.44
	46.76	4.710	0.84	1636.60	46.16
	47.65	4.672	0.878	1667.75	44.19
	48.44	4.624	0.926	1695.40	41.94
	49.14	4.581	0.969	1719.90	40.11
	50.04	4.541	1.009	1751.40	38.55
Replica	50.26	4.491	1.059	1759.10	36.77

Appendix F

Video Tape Map

Photo No.	Video Counter min	to	max	Material	Load (kN)	Objective Lens Pwr	Coordinates x	y	Locus	Notes
1	22	to	38	MS Plate	0	10			baseplate	
2	38	to	54	MS Plate	0	20			baseplate	
3	54	to	80	MS Plate	0	40			baseplate	anomaly - Wbing?
	80	to	89	STATIC						
4	89	to	108	MS Plate	0	40			baseplate	scratches
	108	to	125	BLANK						
5	125	to	143	MS Plate	0	10			baseplate	
	143	to	182	MS Plate	0	20			baseplate	
6	182	to	186	MS Plate	0	40			baseplate	
	186	to	205	BLANK						
7, 8	205	to	227	MS Plate	14	10			baseplate	same area as above
9	227	to	253	MS Plate	14	20			baseplate	
9 A	253	to	310	GARBAGE					baseplate	changing lenses
10	310	to	333	MS Plate	14	40			baseplate	
11	333	to	358	MS Plate	14	20			baseplate	same general area (cracks
12, 13	358	to	381	MS Plate	14	40			baseplate	
14	381	to	395	MS Plate	14	40			baseplate	
15	395	to	422	MS Plate	14	100			baseplate	crack tip

Photo No.	Video Counter min	to	max	Material	Load (kN)	Objective Lens Pwr	Coordinates x	y	Locus	Notes
16	439	to	470	HY-130	50	40	0	0.0000	at weld ed	
17	470	to	500	HY-130	50	40	0	0.0805	baseplate	
18	500	to	534	HY-130	50	40	0	0.1570	baseplate	
19	534	to	570	HY-130	50	40	0	0.2415	baseplate	
20	570	to	605	HY-130	50	40	0	0.3200	baseplate	
21	605	to	640	HY-130	50	40	0	0.4005	baseplate	cleavage?
22	640	to	689	HY-130	50	40	0	0.4780	baseplate	
23	689	to	706	HY-130	50	40	0	0.5575	baseplate	
24	706	to	741	HY-130	50	40	0	0.6375	baseplate	
25	741	to	772	HY-130	50	40	0	0.7150	baseplate	
26	772	to	805	HY-130	50	40	0	0.7985	baseplate	
27	805	to	841	HY-130	50	40	0	0.8835	baseplate	
	841	to	884	BLANK						
28	884	to	904	HY-130	50	40	0.1135	0.0000	at weld ed	adjacent to above
29	904	to	938	HY-130	50	40	0.1135	0.0780	baseplate	
30, 31	938	to	973	HY-130	50	40	0.1135	0.1580	baseplate	
32	973	to	1011	HY-130	50	40	0.1135	0.2400	baseplate	
33	1011	to	1034	HY-130	50	40	0.1135	0.3250	baseplate	linear gamma
34	1034	to	1062	HY-130	50	40	0.1136	0.3250	baseplate	repeat, gamma with decre
35	1062	to	1093	HY-130	50	40	0.1136	0.4040	baseplate	
36	1093	to	1112	HY-130	50	40	0.1136	0.4865	baseplate	cleavage, showing raised
37	1112	to	1143	HY-130	50	40	0.1135	0.5635	baseplate	
38	1143	to	1172	HY-130	50	40	0.1135	0.6450	baseplate	
39	1172	to	1202	HY-130	50	40	0.1135	0.7250	baseplate	
	1202	to	1232	HY-130	50	40	0.1135	0.8070	baseplate	
	1232	to	1262	BLANK	50	40				
	1262	to	1293	HY-130	40	40	0	0.0000	at weld ed	Note: this replica area is o
	1293	to	1321	HY-130	40	40	0	0.0830	baseplate	
	1321	to	1343	HY-130	40	40	0	0.1640	baseplate	
	1343	to	1372	HY-130	40	40	0	0.2445	baseplate	
	1372	to	1397	HY-130	40	40	0	0.3250	baseplate	small cracks
	1397	to	1422	HY-130	40	40	0	0.4100	baseplate	
	1422	to	1444	HY-130	40	40	0	0.4885	baseplate	slag?
	1444	to	1471	HY-130	40	40	0	0.5725	baseplate	
	1471	to	1498	HY-130	40	40	0	0.6546	baseplate	
	1498	to	1522	BLANK						
40	1522	to	1541	HY-130	40	40	0	0.0000	at weld ed	
41	1541	to	1568	HY-130	40	40	0	0.0845	baseplate	
42	1568	to	1591	HY-130	40	40	0	0.1625	baseplate	
43	1591	to	1615	HY-130	40	40	0	0.2480	baseplate	
44	1615	to	1640	HY-130	40	40	0	0.3255	baseplate	
45	1640	to	1668	HY-130	40	40	0	0.4080	baseplate	
46	1668	to	1691	HY-130	40	40	0	0.4915	baseplate	
47	1691	to	1720	HY-130	40	40	0	0.5635	baseplate	
48	1720	to	1738	HY-130	40	40	0	0.5635	baseplate	repeat at different gain lev
49	1738	to	1763	HY-130	40	40	0	0.6465	baseplate	
	1763	to	1783	BLANK						
50	1783	to	1809	HY-130	40	40	0.1015	0.0000	baseplate	
51	1809	to	1839	HY-130	40	40	0.1015	0.0855	baseplate	interesting tear
52	1839	to	1863	HY-130	40	40	0.1015	0.1675	baseplate	cracks & tears
53	1863	to	1889	HY-130	40	40	0.1015	0.2505	baseplate	
54	1889	to	1918	HY-130	40	40	0.1015	0.3315	baseplate	interesting crack pattern
55	1918	to	1934	HY-130	40	40	0.1015	0.3315	baseplate	distance measurement mo
56	1934	to	1966	HY-130	40	40	0.1015	0.4155	baseplate	

Photo No.	Video Counter min	to	max	Material	Load (kN)	Objective Lens Pwr	Coord inates x	y	Locus	Notes
57	1966	to	1980	HY-130	40	40	0.1016	0.4986	baseplate	
	1980	to	2010	GARBAGE						
58	2010	to	2053	HY-130	40	100	0.0685	0.3955	interesting	interesting crack pattern h
	2053	to	2079	BLANK						
59	2079	to	2103	HY-130	40	20			weld metal	typical
60	2103	to	2136	HY-130	40	40			weld metal	typical
61	2136	to	2161	HY-130	40	20			weld metal	typical
62	2161	to	2208	HY-130	40	40			weld metal	typical
	2208	to	2234	BLANK						
63	2234	to	2268	HY-130	50	20			weld metal	typical
64	2268	to	2291	HY-130	50	40			weld metal	small cracks, various orient
	2291	to	2327	BLANK						
	2327	to	2348	WHITE						
65	2348	to	2377	HY-130	0	40	0	0.0000	at weld be	
66	2377	to	2398	HY-130	0	40	0	0.0000	at weld be	repeat
67	2398	to	2423	HY-130	0	40	0	0.0800	baseplate	note the texture of the su
68	2423	to	2454	HY-130	0	40	0	0.1615	baseplate	look at the bumps
69	2454	to	2484	HY-130	0	40	0	0.2470	baseplate	
70	2484	to	2509	HY-130	0	40	0	0.3300	baseplate	
71	2509	to	2540	HY-130	0	40	0	0.4185	baseplate	
72	2540	to	2564	HY-130	0	40	0	0.5010	baseplate	bumps begin to disappea
73	2564	to	2585	HY-130	0	40	0	0.5850	baseplate	
74	2585	to	2610	HY-130	0	40	0	0.6710	baseplate	
	2610	to	2639	HY-130	0	40	0	0.7625	baseplate	
75	2639	to	2685	HY-130	0	40	0	2.2350	baseplate	at extreme distance
	2685	to	2693	BLANK						
76	2693	to	2716	HY-130	0	40			weld bead	typical
	2716	to	2740	BLANK						
77	2740	to	2767	HY-130	5	40	0	-0.0180	weld edge	star shaped crack pattern
78	2767	to	2794	HY-130	5	40	0	0.0510	baseplate	highly granular surface, s
79	2794	to	2818	HY-130	5	40	0	0.1345	baseplate	same
80	2818	to	2843	HY-130	6	40	0	0.2195	baseplate	
81	2843	to	2868	HY-130	5	40	0	0.3030	baseplate	
82	2868	to	2893	HY-130	5	40	0	0.3890	baseplate	
83	2893	to	2921	HY-130	5	40	0	0.4715	baseplate	
84	2921	to	2946	HY-130	5	40	0	0.5565	baseplate	
85	2946	to	2970	HY-130	5	40	0	0.6405	baseplate	
86	2970	to	2998	HY-130	5	40	0	0.7250	baseplate	
87	2998	to	3022	HY-130	5	40	0	0.8085	baseplate	
88	3022	to	3048	HY-130	5	40	0	2.2840	baseplate	at extreme distance
	3048	to	3065	BLANK						
	3065	to	3071	WHITE						
	3071	to	3073	SURFACE						
	3073	to	3074	WHITE						
	3074	to	3079	BLANK						
	3079	to	3082	WHITE						
89	3082	to	3115	HY-130	5	40	0		weld metal	note pattern (plastic zone
90	3115	to	3138	HY-130	5	40	0		weld metal	typical

Photo No.	Video Counter min	to	max	Material	Load (kN)	Objective Lens Pwr	Coordinates x	y	Locus	Notes
91	3155	to	3174	HY-100	33	40	0	-0.1565	weld metal	note crack
92	3174	to	3199	HY-100	33	40	0	-0.0770	weld metal	
93	3199	to	3219	HY-100	33	40	0	0.0070	edge of w	
94	3219	to	3243	HY-100	33	40	0	0.0880	baseplate	
95	3243	to	3266	HY-100	33	40	0	0.1705	baseplate	
96	3266	to	3287	HY-100	33	40	0	0.2555	baseplate	
97	3287	to	3306	HY-100	33	40	0	0.3365	baseplate	
98	3306	to	3327	HY-100	33	40	0	2.2575	baseplate	at extreme distance
	3327	to	3350	BLANK						
99	3350	to	3377	HY-100	33	40			weld metal	begin weld metal mozaic
100	3377	to	3395	HY-100	33	40			weld metal	repeat frame
101	3395	to	3415	HY-100	33	40			weld metal	
102	3415	to	3436	HY-100	33	40			weld metal	
103	3436	to	3457	HY-100	33	40			weld metal	end weld crack mozaic
	3457	to	3478	BLANK						
104	3478	to	3498	HY-100	20	40	0	-0.1560	weld bead	
105	3498	to	3519	HY-100	20	40	0	-0.0695	weld bead	
106	3519	to	3539	HY-100	20	40	0	0.0140	weld bead	
107	3539	to	3559	HY-100	20	40	0	?	baseplate	
108	3559	to	3580	HY-100	20	40	0	0.1825	baseplate	
109	3580	to	3598	HY-100	20	40	0	0.2650	baseplate	
110	3598	to	3623	HY-100	20	40	0	0.3525	baseplate	
	3623	to	3645	BLANK						
111	3645	to	3663	HY-100	0	40	0	-0.1560	weld bead	
112	3663	to	3682	HY-100	0	40	0	-0.0775	weld bead	
113	3682	to	3705	HY-100	0	40	0	0.0080	weld bead	
114	3705	to	3724	HY-100	0	40	0	0.0840	baseplate	
115	3724	to	3742	HY-100	0	40	0	0.1700	baseplate	
116	3742	to	3763	HY-100	0	40	0	0.2530	baseplate	
	3763	to	3786	HY-100	0	40	0	0.3396	baseplate	
117	3786	to	3804	HY-100	0	40	0	2.2445	baseplate	baseplate at extreme dista
	3804	to	3816	BLANK						
	3816	to	3822	WHITE						
	3822	to	3836	BLANK						
118	3836	to	3858	HY-100	0	40			weld metal	begin weld crack mozaic
119	3858	to	3878	HY-100	0	40			weld metal	same mozaic as above
120	3878	to	3899	HY-100	0	40			weld metal	end weld crack mozaic

Photo No.	Video Counter min	to	max	Material	Load (kN)	Objective Lens Pwr	Coordinates x	y	Locus	Notes
121	4158	to	4174	HSLA-100	30	40			weld metal	weld bead mozaic
122, 123	4174	to	4197	HSLA-100	30	40			weld metal	
124	4197	to	4216	HSLA-100	30	40			weld metal	
125	4216	to	4240	HSLA-100	30	40			weld metal	odd structure, similar to H
	4240	to	4414	BLANK						
	4414	to	4436	HSLA-100	0	40			weld metal	replica bubbles
126	4436	to	4458	HSLA-100	0	40			weld bead	typical; ?Intergranular crac
127	4458	to	4477	HSLA-100	0	40	0	0.0000	weld bead	
128	4477	to	4496	HSLA-100	0	40	0	0.0879	baseplate	
129	4496	to	4516	HSLA-100	0	40	0	0.1615	baseplate	
130	4516	to	4532	HSLA-100	0	40	0	0.2410	baseplate	
131	4532	to	4553	HSLA-100	0	40	0	0.3280	baseplate	
132	4553	to	4570	HSLA-100	0	40	0	2.2560	baseplate	at extreme distance
	4570	to	4578	BLANK						
133	4578	to	4597	HSLA-100	30	40	0	0.0000	weld edge	no cracks
134	4597	to	4614	HSLA-100	30	40	0	0.0884	baseplate	
135	4614	to	4636	HSLA-100	30	40	0	0.1655	baseplate	
	4636	to	4680	BLANK						

LIBRARY
NAVAL POSTGRADUATE SCHOOL
MONTEREY, CALIFORNIA 93943-5002

Thesis
I96
c.1

Iwanowicz
Study of residual
stresses and microcracks
in high strength steel
weldments.

Thesis
I96
c.1

Iwanowicz
Study of residual
stresses and microcracks
in high strength steel
weldments.

DUDLEY KNOX LIBRARY
3 2768 00037060 5